UNIVERSITÉ CATHOLIQUE DE LOUVAIN
École Polytechnique de Louvain
Institut de la Matière Condensée et des Nanosciences

Quantum Transport Phenomena in Covalently Functionalized and Disordered Graphene

Dissertation présentée en vue de l'obtention du grade de
Docteur en Sciences de l'Ingénieur
par

Nicolas Leconte

Membres du jury :

Prof. Jean-Christophe Charlier, promoteur
Prof. Bernard Piraux, président
Prof. Benoit Hackens
Prof. Philippe Lambin
Dr. Aurélien Lherbier
Prof. Richard Martel
Prof. Stephan Roche

Février 2014

Foreword

For one decade now, graphene has been at the forefront of research in the fields of Physics and Engineering. When in 2004, Sir Geim and Sir Novoselov synthesized a monolayer of carbon using a friday-afternoon experimental technique, little did they know they would trigger the birth of one of the most active communities of both experimental and theoretical physicists, trying to make the next big thing happen in industry. Not a week goes by without a new paper popping up explaining a new idea on how graphene could be used as a technological application. This thriving research has convinced the European Union this year to fund a Flagship dedicated to bring Graphene and other 2D materials from the lab to the factory.

The interest in this *wondermaterial* is inspired by some of its peculiar properties, which, in flatland, are sometimes very different from their 3D counterparts. To name a few, the in-plane bondstrength makes it stronger than diamond, while its out-of-plane flexibility renders it interesting for bendable devices. The specific honey-comb geometry leads to physics that transform graphene into an out-of-the-box lab to study high energy physics, related to its apparent massless like behavior of the electrons. Or finally, the huge associated mobilities might some day be interesting for use in electronic devices.

When I joined this community about four years ago, the graphene activity could still be considered in its early footsteps. Today, surprisingly, the early day somehow naive excitment hasn't faded yet. At the same time, the project has taken on some much needed maturity. Some bright people brought in their expertise from industry to transform the original idea from the lab to actual applications. To name a few, a famous brand

of tennis gear has developed a tennis racket improved in its mechanical properties by introducing graphene in its composite material, another high profile giant in electronical applications has developed prototypes of bendable touchscreens for smarthphones based on graphene, etc.

Luckily for physicists doing simulations tophill to understand and even predict new properties that could be useful someday, a lot still remains to be done. For instance, to be an ingredient in the cuisine of the electronics engineer, one has to be able to turn the charge flow on and off by letting otherwise metallic graphene behave like a semiconductor. Or one has to understand its interaction with hydrogen to make it useful to store the cations in batteries. Or one might try to help this carbon allotrope behave magnetically for cheap information storage.

One strategy to achieve these modifications of the properties of clean graphene is by functionnalizing it with foreign atoms. This has been my focus during the last four years, playing around with oxygen and hydrogen. I analyzed mainly on how these atoms influence the electronic transport properties.

Abstract

Tailoring the properties of graphene has been the subject of very intense research during the past few years. Such modification can be readily achieved using chemical functionalization with foreign atoms thanks to the two-dimensional nature of the material. The exact impact of such chemical treatment cannot always be accurately tackled experimentally, thus requiring active input from modeling and numerical simulations.

Theoretical models predict weak localization to occur in graphene under certain specific conditions, including the mixing between inequivalent K-point valleys induced by short-range disorder. Mesoscopic computer simulations based on accurate parameters extracted from first-principles Density Functional Theory calculations, and applied to realistic graphene samples (with sizes comparable to experimental ones), allow to verify the existence of such quantum interference effects, in both hydrogenated and ozonated graphene.

The seminal work by Geim and Novoselov suggested an Anomalous Quantum Hall Effect in graphene. In order to observe the very characteristic quantization of states in transverse conductivity measurements, the disordered system should combine the presence of both localized and extended states at specific critical energies, separated by mobility edges. The specific impact of disorder on this new quantum Hall effect is still a strongly debated issue among the theoretical community, due to the complexity of the calculations that have to be performed on realistic graphene samples.

The present work extends the knowledge on simplified disorder models to the realistic cases of oxygen functionalization and hydrogenation on the transport properties of graphene. Particular attention is given to

the specific impact of symmetry breaking induced by the non-equivalence of the two sub-lattices inherently present in the hexagonal structure. By including the effect of an external perpendicular magnetic field, the impact of symmetry preserving disorder on the Hall quantization is partially clarified. The appearance of previously unknown critical states specifically due to disorder in the diagonal conductivity is confirmed using a new formalism, which allows to predict the Hall conductivity.

In order to extend the range of possible applications of graphene-based material, the spin degree of freedom has to be considered in addition to the conventional charge component of the carriers. In this context, a better understanding of possible intrinsic magnetism in graphene is required. Presently, no full consensus exists in the community regarding the possibility to induce paramagnetic centers and/or long-range interaction coupling between these local magnetic moments.

A theoretical model is proposed allowing to check the existence of (anti)-ferromagnetism in graphene induced by hydrogen functionalization, through the observation of possible magneto-resistivity fingerprints.

Acknowledgements

In these few lines, I have the opportunity to thank all the people that have been contributing to where I am now, from a scientific point of view as well as from a human point of view. My thoughts are now wandering off to all the people I've had the chance to interact with during these last years, I hope I won't forget any one.

Let me first start by thanking my supervisor Jean-Christophe who, more than four years from now, said to someone in the lab "*I've just hired someone for a PhD. Based on his academic records, it's a long shot, but we'll see what it gives*". I want to thank him for believing in me and giving me the opportunity to join this exciting community. I really appreciated his scientific input. He often reminded me of the importance of rigour when communicating the scientific results. He also put me into contact with the many interesting scientists, including the following one.

Thus, I would like to give a huge thanks to Stephan, who could very well be considered my co-advisor in this work. He has given me the chance to use and develop further the computational tools that have been used in this work. His passion for the science, his ability to get excited about the smallest jiggle in the curves have been very contagious and will have a permanent impact on my future career. My stays in his group have been very inspiring, as well as the short stay in *Villa Nova* close to the sea.

The jury of my thesis has taken a lot of time to read the present manuscript, and has given my valuable feedback during the private defense. Profs. B. Piraux, B. Hackens, P. Lambin and R. Martel, as well as Dr. A. Lherbier, thank you! Aurélien, you've been very helpful also

guiving guidance regarding the technical issues I had with the Kubo code during the first years.

The other members of my scientific commitee deserve particular acknowledgement as well: Profs. L. Henrard, X. Gonze and G. M. Rignanese.

From a scientific point of view, I also want to thank Frank, who has helped me a lot while implementing a working code based on his yearlong work for the new formalism development calculating the Hall conductivity. Yannick has been very helpful in analyzing some details of the more complicated equations of the formalism.

The many people I have been interacting with during the different studies presented in this thesis certainly deserve their name here as well: David, Joël, Pablo, Juanjose and Adrian.

This lab has a great crowd of scientists, with who the scientific discussions have been very valuable. These discussions go well beyond scientific grounds, and the many informal interactions help one stay positive during the difficult times. Thank you, François for sharing the office with me, your clearcut opinion on *homeopathy* and other pseudoscientific gibberish were source for loads of fun. Zeila and Marcos, your vocal presence in our office was appreciated too. Andrés (tequila-breaks), Simon (casino initiation), Xavier (*helpful* late night advice), Guillermo (*python* guru), David (squash skills, more on that later), Martin (sugar-daddy), Geoffroy (*les pennés sont des gens sympas aussi*), Anna (*Italian candy is the best*), Matteo (*see you this afternoon, at* 10 *pm*), Stephan (ASCII computer games), Samuel (*have another drink*), Gaël (*some pies for the ACIM?*), Bruno (icecream), Nicky (long live the ETSF), Fabiana (PCPM Scientific day presentation), Lian (chocolate-factory), Albert (*let's push the simulations yet a bit further*), Sadia (*flamoushe*), Jean-Michel (*une rafale pendant que ça bilbotte?*), Alain (globetrotting wall-climber), Luc (YRM), Annette (nordic running) etc, you've all been very important colleagues and friends these years.

Also, thank you to all my friends, from the board games, grad school, AFS, ANLO, (SI)CI, running and triathlon, football, and outside. I hope to see you guys often, I'll come back from abroad. Thank you Caroline,

Amandine, Mehmet, Aline, Fynch, Ludo, etc for having shared lodging with me these last few years.

Finally, I'd particularly like to thank my family for supporting me during this thesis. You've been of great inspiration. At times, you've also given me the necessary slack when I had to *lauch some calculation* during family time (you've often wondered what physical movement is required to *lancer* anything other than a tennisball). Mum, Dad, thank you for all you've done for me during these 29 years. Sometimes, one needs a manuel to interact with me: you've written it. You've given me a great toolset of technical and human skills for the future. Dear brother and sisters, you're the best! Big hug to my grand-mothers!

I said I would come back to David's squash skills. These skills may or may not include, a bet gone wrong, *cheating and deception*, but I have to thank (or despise?) him (and his skills) for the remaining of the acknowledgements he (and some other colleagues) wrote for me, *to save me some time writing this Thesis.*

Thank you!
Nicolas

We quickly came aware that our initial approach of using three minds (DW, SD, AB) to approximate Nicolas' mind state at the end of his thesis was insufficient. Therefore, we had to expand our basis set to better describe the wavefunction by using a superposition of the world's greatest minds. Bazinga!

Now that I have counted twice to infinity and approached the great 42, I, Nicolas, feel the need to make a recount and share what I have learned, for I am an intellectual, i.e, *a person who's found one thing that's more interesting than sex* ("Aldous Huxley"), and that is, indeed, worth sharing.

I was born not knowing, and I had only a little time to change that here and there ("Richard P. Feynman"), so I struggled, since *invention, my dear friends, is 93% perspiration, 6% electricity, 4% evapora-*

tion, and 2% butterscotch ripple ("Willy Wonka, Willy Wonka and the Chocolate Factor").

I knew there would be sacrifices, that I had to become *not antisocial, just not user friendly* ("Unknown"). No more *fuki-fuki* ("Simon Dubois"). Yet I realized, *better to be a geek than an idiot* ("GPL"). The metamorphosis had started. And believe me, *for a successful technology, reality must take precedence over public relations, for nature cannot be fooled* ("Richard P. Feynman"). Thankfully, little pleasures started to come as comforting rewards. As I was embracing the force, I started to have thoughts like: *Software is like sex, it's better when it's free* ("GPL") and I have verified that *computer guys have skilled fingers, if you know what I mean* ("Unknown"). There were dark days too, like when I *spent a minute looking at my own code by accident, and found myself thinking "What the hell is this guy doing?"*. But of course *if we knew what we were doing, it wouldn't be called research* ("Albert Einstein").

Other times colleagues would say me with a sentence tone: *your theory is crazy, but it's not crazy enough to be true* ("Niels Bohr"). I went along, following my path, *prediction is very difficult, especially if it's about the future* ("Niels Bohr"). Yet, the learning was there. The young grasshopper has been patient. All those books, all those papers, the knowledge is inside me.

I thank you all, the authors. I stand now on the shoulders of giants thanking them, but also saying to the world *I know kung fu* ("Neo, The Matrix")! ... and *I'll be back* ("The Terminator").

David, Simon & Andrés

Contents

List of Figures

Introduction

Even though graphene was already studied extensively from a theoretical point of view, interest has only been substantial since its first conscious experimental realization in 2004 by Geim and Novoselov [1].

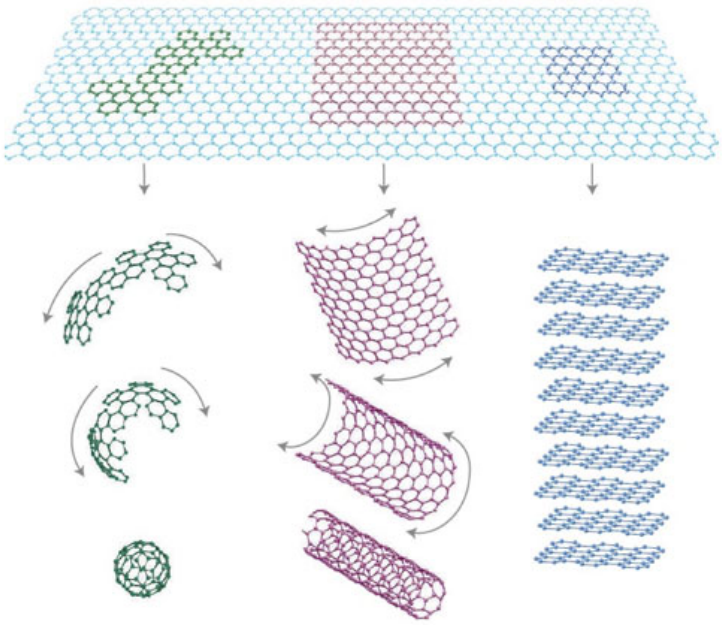

Figure 1: Carbon allotropes: graphene (top), fullerene (left), nanotubes (middle) and graphite (right).

Graphene is the 2D sibling among the other carbon allotropes such as graphite (stacked graphene layers) and diamond in 3D, fullerenes in 0D and carbon nanotubes (rolled graphene layers) and carbyne in 1D (see

Fig. 1 for a few family members). In graphene, the atoms are arranged in a two-dimensional honeycomb lattice, thanks to the sp^2 hybridization leading to three of the four valence electrons participating in the in-plane bonding. The last electron forms a so-called $\pi-$ orbital which is out-of-plane. The sp^3 hybridization occuring in diamond, including all electrons in covalent bonds, removes this electronic transport degree of freedom.

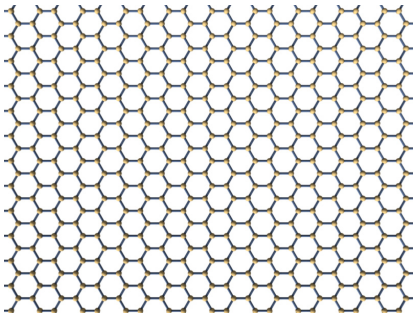

Figure 2: Graphene sheet

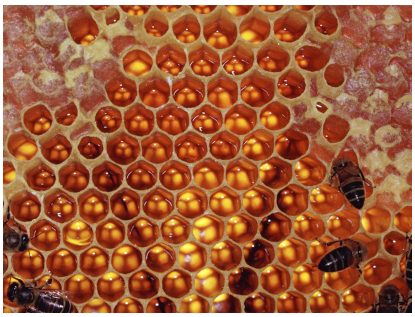

Figure 3: Honeycomb structure

To synthesize graphene, many methods have been proposed. The one which, *a posteriori*, seems very straightforward, is peeling off graphene from graphite by mechanical exfoliation. This can be done using simple scotch-tape and brought Geim and Novoselov the Nobel prize in 2010 for *groundbreaking experiments regarding the two-dimensional material graphene* when they managed to characterize the residues on the tape as graphene by performing transport measurements. Some of these transport measurements on the Quantum Hall Effect (QHE) are at the core of this Thesis.

Historically, when producing Silicon Carbide (SiC), unwanted carbon builds up at the surface of the material. However, it was soon realized that this carbon composition could actually be controlled in such a way that it forms a graphene layer [2, 3]. The substantial advantage over mechanical exfoliation is that it allows for mass production. Nevertheless, the properties of graphene obtained that way may be altered by the presence of the substrate and transfer onto another substrate might be required.

Such transfer is also required when using the chemical vapor deposition technique (CVD) where chemical precursors form graphene under the right treatment. Most often, the substrate used nowadays is copper [4]. As to the precursors, a real arsenal of carbon containing molecules have already shown good production yield. Even chocolate cookies have already been used in that sense [5].

Other methods to synthesize graphene involve for instance chemical exfoliation where the weak bonding between layers of graphene is broken using oxidation for instance [6]. Using other chemistry tools, carbon nanotubes can also be *unrolled*, leading to good control over the specific boundaries of the obtained graphene ribbons [7, 8]. This is of importance as the type of these boundaries play a significant role in the transport properties of graphene.

A more recent technique also allows for a very good control of the ribbon boundaries. This method uses chemical precursors which build up a graphene ribbon in a *bottom-up* approach [9].

Graphene is often called the material of all the superlatives. For instance, from the electronical point of view, it has an electron mobility which surpasses conventional materials by orders of magnitude. For encapsulated graphene, mobilities of 100 000 $\mathrm{cm}^2\ \mathrm{V}^{-1}\ \mathrm{s}^{-1}$ have been measured [10]. Very high current densities can also be sustained. From a mechanical point of view, on top of its nice bendability, it exhibits a Young Modulus of 1 TPa [11]. The modulus of steel is about one order of magnitude lower. From a thermal point of view, its conductivity is also very high. The combination of strong interatomic bonds and low mass of the carbon atoms allows for large structural vibrations dissipating heat very efficiently (3000 $\mathrm{Wm}^{-1}\mathrm{K}^{-1}$) [12]. And finally, from an optical point of view, the absorption of photons equals exactly $\pi\alpha \simeq 2.3\%$ where α is the fine structure constant [13]. This is relatively speaking a very high value considering the one-atom thickness of graphene.

All these exceptional properties have led people to believe in their application in the industry. The Graphene Flagship funded by the European Union has established a roadmap estimating the point in time where these applications could become reality. Some have already

reached maturity (bendable touch screens, graphene paints, etc) while others might still be decades away (applications based on spintronics). An overview of the applicability of such applications as seen by the Graphene Flagship is given in Fig. 4.

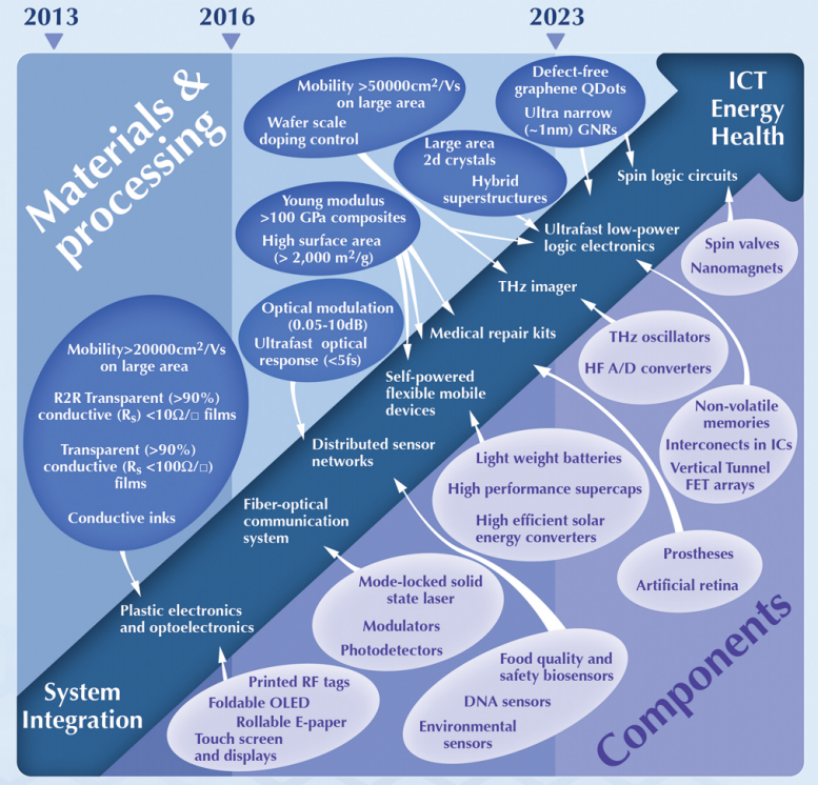

Figure 4: Roadmap for graphene applications, as seen by the Graphene Flagship [14].

To make graphene the next big thing in a certain domain, it has to be different from the already existing technologies. Taking for instance the use of graphene in electronic devices, the challenge is to find new territory completely dedicated to graphene's unique properties and where silicon could not compete with it. Not only from a theoretical point of view (some characteristics of graphene are more interesting than Silicon), but also from an industrial and economical point of view. Silicon based technologies are well mastered and mostly, very cheap. So, ex-

cept for some niche applications, graphene will only replace Silicon if it happens to be *really* better than this latter material.

To fully exploit the possibilities of graphene, the role of disorder has to be clarified. Only under very controlled conditions which are accessible in the lab, much less in the real world, graphene can be thought of as a truly 2-dimensional clean monocrystalline material. In reality, samples very often are polycrystalline. The mismatch between single crystals create grain bounderais which can drastically affect the pristine transport properties. Such grain boundaries (as well as many other graphene defects) are traps for external impurities, which can also affect the properties of clean graphene [15]. On the one hand, the role of this unwanted disorder has to be clarified, and on the other, by gaining this understanding, one could try to functionalize the material in a controlled fashion to tailor graphene to one's needs.

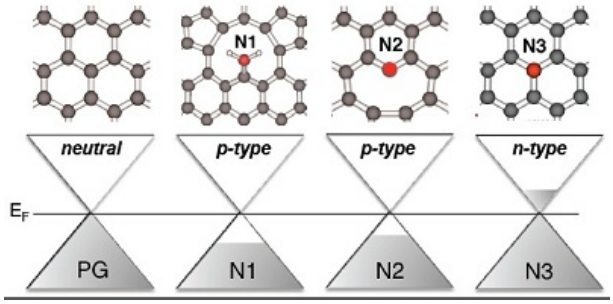

Figure 5: Different kinds of doping in graphene using nitrogen [16]. N3 displays the expected n-type behavior, using simple electron counting. N1 (nitrile-like) or N2 (pyridinic) behave as hole donors.

The effect of functionalization can also induce the effect known as doping. Depending on the kind of dopant, either neutral, n-type or p-type doping can be achieved. Not only the type of dopant, but also the local chemistry of a same dopant can affect the final behavior. This is exemplified in Fig. 5 where nitrogen can have both n or p type behavior. In addition of providing an excess of hole or electron charge carriers, doping can also open up a tunable bandgap which amplitude generally depends on the amount of charge being transfered [17]. The field of

graphene doping is vast, and several review papers cover the most recent advances in this field [18, 19].

An attempt to bring graphene closer to actual applications is thus by trying to firstly, understand its intrinsic properties, and secondly, trying to modify and improve its existing properties using external disorder. This Thesis covers several of the approaches to do so.

The QHE already mentioned at the beginning of this introduction can be considered one of the fundamental cornerstones of the physics specific to graphene. Indeed, as will be discussed later, the quantization of this phenomenon is different when measured in 2DEG's compared to graphene. In the early years of this phenomenon's study, before the rise of graphene, to role of disorder has been discussed thoroughly in inversion layers. Nevertheless, disorder has mainly been considered a necessary ingredient for the localization of states, ingredient to which one hadn't much control over. With the advent of graphene, and the straightforward access to functionalization because of its truly 2-dimensional structure, disorder can now be studied in more detail to appreciate its controlled effect on the QHE in graphene.

Two complement this introduction, and better appreciate the physics leading to the QHE, the reader is advised to read Chapter 2. An overview of the conventional quantum localization picture as well as the one specific to graphene is sketched in Section 2.1. In Section 2.2, a similar separation between 2DEGs and graphene is used regarding the QHE to present the literature from the time the effect was discovered up to state of the art discussing the most recent advances. Specific reference is made to literature discussing the lifting of the four-fold degeneracy of the landau levels.

Chapter 3 introduces the different computational tools required for the simulations in this Thesis.

Chapter 4 presents some of the first results accessible with our method, allowing to probe for experimentally realistic magnetic fields and sample sizes. In the past, through direct diagonalization, only unrealistically large fields were accessible [20]. F. Ortmann *et al.* [21] have recently proven the validity of the method on a system of sublattice-dependent

functionalized graphene, lifting the pseudospin degeneracy of the zero energy Landau level. This Chapter considers the simpler case where the sublattice symmetry is not broken, by studying un-reconstructed divacancies, a simplified model developed to better appreciate the results on epoxy oxygen in Chapter 5. Despite this absence of symmetry breaking, a surprising disorder and magnetic field dependent energy scaling of delocalized states is predicted.

In Chapter 5, the results obtained by functionalization of graphene with oxygen atoms in epoxy position are presented. The driving force behind this study was first to confirm the experimental hunch the group of Prof. A. Bachtold had when trying to explain their experiments on ozone treated graphene [22]. In a broader framework, the attempt of applying a high concentration of functionalization is to create strong disorder able to induce localization which could transform graphene into a transport gap insulator where the flow of electrons can be turned on and off, a necessary property for use in logic electronic devices.

In this same Chapter, the properties of the same system are studied under magnetic field. This complements and extends the QHE simulations on the divacancy case.

Chapter 6 covers the results obtained when functionalizing graphene with hydrogen. The objective of the study was to check if specific magnetoresistive transport signals could be calculated indicating possible coupling between magnetic moments. Such hydrogen functionalization has important applicability for energy storage in batteries and thus, a good understanding of the fundamental interaction is required. Moreover, this Chapter also discusses some unexpected transport features observed for different magnetic groundstates.

Finally, Chapter 7 gives an overview of the large class of disorder-specific transport properties. A comparison is given between the different effect of long and short range disorder. The difference between short and long range disorder is introduced from a theoretical point of view in Section 2.1.2 where the framework for weak (anti)-localization is set for the specific case of graphene.

Part I

Theory

Chapter 1

Graphene

1.1 Electronic Structure

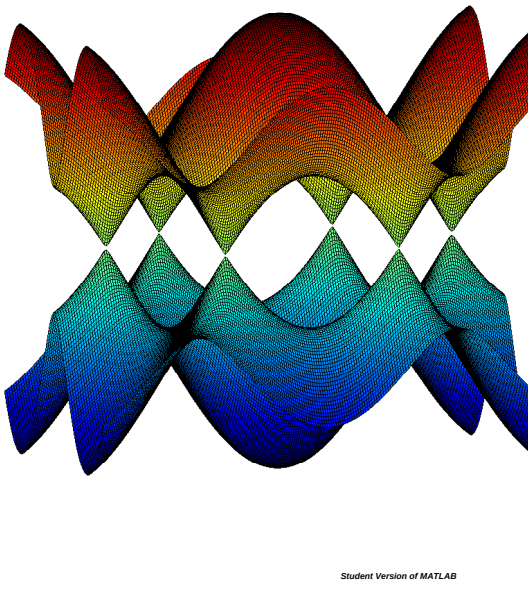

Figure 1.1: 3-dimensional electronic bandstructure of pristine graphene.

The electronic structure has already been discussed and reviewed in many review papers [23, 24, 25], so only a brief overview of the characteristic eletronic structure of graphene is given. Focus is driven towards the physics of interest to understand the high velocity in pristine graphene, the localization behavior due to possible intervalley mixing and the inequivalence between sublattices yielding peculiar transport signatures.

Figure 1.1 depicts the 3-dimensional electronic bandstructure within the first Brillouin zone, based on a simplified tight-binding (TB) model discussed in Section 1.2. In the field of electronic transport, only the region between -1 and 1 eV is of interest. From an electronic point of view, unrealistic charge concentrations would be required to go beyond this window. In this region, states are constrained in reciprocal space around specific high-symmetry points, which are classified into the K and K' group of points. At these points, in pristine graphene, the dispersion relation can be approximated by a linear relation between the energy E and the wave vector $\boldsymbol{k}$. The electronic structure is thus often described using the Dirac Equation which governs high energy physics where particels move at near speed of light. Charge carriers in graphene move also at very high velocity, albeit a fraction of the speed of light ($v_F \simeq c/300$). Nevertheless, graphene is also well modeled to a certain extent by conventional DFT where the Schrödinger equation is applied on the states of each orbital of each carbon atom. Specific Kohn-Sham-Dirac schemes have also been developed in litterature [26], improving the description at low energy due to the Dirac-like behavior, but obviously failing at higher energy due to absent σ orbitals which are not governed by the ultra-relativistic equation.

Before explaining how the Dirac equation arises from the peculiar geometry of graphene in Section 1.3, the tight-binding model is introduced in Section 1.2.

1.2 Tight-Binding Model

1.2.1 Pristine Graphene

As in any TB model to a solid, the strategy entails the representation of the electronic wave function of the solid (as described in Section 3.1 on DFT) by a linear combination of the wave functions of the constituent atoms [27, 28, 29].

Graphene contains two inequivalent atoms (labelled A and B) in the primitive cell. In real space, the unit cell is defined with the cell vectors

$$a_1 = a\left(\frac{\sqrt{3}}{2}, \frac{1}{2}\right) \text{ and } a_2 = a\left(\frac{\sqrt{3}}{2}, -\frac{1}{2}\right) \tag{1.1}$$

where a is the graphene lattice parameter (= 2.46 Å). Each atom A and B is surrounded by three atoms of the opposite type respectively (B and A).

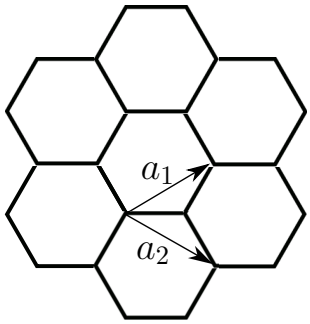

Figure 1.2: Real space representation of the unit cell of graphene

In reciprocal space, the unit vectors are

$$b_1 = b\left(\frac{1}{2}, \frac{\sqrt{3}}{2}\right) \text{ and } b_2 = b\left(\frac{1}{2}, -\frac{\sqrt{3}}{2}\right) \tag{1.2}$$

because $a_i \cdot b_j = 2\pi\delta_{ij}$.

The so-called sp^2 hybridization between atoms gives rise to the three σ bonds which are responsible for most of the mechanical properties of graphene, and to the dangling π bond, which governs the electronic

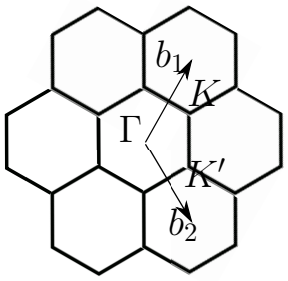

Figure 1.3: Reciprocal space representation of the unit cell of graphene

transport properties of the material. Close to the Fermi energy, the material can be well approximated including only the π orbital in the TB model.

For a single isolated carbon atom, the Schrödinger equation reads as

$$\hat{H} \left|\phi_{p_z}\right\rangle = E \left|\phi_{p_z}\right\rangle \tag{1.3}$$

Summing over all atoms on inequivalent A and B sublattices respectively yields:

$$\left|\psi_A\right\rangle = \sum_A D_A \left|\phi_{p_z,A}\right\rangle \tag{1.4}$$

$$\left|\psi_B\right\rangle = \sum_B D_B \left|\phi_{p_z,B}\right\rangle . \tag{1.5}$$

Using the linear combination assumption, the total wave function is given by

$$\left|\Psi\right\rangle = C_A \left|\psi_A\right\rangle + C_B \left|\psi_B\right\rangle \tag{1.6}$$

Using Bloch's theorem for periodic systems [29], Eqs (1.4) and (1.5) can be written as

$$\left|\psi_A(r)\right\rangle = \frac{1}{\sqrt{N}} \sum_A e^{i\boldsymbol{k}\boldsymbol{R_A}} \left|\phi_{p_z}(r - R_A)\right\rangle \tag{1.7}$$

$$\left|\psi_B(r)\right\rangle = \frac{1}{\sqrt{N}} \sum_B e^{i\boldsymbol{k}\boldsymbol{R_B}} \left|\phi_{p_z}(r - R_B)\right\rangle \tag{1.8}$$

where R_A and R_B give the positions of atom A and B and N is the number of unit cells. The sums are infinite if the samples are assumed to be of infinite size.

To express the Hamiltonian in the same basis as Ψ, the matrix elements associated with the two states $|\psi_A\rangle$ and $|\psi_B\rangle$, which are independent by definition, are calculated using:

$$H_{mn} = \left\langle \psi_m \middle| \hat{H} \middle| \psi_n \right\rangle . \tag{1.9}$$

Assuming only interactions between first neighbor carbon atoms, the sum is reduced on these 3 atoms, and the matrix elements are found as

$$H_{AA} = H_{BB} = \left\langle \phi_{p_z}(r - R_A) \middle| \hat{H} \middle| \phi_{p_z}(r - R_A) \right\rangle = \epsilon_z \tag{1.10}$$

$$\begin{aligned} H_{AB} = H_{BA}^{\star} &= \frac{1}{N} \sum \sum e^{i\boldsymbol{k}(\boldsymbol{R_B} - \boldsymbol{R_A})} \left\langle \phi_{p_z}(r - R_A) \middle| \hat{H} \middle| \phi_{p_z}(r - R_B) \right\rangle \\ &= \gamma_0 f(k) \end{aligned} \tag{1.11}$$

with the term $f(k)$ calculated from the positions depicted in Fig. 1.2:

$$f(k) = -(1 + e^{-i\boldsymbol{k}\cdot\boldsymbol{a}_1} + e^{-i\boldsymbol{k}\cdot\boldsymbol{a}_2}) \tag{1.12}$$

The Hamiltonian in the TB basis in the first neighbor approximation is thus given by

$$\hat{H} = \begin{pmatrix} \epsilon_z & \gamma_0 f(k) \\ (\gamma_0 f(k))^{\star} & \epsilon_z \end{pmatrix} . \tag{1.13}$$

This brief analysis shows that the two quantities of interest in a TB model are the onsite energy ϵ_z and the hopping terms γ_0.

Solving the Schrödinger equation for this Hamiltonian gives access to the k-dependent energy eigenvalues. For this simple model, a simple analytical expression can be found:

$$E_{\pm}(k) = \frac{\epsilon_z - s_0 \gamma_0 f(k)^2 \pm (\gamma_0 - s_0 \epsilon_z) |f(k)|}{1 - s_0^2 f(k)^2} \tag{1.14}$$

where the overlap $s_0 = \langle \phi_{p_z}(r - R_A) | \phi_{p_z}(r - R_B) \rangle$ is often neglected close to the Dirac point, reducing Eq. (1.14) to

$$E_{\pm}(k) = \epsilon_z \pm \gamma_0 \, |f(k)| \tag{1.15}$$

Thus, firstly, the value of ϵ_z only induces a rigid shift of the electronic bandstructure. Secondly, and more striking, is the behavior at the high symmetry points K and K'. The manifolds with positive and negative sign in Eq. (1.15) touch exactly at these two inequivalent points. Moreover, for low energy excitations, the spectrum is linear. For electrons in 2DEG (hosted by semiconductor heterostructures), the behavior is strikingly different, being quadratic with momentum.

1.2.2 Strained Graphene

In this Thesis, when trying to understand some peculiar results, an analogy with strained graphene was proposed. In the end, the assumptions leading to this analogy were not applicable, so the following model was not used (see Appendix D). Nevertheless, the developmment of this model has pedagogical value, so its derivation and associated implications are very briefly presented in this Section.

Straining graphene or adding an oxygen atom in bridge position on pristine graphene both have the effect of changing the hopping terms. Assuming uniaxial strain in the x direction, only γ_1 in Fig. 1.4 is modified. The two other hopping terms are not affected in first approximation. More elaborate impurities which would break the A and B sublattice symmetry induce a modification of the onsite energies associated with these sublattices. In the case of epoxy, sublattice symmetry breaking is not present, but *locally*, the symmetry is nevertheless broken with respect to the hopping terms. This is straightforward looking at the equivalent model developed from the full TB model for epoxy oxygen described in Cresti et al. [30] and further used in Appendix D.

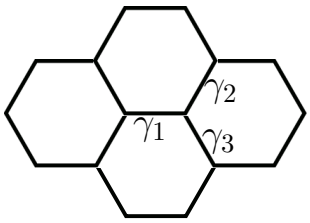

Figure 1.4: TB parameters for three inequivalent hopping terms γ_1, γ_2 and γ_3.

With inequivalent hopping terms (and setting the onsite energy to zero), an expression similar to Eq. (1.15) is found:

$$E^2 = \gamma_1^2 + \gamma_2^2 + \gamma_3^2 + 2\gamma_1\gamma_2\cos(2\pi k_1) + 2\gamma_1\gamma_3\cos(2\pi k_2) + 2\gamma_2\gamma_3\cos\left[2\pi(-k_1 + k_2)\right]. \tag{1.16}$$

While a change of onsite energy between A and B sublattice opens up a gap, the behavior when changing the hopping terms is a bit different. Simply changing the value of γ_1 while keeping γ_2 and γ_3 equal to γ_0 can already give rise to interesting physics. For instance, if $\gamma_1 < 2\gamma_0$, Fig. 1.5 shows the Dirac cones start to move towards eachother.

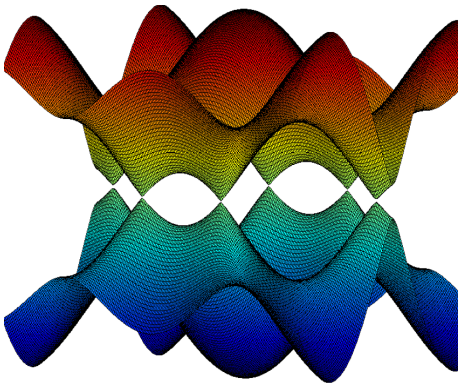

Figure 1.5: Strained Graphene: $\gamma_1 = 1.5\gamma_0$

Increasing the value of γ_1 to exactly $2\gamma_0$ merges the Dirac points two by two, and creates a perfect anisotropy where in one direction, a linear dispersion is preserved, and in the other, a quadratic behavior has appeared (see Fig. 1.6).

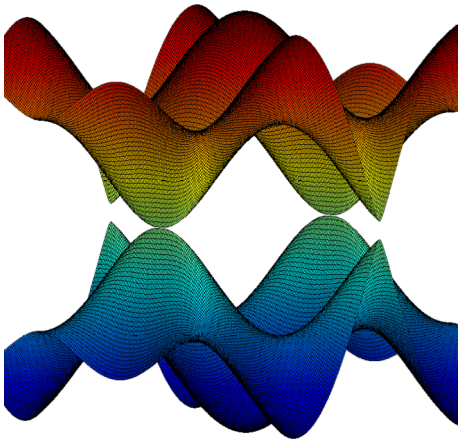

Figure 1.6: Strained Graphene: $\gamma_1 = 2\gamma_0$

Finally, if $\gamma_1 > 2\gamma_0$, a gap opens up (Fig. 1.7).

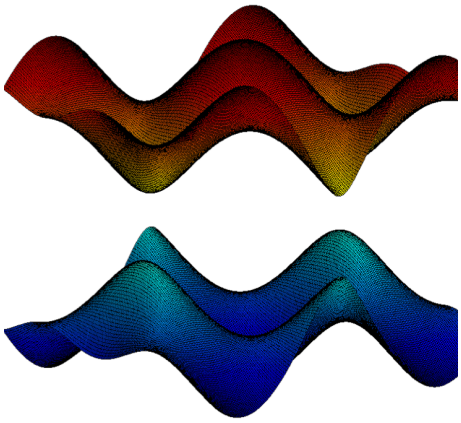

Figure 1.7: Strained Graphene: $\gamma_1 = 3\gamma_0$

In fact, theoretical literature discussing such change in hopping term is prolific (see for instance Ref. [31, 32, 33, 34, 35, 36]) as well as experi-

mental realizations of Dirac cone merging by a microwave tight-binding analogue experiment of a graphenelike lattice [37] or by using cold adotams in a laser field [38]. In graphene, doubling the hopping term in one direction using strain would break the sample. Inducing strain by chemical modification would probably also have some undesired side-effects destroying the Dirac cone structure before any merging occurs. Nevertheless, Kubo transport simulations on such systems might unveil interesting anisotropic behaviors before rupture.

1.3 Dirac-Weyl Equation

Starting from Eq. (1.13) where the diagonal elements where set to zero by applying a rigid shift of the reference energy, and linearly expanding it around K' and K, gives:

$$H_K = \hbar v_F \begin{pmatrix} 0 & k_x - ik_y \\ k_x + ik_y & 0 \end{pmatrix} = v_F(p_x\sigma_x + p_y\sigma_y) \tag{1.17}$$

where $p_x = \hbar k_x$ and σ are the Pauli matrices. In more compact form, a formula very similar to the Dirac equation is found:

$$H_K = v_F \hat{\sigma} \cdot \boldsymbol{p} \tag{1.18}$$

if $\boldsymbol{p}$ would be replaced by $-i\hbar\nabla$.

Because the wavefunction is described by a spinor, the electrons have what is called a pseudospin, in analogy with the spin degree of freedom in high energy physics [39]. This pseudospin is directly related to the respective sublattices.

The fact graphene is described by the Dirac equation leads to two interesting properties. Firstly, based on the same formalism as in the previous Section 1.2.1, the contribution to backscattering is calculated to be zero for long range impurities. Long range disorder does not affect the pseudospin degree of freedom. This has quite a dramatic effect which allows for coherent transport in graphene (see Section 2.1.2 for details). This is in striking opposition to other conventional materials

where disorder governs the scattering events affecting electronic transport. In graphene, short-range disorder is required to induce for instance quantum localization effects. These physics are discussed later on in Section 2.1. Secondly, when electrons with energy E impinge on a potential V (with $E < 2V$), they do not behave like Schrödinger particles in a box. Instead of having an exponentially low tunneling probability, these Dirac electrons can tunnel with a probability equal to one for $V \to \infty$, at certain angles. This process is called Klein Tunneling, and literature about this phenomenon is abundant (see for instance Ref. [40]).

Chapter 2

New 2-Dimensional Physics

In following Sections, the two most important physical phenomena encountered during this Thesis are discussed from a theoretical point of view. Section 2.1 covers the physics behind the weak localization phenomenon, while Section 2.2 covers the Quantum Hall Effect.

2.1 Quantum Localization Effects

2.1.1 General Picture

Up to the 1980s, the general belief was that interference effects played no role in condensed matter physics. The picture set up by Drude stated that, for a certain disorder conformation, subsisting interference effects would disappear upon averaging over many disorder realizations. Consequently, a classical approach to the transport behavior in metals seemed sufficient. With the discovery of the Aharonov-Bohm effect, this view appeared to be flawed. Other interference effects have since been observed in the realm of mesoscopic physics. These physics are at the interface between the nanoscopic world containing a very limited amount of atoms but where quantum physics are important and the microscopic world where a large amount of atoms are interacting through the classical laws of physics. At the interface, a large amount of atoms obey the quantum laws of physics.

Based on the book by Akkermans *et al.* [41], the plane wave with incident wave vector $\mathbf{k}$ and reemitted wave vector $\mathbf{k}'$ is written as

$$A(\mathbf{k},\mathbf{k}') = \sum_{\mathbf{r}_1,\mathbf{r}_2} f(\mathbf{r}_1,\mathbf{r}_2) e^{-i(\mathbf{k}\cdot\mathbf{r}_1 - \mathbf{k}'\cdot\mathbf{r}_2)} \tag{2.1}$$

where the amplitude $f(\mathbf{r}_1,\mathbf{r}_2)$ describes the propagation of a plane wave between two scattering centers located at $\mathbf{r}_1$ and $\mathbf{r}_2$. To go from $\mathbf{r}_1$ to $\mathbf{r}_2$, all paths need to be considered yielding

$$f(\mathbf{r}_1,\mathbf{r}_2) = \sum_j |a_j| e^{i\delta_j}. \tag{2.2}$$

The associated wave intensity can be calculated as

$$|A(\mathbf{k},\mathbf{k}')|^2 = \sum_{\mathbf{r}_1,\mathbf{r}_2} \sum_{\mathbf{r}_3,\mathbf{r}_4} \sum_{jj'} |a_j||a'_j| e^{i(\delta_j - \delta'_j)} e^{i(k\cdot r_1 - k'\cdot r_2)} e^{-i(k\cdot r_3 - k'\cdot r_4)}. \tag{2.3}$$

All terms in Eq. (2.3) vanish for a random distribution of phase differences $\delta_j - \delta'_j$. These differences measure the difference between the lengths of all available paths. The only non-vanishing terms correspond to a phase difference equal to zero, *i.e.* pairs of identical trajectories, and can be classified into two types. The first type, where $r_1 = r_3$ and $r_2 = r_4$, contributes

$$|A(\mathbf{k},\mathbf{k}')|^2 = \sum_{\mathbf{r}_1,\mathbf{r}_2} |f(\mathbf{r}_1,\mathbf{r}_2)|^2 \tag{2.4}$$

to the intensity, while the second type, where $r_1 = r_4$ and $r_2 = r_3$ adds a phase dependent contribution

$$|A(\mathbf{k},\mathbf{k}')|^2 = \sum_{\mathbf{r}_1,\mathbf{r}_2} |f(\mathbf{r}_1,\mathbf{r}_2)|^2 e^{i(k+k')\cdot(r_1 - r_2)} \tag{2.5}$$

to the intensity. In the classical framework of the Boltzmann equation, only the term in Eq. 2.4 is taken into account. In Eq. 2.5, two situations can happen. Either $k + k' \simeq 0$ in which situation *coherent backscattering* occurs, either $r_1 = r_2$ in which the origin of weak localization is found.

2.1.2 Graphene

The localization picture in graphene [42] is a bit more complicated because of the pseudospin component and because of the chirality of the charge carriers (locking their momentum either parallel or anti-parallel to the direction of the pseudospin). Furthermore, graphene has two flavors of the gapless Dirac-like spectrum (known as valleys) and the chirality of the carriers is opposite depending on which inequivalent valley is being occupied.

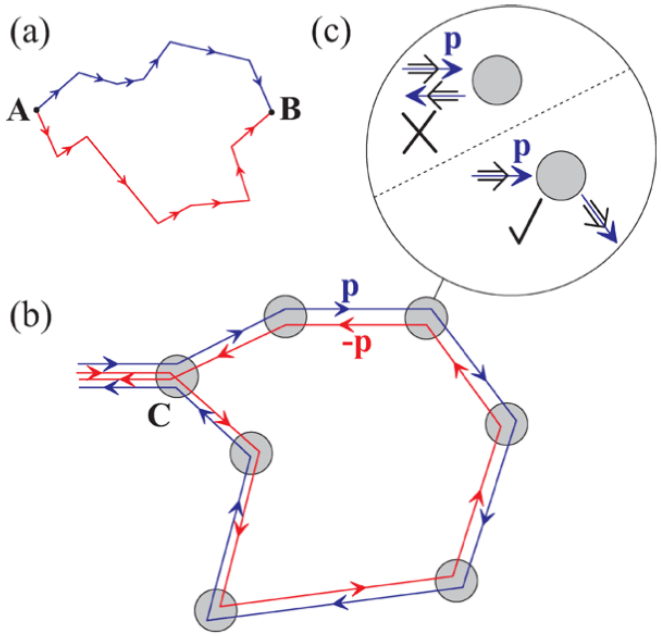

Figure 2.1: (a) Two classical paths to go from A to B. (b) Closed path with counterpropagating charge carriers, leading to localization correction. (c) Probited backscattering in the case of long-range disorder. Figure taken from [42]

In the presence of long-range disorder, which cannot differentiate between neighboring atoms, the pseudospin is not affected. The conservation of pseudospin thus does not allow to scatter the chiral particles in the backward direction and the pseudospin remains parallel to the momentum [see panel (c) of Fig. 2.1]. For the clockwise direction of the

closed path [see panel (b)], the pseudospin rotates by an angle of π and for the anticlockwise direction by an angle of $-\pi$. This net difference in the rotation of pseudospin of 2π induces a phase difference of π for spin-1/2 fermions. The electons are thus out of phase and change the conventional constructive interference in 2DEG's in destructive interference for graphene. Thus, long-range disorder induces weak anti-localization.

By allowing for intravalley scattering, which allow for pseudospin symmetry breaking, different phases are acquired along the paths which destroy the phase difference acquired on both paths, thus destroying any interference effects.

However, if intervally scattering is possible, counterpropagating paths can occupy opposite valleys. The two valleys have opposite chirality, and thus, the acquired phases are equal leading to constructive interference. Short-range scattering inducing intervalley scattering can thus restore the conventional weak localization behavior.

2.2 Quantum Hall Effect

At around 2:00 AM, during the night of the 4th to the 5th of February 1980, as he states in his foreword for the book on the Quantum Hall Effect by R. Prange and S. Girvin [43], Klaus von Klitzing made the discovery that Hall resistance plateaus are unexpectedly constant and reproducible when measured on inversion layers. Originally, he wanted to find Anderson localization effects, instead he found a much more intricate behavior between these localization effects and their interplay with persistent currents which are a *sine qua non* condition to observe the quantization of the transverse conductance given by integer multiples of the fundamental constants e^2/h (with e the elementary charge and h the Planck constant). He was rewarded with the Nobel Prize in Physics in 1985 for his discovery.

This discovery has sparked more than a decade of very active research to understand the physics underlying this intriguing phenomenon. A lot of theoretical literature is thus available, dating back to the early eighties. In 2004, when graphene is first sythesized and characterized, namely

with such transverse conductance measurements, the QHE came back at the forefront of both theoretical and experimental research. Graphene being the first truly 2-dimensional material [as opposed to an inversion layer behaving like a 2D Electron Gas (2DEG)], the surface states are readily accessible for direct measurements, providing thus an ideal candidate to study the QHE.

Section 2.2.1 discusses the QHE from a general point of view, valid for all kinds of 2DEG's, while Section 2.2.2 focuses on its application to graphene. The Hall bar geometry is assumed. Specific attention is given towards the litterature on percolation of localized states, as these may help better appreciate the results obtained within this Thesis on highly disordered graphene.

2.2.1 Two-Dimensional Electron Gas

From Classical to Quantum

In the classical Hall Effect, electrons flowing in the x direction with current density j_x, are deflected towards the y direction by the magnetic field applied in the z direction under the influence of the Lorentz force $F_y = -ev \times B/c$ generating the resistivity tensor

$$\boldsymbol{\rho} = \begin{bmatrix} \rho_0 & \frac{B}{nec} \\ -\frac{B}{nec} & \rho_0 \end{bmatrix} \tag{2.6}$$

with n the charge carrier density and $\rho_0 = 1/\sigma_0 = m/(ne^2\tau_0)$. τ_0 is the mean free time and e the electronic charge. The only quantum effects that enter into account for the classical picture are through the bandstructure which can change the effective mass of the electrons and possibly through a change of the mean free path.

However, for the quantum case, the electrons are governed by the Schrödinger equation [Landau gauge $\boldsymbol{A} = (-yB, 0, 0)$] where the wave function

$$\Psi \propto e^{ikx}\varphi(y), \tag{2.7}$$

because the potential does not involve an x-dependent component, so plane wave dependence on x can be assumed:

$$\frac{\hbar\omega_c}{2}\left[-l_B^2\frac{\partial^2}{\partial y^2}+\left(\frac{y}{l_B}-l_Bk\right)\right]\varphi_n=E_n\varphi_n \tag{2.8}$$

which thus takes the form of a (shifted) harmonic oscillator. The magnetic length $l_B=\sqrt{\frac{\hbar c}{eB}}$ is introduced as well as the cyclotron frequency $\omega_c=\frac{eB}{m}$. The different oscillator lengths, labeled by $n=0,1,2,\ldots$, define the Landau levels. The corresponding energy levels are given by

$$E_n=\hbar\omega_c(n+\frac{1}{2}) \tag{2.9}$$

(independent of k) and are thus linear with B through ω_c defined above. The total number of states of a full Landau level can be calculated to be

$$n_B=\frac{1}{2\pi l_B^2}=\frac{eB}{hc}. \tag{2.10}$$

and is thus increased by increasing the magnetic field. The quantum effects are responsible for the quantization reflecting in the Landau levels. The states in the y direction are confined and the ones in x directions are either extended or localized because of the massive degeneracy of states inside the Landau level. The *filling factor* is defined by $\nu=\frac{n}{n_B}$. If, for the ideal case where ν is an integer, $n=in_B$ is replaced in Eq. (2.6) and yields, by matrix inversion, the conductivity tensor

$$\boldsymbol{\sigma}=\begin{bmatrix}0 & -i\frac{e^2}{h}\\ i\frac{e^2}{h} & 0\end{bmatrix} \tag{2.11}$$

which governs the QHE. If the Landau level is not completely filled, the filling factor does not equal an integer, and the Hall conductivity is located in between two plateaus.

Impurity Effects

General considerations Formally, based on relativistic transformation arguments [44] which require breakdown of translational invariance,

and intuitively, based on the requirement of localization, impurities can play on important role to observe the QHE.

Under magnetic field, electrons move in circles (the classical cyclotron radius v_F/ω_c is replaced by the magnetic length l_B for the quantum picture). If only a few impurities are present, some electrons will circle forever in regions away from any impurities, and their energy is given by Eq. (2.9), while others are under the influence of an impurity potential and thus suffer an energy shift given by the complex part $i\frac{\hbar}{\tau_0}$ (with τ_0 the scattering time). The first effect of the impurities is thus to broaden the Landau levels around the values of E_n.

Extending the analysis in Section 2.2.1 by adding the effect of an external electric field in the y direction and adding a single-impurity δ-potential, the eigenenergies are determined by [45]

$$1 = 2\pi \sum_{nk} \frac{|\psi_{nk}(0)|^2}{E_\alpha - E_{nk}} \tag{2.12}$$

where E_{nk} includes the energy shift induced by the electric field and the wavefunctions are given by

$$\psi_{nk}(x,y) \propto e^{ikx}\phi_{nk}(y + \frac{ce}{B}). \tag{2.13}$$

Without going through the details (see [43]), the solutions to Eq. (2.12) are described. Each impurity solution E_α lies in between the unperturbed levels with energy E_{nk}. There is exactly one state which is completely localized because of the single impurity. This state lies furthest away from the original Landau level position $n\hbar\omega_c$, and, because it is completely localized, it carries no current, so it is of no importance whether the state is occupied by an electron or not. All other states are constrained to lie very close to the unperturbed energy and are extended. Most important, the extended states carry an extra Hall current which exactly compensates for that not carried by the localized state. This ensures quantization is disorder independent. The current carried

by the extended states is given by

$$\begin{aligned} I &= -\frac{e}{h}\sum_{np}(E_{np+1} - E_{np}) \\ &= \frac{e}{h}\sum_{n}(E_{np_{\max}} - E_{np_{\min}}) \end{aligned} \tag{2.14}$$

with $p_{\max/\min}$ referencing respectively the upper and lower edge state. Although the second line indicates only edge state energies appear in the calculation of I, the first line clearly indicates bulk states do participate to transport.

Increasing the number of impurities (and associated δ-potentials) to a value of M ($< N$, N being the total number of states), the number of extended states is reduced to $N - M$. As long as all extended states are occupied, the current remains the same. Electrons passing close to the impurity speed up and carry just enough current to compensate for the current not carried by the localization [43].

If the core of extended states in each Landau level is separated by an energy gap containing only localized states, Laughlin [46] shows that (i) extended states indeed exist at the core of the Landau levels, and (ii), if these states are occupied, they carry all the current necessary to compensate for the localized states.

Sufficient conditions on disorder for robust QHE In the previous paragraph, the importance of disorder to observe the QHE was highlighted. Neverthless, some kinds of disorder may be detrimental to the QHE, and a more in depth analysis is required [47]. More specifically, three different impurity potentials, namely a *weak potential* V_W, a *scattering potential* V_{SC} and a *smooth potential* V_S, are shown to be sufficient conditions to observe the QHE. This also means each potential that can be written as a sum of these three terms satisfies the necessary conditions:

$$V = V_W + V_{SC} + V_S \tag{2.15}$$

Such potentials allow for the observation of mobility edges which separate the extended from the localized states. In this paragraph, the

physical behavior of these extended and localized states is discussed for the different potentials. Fig. 2.2 depicts their behavior.

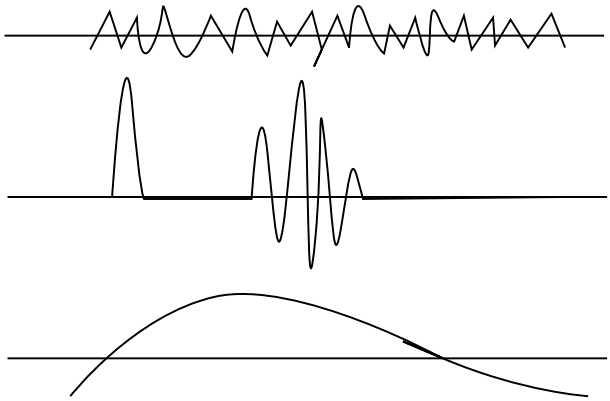

Figure 2.2: Different types of disorder, classified as weak potentials V_W (top), scattering centers V_{SC} (middle) and smooth potentials V_S (bottom).

Weak potential To be considered as weak, a potential must satisfy the *weakness condition* [48, 49]

$$\max |V_W(r)| \equiv V^{\max} \ll \hbar\omega_c. \tag{2.16}$$

Considering the Hamiltonian

$$H = H_0 + \lambda V_W \tag{2.17}$$

where the parameter λ varies from zero to one, and the corresponding eigenenergies $E(\lambda)$, using the Feynman-Hellmann theorem, the following equation has to be satisfied:

$$\frac{dE}{d\lambda} = \langle V_W \rangle . \tag{2.18}$$

Integrating Eq. (2.18) from zero to one yields that the energies satisfying the Hamiltonian H differ from the unperturbed levels $n\hbar\omega_c$ by at most $V^{\max}$. Noting the condition in Eq. (2.16), it trivially proves that there are no states in the central region between two Landau levels. An

absence of states between two levels and using the Laughlin-Harperin argument (see end of the **General considerations** paragraph) implies naturally the existence of mobility edges. Also, these extended states for finite B are different from the zero B-case where any random potential ends up localizing states in two dimensions.

Scattering potential Scattering potentials can be of arbitrary strength and variation which vanishes outside the scattering region. A very important further condition that such potential has to satisfy according to [47, 50, 51] is that a potential-free region of minimum width d has to percolate troughout the system, where

$$d \gg l_B. \tag{2.19}$$

Otherwise, the following picture for the extended and localized states does not hold. Based on wavepacket considerations which move throughout the sample due to an electric field, the states associated with these wavepackets are proven to only scatter forward when reaching a scattering region. Because of the elastic scattering, the incoming wavepacket and the outgoing wavepacket are required to have the same energy. The moving wavepacket has no sufficient kinetic energy to escape the localization energy induced by the magnetic field. However, because of the electric field, one state with wavevector k has a potential energy of vk (with v the group velocity) along the line $y = k$ on which it is localized. When reaching the scattering center, this equipotential line energy circumvents the scattering center and recovers its y positioning when leaving the scattering region, after which the wavepacket continues in the same direction as the incoming wave. This is proven in a more formal way in Note 1 of Chapter 3 in Ref. [43]. This behavior is sketched in Fig. 2.3.

So, as long as this impurity free region is *large enough* to allow for full recovery, extended states are not hindered by the presence of these scattering centers. And thus, the latter do not hinder the development of the QHE. The necessity to be *large enough* is different from the zero magnetic field case. Actually, the condition in Eq. (2.19) is less stringent

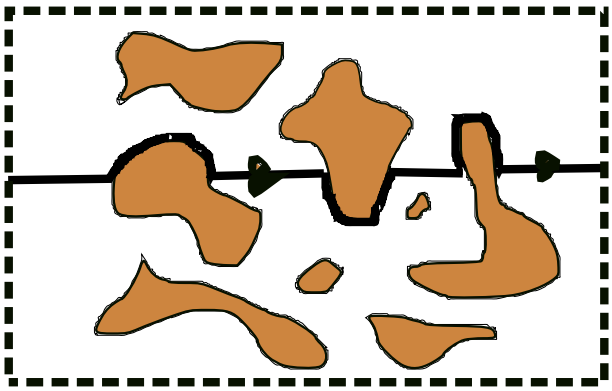

Figure 2.3: Schematic wave packet representation of delocalized states through a scattering potential (brown zones) distributed randomly in pristine sample (white). Black line with arrows indicate the path followed by a wave packet of wavevector $\boldsymbol{k}$ on the corresponding equipotential line.

here than in zero field where the characteristic length l_e is usually larger than l_B.

Smooth potential A potential is required to be smooth in the sense that [47, 52, 53, 54, 55, 56, 57, 58, 59]

$$|\Delta V_S| = \frac{\hbar\omega_c}{l_B}. \tag{2.20}$$

To allow for a robust QHE, a more exotic explanation for the role of this kind of disorder is required to sustain extended states. Extended states can only be understood in terms of a continuum percolation model. For sake of simplicity, and to avoid introducing the percolation theories formally (for reviews, see[60, 61]), only a simple intuitive argument is presented.

In a smooth potential, the equipotential lines already mentioned in previous paragraphs and sections, are following the relief of the well separated potential maxima and minima. This is visually very similar to a contour map used by the military for instance. For high energies, the equipotential lines will be closed curves around the tops of the potential hills. The closed curves at the bottom of the valleys will correspond to

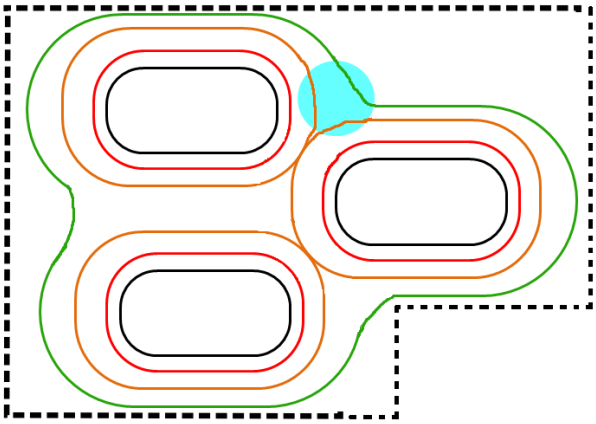

Figure 2.4: Smooth potential sketch. Localized states in red and orange, delocalized state in green. Blue circle indicates an avoided crossing.

lower energies. Closed curves of same energies which lie far away from each other do not talk to each other and are as such perfectly localized. For the extended states, the argument is a bit more tricky. Since equipotential lines cannot cross, the curve of lower energy in Fig. 2.4 is covering a larger surface because it has to avoid such crossing. For a sample of infinite size, at zero electric field, there can be an extended state for at most one energy. Invoking the Laughlin-Harperin gauge argument, it is proven that mobility edges exist and consequently, the QHE can develop in such potential.

Experiment As reference to the seminal work by K. v. Klitzing [62], data from his first observation of the QHE are plotted in Fig. 2.5. Liquid Helium temperatures were necessary and measurements were performed on a thin sheet of semiconducting material. Quantization of the Hall resistance following the Landau level structure is observed, unaffected by the details of the material (see previous paragraphs for the different disorder models that do not affect the quantization).

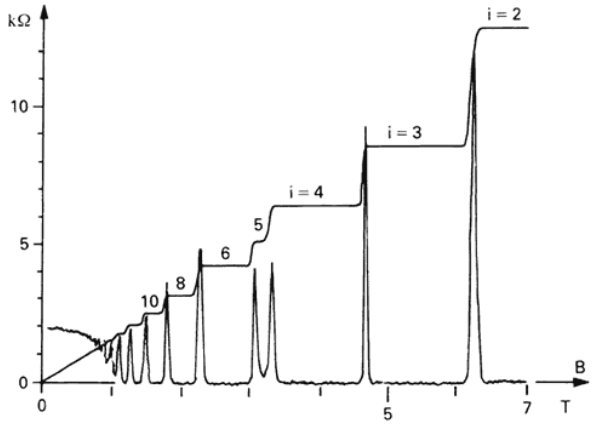

Figure 2.5: Experimental figure taken from the paper by K. v. Klitzing *et al.* [62]. Sample independent quantization of the Hall resistivity is observed.

2.2.2 Graphene

As introduced from a general point of view in the previous Section, the quantization induced by the energy seperation between delocalized and localized states induces the appearance of a Landau level spectrum. In conventional 2DEG's, the energy seperation between Landau levels follows a linear scaling law with magnetic field B [See Eq. (2.9)]. In graphene however, because of the linear dispersion at the Dirac point, the scaling has a $\sqrt{B}$ behavior giving rise to an anomalous quantized Hall conductivity [24, 63, 64]. Figure 2.6, taken from [24], shows this anomalous quantization for single layer graphene (mainframe). The unconventional quantization rule is given by

$$\sigma_{\mathrm{xy}} = \left(n + \frac{1}{2}\right) g_s \frac{e^2}{h} \tag{2.21}$$

in contrast with the 2DEG QHE where the 1/2 shift and the four-fold degeneracy ($g_s = 4$ for graphene) are absent. In the high magnetic field regime, graphene maintains it symmetric electron/hole energy spectrum, which includes a zero energy Landau level (where electrons and holes

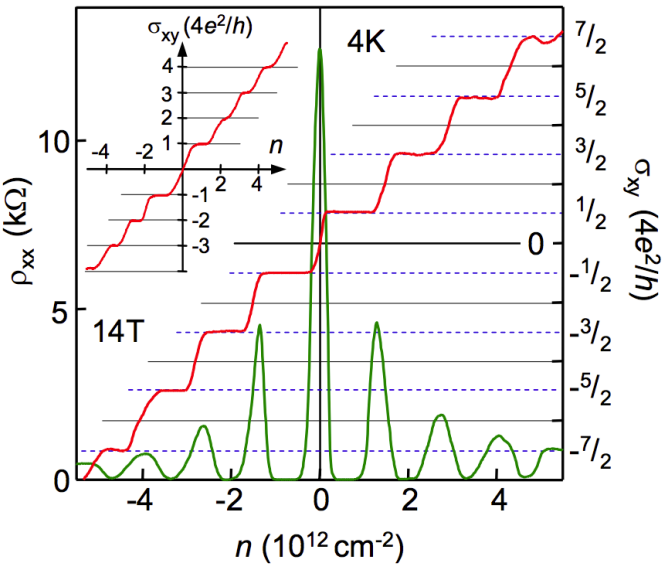

Figure 2.6: QHE for massless Dirac fermions. Both the Hall conductivity and longitudinal resistivity are depicted. Mainframe: monolayer graphene. Inset: bilayer graphene. $B = 14$T. Figure taken from [24]

coexist), and non-equidistant Landau levels (LLs), with energies

$$\varepsilon_n = sgn(n)\sqrt{2\hbar {v_F}^2 eB|n|}, \tag{2.22}$$

where $v_F = 10^6 \mathrm{ms}^{-1}$ is the Fermi velocity, B is the magnetic field and n is the integer LL index [65, 66].

Several symmetry-breaking mechanisms can lift the four-fold degeneracy of LLs [67, 68]. In particular, the presence of an additional quantized Hall plateau $\sigma_{xy} = 0$ at low energy in high-mobility samples has been tentatively analyzed in terms of energy-splitting (gap) of the zero-energy LL, either driven by Zeeman interaction (spin degeneracy lifting) or the formation of quantum Hall ferromagnetism [69, 70, 71]. By modifying the sublattice symmetry, the valley-degeneracy can be lifted as well. Fig. 2.7 depicts such lifting based on calculations using the same formalism described in Section 3.3.

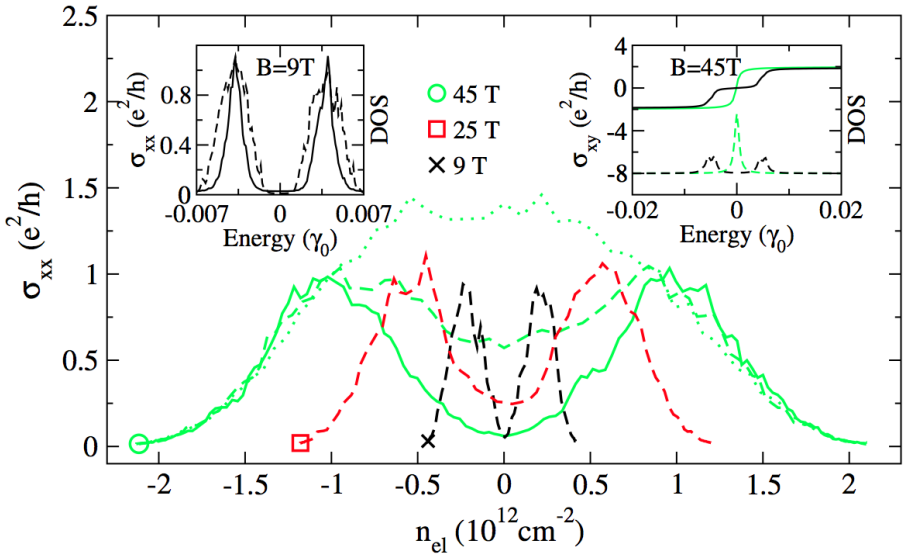

Figure 2.7: Sublattice symmetry breaking in graphene induces a splitting of LL0 (mainframe) and the appearance of a zero energy plateau (inset). Figure taken from [21]

The scaling of the zero-energy split gap with magnetic field remains however theoretically and experimentally debated, with a behavior changing from linear to $\sqrt{B}$-like, depending on the underlying dominant symmetry breaking or on the sample quality [71, 72]. In highly disordered graphene, a crossover from the Efros-Shklovskii to Mott variable-range hopping has been reported and related to a localization length exceeding the screening length, thus elucidating the nature of transport at the Hall plateau transition and emphasizing the important role of disorder [73]. The existence of a metal-insulator transition (MIT) is actually a central aspect of the quantum Hall effect (QHE) theory, which requires the robustness of electronic states at the center of Landau level, which have peculiar multifractal properties (*critical states*) (See Refs. [74, 75] and Section 2.2.1 for general condiderations on the effect of disorder). The recent observation of a quantized Hall conductance in highly resistive (millimeter-scale) hydrogenated graphene, with mobility less than 10cm^2/V.s and estimated mean free path far beyond the Ioffe-Regel limit, even suggests some unprecedented robustness of the

QHE in strongly damaged graphene, a fact which crucially demands for theoretical inspection and analysis of the related MIT [76].

On the other hand, in absence of magnetic fields, adsorbed impurities and defects are found to produce a large variety of additional transport features in graphene, such as resonant tunneling, mobility gaps, and electron-hole asymmetry (see for instance [77, 78, 79, 80]). Available high-field magnetotransport experiments in graphene also present frequently some weak electron-hole asymmetry together with some variability in σ_{xx} [81, 82, 83], which could hint towards a signature of specific impurities. See Fig. 2.8 for illustration of such asymmetry. However, no connection with specific disorder has been established so far. Besides, the possibility of tuning QHE fingerprints by intentional disorder (chemical functionalization, controlled doping,...)[84, 85, 86] would certainly allow a richer exploration of the metal-insulator transition and the QHE phase diagram in two-dimensional systems, which could be interesting for metrology issues [87, 88, 89].

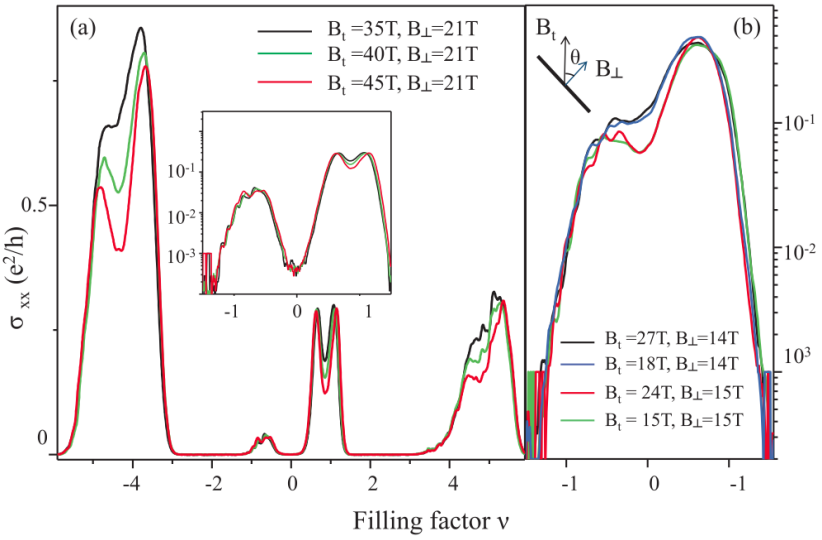

Figure 2.8: Experimental figure taken from the paper by A. J. M. Giesbers *et al.* [83]. This experiment shows that the zero Landau level here is not sensitive to spin degenaracy lifting as the curves do not change when changing the magnetic field orientation. Only the higher energy LLs are changing with the angle of the field.

Chapter 3

Computational Tools

In the following Sections, the different computational tools used in this Thesis are described.

3.1 Density Functional Theory

In this Section, a general introduction to the Density Functional Theory (DFT) is presented. Within this Thesis, DFT has mainly been used to understand the local influence of the impurity potential induced by an oxygen atom in epoxy position. The advantage of this method is its great accuracy related to the fact that calculations are performed based on first-principles where no external parameters are required. At the same time, the cost of this great accuracy explains why the samples of mesoscopic sized cannot be treated within this formalism. To take profit of the accuracy of DFT while limiting the computational cost, TB parameters are extracted using fits to the *ab initio* calculations. In Section 3.1.1, the Born-Oppenheimer approximation is explained, which already diminishes the cost within the *ab-initio* part of the simulations. In Section 3.1.2 and 3.1.3, the Hohenberg-Kohn theorem and Kohn-Sham equations are discussed which underly DFT.

3.1.1 Born-Oppenheimer Approximation

To fully characterize a quantum mechanical system, the many-body wavefunction Ψ_i^{MB} for each particle i can be used which has to satisfy the time-independent Schrödinger equation

$$\hat{H}^{\mathrm{MB}}\Psi_i^{\mathrm{MB}} = E_i\Psi_i^{\mathrm{MB}}. \tag{3.1}$$

This Hamiltonian contains both a kinetic $\hat{T}$ and potential energy $\hat{V}$ term given by

$$\hat{T} = -\sum_{i=1}^{N}\frac{\hbar}{2m_i}\nabla_{r_i}^2 \tag{3.2}$$

and

$$\hat{V} = \frac{1}{4\pi\epsilon_0}\sum_{i=1}^{N}\sum_{j>i}^{N}\frac{q_i q_j}{|r_i - r_j|}. \tag{3.3}$$

with the mass m_i and charge q_i of each particle. Positions are given by coordinates r_i.

Eq. (3.1) contains thus the particles' motions which are correlated through the potential energy. Solving this would be computationally practically impossible, thus a first approximation is required which leads to the essence of DFT. This approximation bears the name of the scientists Born and Oppenheimer who proposed it. Their idea was to take advantage of the fact that the masses of the nuclei are at least 3 orders of magnitude larger than the mass of the electrons. The dynamics of both these particles are thus very different which allows to safely decouple the wave function into consituent parts of electronic and nucleic wavefunctions

$$\Psi^{\mathrm{MB}}\left(\{r_i\},\{R_j\}\right) = \Psi^{\mathrm{el}}_{\{R_j\}}\left(\{r_i\}\right)\Phi\left(\{R_j\}\right) \tag{3.4}$$

with the positions of the electrons given by r_i and the positions of the nuclei by R_j. Discernating between nuclei and electrons, separates the full Hamiltonian into:

$$\hat{H}^{\mathrm{MB}} = \hat{T}^{\mathrm{el}} + \hat{T}^{\mathrm{nucl}} + \hat{V}^{\text{el-el}} + \hat{V}^{\text{nucl-el}} + \hat{V}^{\text{nucl-nucl}}. \tag{3.5}$$

where

$$\hat{T}^{\text{el}} = -\sum_{i=1}^{N_e} \frac{1}{2}\nabla_{r_i}^2 \tag{3.6}$$

$$\hat{T}^{\text{nucl}} = -\sum_{i=1}^{N_n} \frac{1}{2M_i}\nabla_{R_i}^2 \tag{3.7}$$

$$\hat{V}^{\text{el-el}} = \sum_{i=1}^{N_e}\sum_{j>i}^{N_e} \frac{1}{|r_i - r_j|} \tag{3.8}$$

$$\hat{V}^{\text{nucl-el}} = -\sum_{i=1}^{N_e}\sum_{j=1}^{N_n} \frac{Z_j}{|r_i - R_j|} \tag{3.9}$$

$$\hat{V}^{\text{nucl-nucl}} = \sum_{i=1}^{N_n}\sum_{j>i}^{N_n} \frac{Z_i Z_j}{|R_i - R_j|} \tag{3.10}$$

with the number of electrons N_e, the number of nuclei N_n, the atomic mass M_i and the atomic number Z_i. Atomic units are used. The position of the nuclei can further be considered as fixed with respect to the motion of the electrons, allowing to simplify the Hamiltonian as

$$\left[H^{\text{el}}_{\{R_j\}}\right] \Phi_i\left(\{R_j\}\right) = E_i^{\text{BO}} \Phi_i\left(\{R_j\}\right) \tag{3.11}$$

where the second term contains only the terms which are electron-dependent:

$$H^{\text{el}}_{\{R_j\}} = \hat{T}^{\text{el}} + \hat{V}^{\text{el-el}} + \hat{V}^{\text{nucl-el}} \tag{3.12}$$

and where the electrostatic interactions between nuclei is considered constant.

Eq. (3.11) thus clearly decouples the electronic contributions from the ones from the nuclei. Nevertheless, complicated correlations between electrons are still present, and may, depending on the required accuracy, imply more or less complicated calculations. Within this Thesis, a relatively simple approach is taken where these electron-electron interactions are averaged out by setting up an effective potential using the electronic density. This approach is formally known as the DFT approach developped in the following Section.

3.1.2 Hohenberg-Kohn Theorems

The problem of fully interacting electrons can be further simplified thanks to the work of Hohenberg and Kohn [90] . In their work, the fundamental variable is the electronic density $n(r)$ which reduces the electron subspace containing N electrons by a factor N (for instance, a wavefunction $3N$ dimensions to a density in 3 dimensions). Two important theorems give mathematical foundation to this simplification.

Theorem 1. *The ground-state electronic density $n(r)$ of a system of interacting electrons uniquely determines the external potential $V_{ext}(r)$ in which the electrons evolve.*

Similarly, V_{ext} is thus an universal functional of $n(r)$ within some additive constant. Because of this, any property of the system is a functional of the ground state density $n_0(r)$. For instance, the total energy is obtained as

$$E\left[n(r)\right] = F\left[n(r)\right] + \int n(r)V_{ext}(r)dr \tag{3.13}$$

with $F\left[n(r)\right]$ an universal (unknown) functional of the density.

Before discussing the Kohn-Sham Equations which will give the approach used in DFT for this unknown functional, the second theorem by Hohenberg and Kohn is given. This theorem is also used in these equations.

Theorem 2. *The universal functional for the energy $E\left[n(r)\right]$ is defined in terms of the electronic density n(r). The ground-state is obtained for the density $n_0(r)$ that minimizes this functional.*

Consequently, the ground-state of the system (as well as the total energy) can be obtained using conjugate gradient methods or other iterative minimization procedures [91].

3.1.3 Kohn-Sham Equations

To access the total energy of the system, an expression for $F\left[n(r)\right]$ is required. Kohn and Sham [92] proposed to split up this functional into

three terms defining the total energy in Eq. (3.13) as

$$E\left[n(r)\right] = T_s\left[n(r)\right] + E_H\left[n(r)\right] + E_{XC}\left[n(r)\right] + \int n(r)V_{ext}(r)dr \quad (3.14)$$

with the kinetic energy $T_s\left[n(r)\right]$ and the non-interacting electron gas $E_H\left[n(r)\right]$ given by

$$T_s\left[n(r)\right] = \frac{1}{2}\sum_{i=1}^{N}\int \psi_i^{\star}(r)\nabla^2\psi_i(r)dr \quad (3.15)$$

$$E_H\left[n(r)\right] = \frac{1}{2}\int n(r)V_H(r)dr = \frac{1}{2}\int \frac{n(r)n(r')}{|r-r'|}dr. \quad (3.16)$$

The third term, the exchange correlation energy, is most often not known exactly. The uncertainty on $F\left[n(r)\right]$ is thus completely governed by the approximations used to estimate $E_{XC}\left[n(r)\right]$.

Using the second HK theorem, and including the additional constraint to keep the total number of electrons N constant under variation of $n(r)$, the ground state is found using the Lagrangian multiplier λ:

$$\frac{\delta}{\delta n(r)}\left[E\left[n(r)\right] - \lambda\left(\int n(r)dr - N\right)\right] = 0 \quad (3.17)$$

or

$$\lambda = \frac{\delta E\left[n(r)\right]}{\delta n(r)} \quad (3.18)$$

$$= \frac{\delta T_s\left[n(r)\right]}{\delta n(r)} + V_{KS}(r) \quad (3.19)$$

with the Kohn-Sham potential being an effective potential given by

$$V_{KS}(r) = V_{\text{ext}} + V_H(r) + V_{XC}(r), \quad (3.20)$$

with V_{ext} the potential created by the ions, V_H the potential obtained from the one-electron Schrödinger wavefunctions

$$V_H(r) = \int \frac{n(r')}{|r'-r|}dr' \quad (3.21)$$

and the exchange correlation potential. The latter is derived from the yet unknown correlation energy as

$$V_{XC}(r) = \frac{\delta E_{XC}\left[n(r)\right]}{\delta n(r)}. \tag{3.22}$$

The electronic density is obtained from the single-particle wavefunctions:

$$n(r) = \sum_j \psi_j^\star(r)\psi_j(r) \tag{3.23}$$

which are obtained from

$$\left(-\frac{1}{2}\nabla^2 + V_{\mathrm{KS}}(r)\right)\psi_j(r) = \epsilon_j\psi_j(r) \tag{3.24}$$

Using Eq. (3.23) for the electron density, Eq. (3.20) for the Kohn-Sham potential and Eq. (3.24) for the single particle wave functions, a self consistent cycle can be established. At each cycle, the ground state wavefunction and electronic density are used.

The self-consistent cycle is depicted in Fig 3.1.

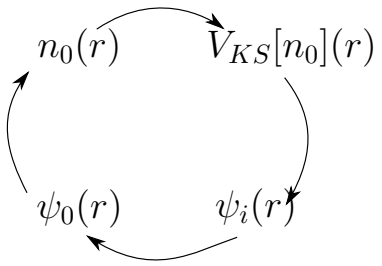

Figure 3.1: Self-Consistent Field cycle within DFT

The only unknown quantity remaining is the exchange correlation functional. The Local Density and Generalized Gradient Approximations (LDA and GGA) which were used in this Thesis are very briefly presented.

3.1.4 Exchange Correlation Functionals

LDA

In this local approximation, the exchange energy, which is required to find the exchange potential following Eq. (3.22), is obtained from the exchange-correlation energy density $\epsilon_{XC}^{\mathrm{HEG}}$ induced by an homogeneous electron gas. These values are known for any constant densities $n(r) = n$ from Quantum Monte-Carlo simulations [93] and have been parametrized [94].

GGA and More Elaborate Schemes

The GGA approach is very similar to the LDA one, except that a local gradient expansion of the density is used to evaluate this latter quantity [95]. More elaborate schemes involving semi-local or orbital dependent terms exist as well [96]. However, such precision is not required in this Thesis, and these approximations are thus not discussed here.

3.2 Kubo: Longitudinal Conductivity

A brief and general presentation of the Kubo-Greenwood method to calculate the longitudinal conductivity and related physical quantities is given in Section 3.2.1. In Section 3.2.2 some useful numerical techniques are presented to allow for efficient computation of aformentioned quantities.

3.2.1 Physical Quantities

Transport properties for large mesoscopic-sized systems can be simulated efficiently using an order-N method based on the Kubo formalism [97, 98, 99, 100, 101, 102, 103, 104]. In this formalism, the evolution of wave-packets through the sample is followed, which is altered from its behavior in pristine graphene by the presence of impurity potentials. Assuming the electronic transport in the system is isotropic for the in

plane x and y directions, the 2D diffusion coefficient $D(t)$ is obtained by

$$D(t) = D_x(t) + D_y(t) = 2D_x(t) \tag{3.25}$$

Within this formalism, the diffusion coefficient $D_x(t)$ in the transport direction x is calculated at each time step using

$$D_x(t) = \frac{\Delta X^2(t)}{t} \tag{3.26}$$

with the mean-quadratic displacement or spreading of a wave-packet given by

$$\Delta X^2(E,t) = \frac{\mathrm{Tr}\left[\delta(E-\hat{H})\left|\hat{X}(t)-\hat{X}(0)\right|^2\right]}{\mathrm{Tr}\left[\delta(E-\hat{H})\right]} \tag{3.27}$$

$$= \frac{\mathrm{Tr}\left[\left[\hat{X},\hat{U}(t)\right]^\dagger \delta(E-\hat{H})\left[\hat{X},\hat{U}(t)\right]\right]}{\mathrm{Tr}\left[\delta(E-\hat{H})\right]} \tag{3.28}$$

where $\hat{X}(t)$ is the position operator in Heisenberg representation at time t:

$$\hat{X}(t) = \hat{U}^\dagger(t)\hat{X}(0)\hat{U}(t) \tag{3.29}$$

and where $\hat{U}(t) = e^{-i\hat{H}t/\hbar}$ is the time-evolution operator.

An efficient computational scheme to calculate both the denominator and the numerator in Eq. (3.28) is outlined in Section 3.2.2. The denominator actually corresponds to the density of states (DOS) which is the sum of all states at an energy E:

$$\rho(E) = \sum_n \delta(E-E_n) = \mathrm{Tr}\left[\delta(E-\hat{H})\right] \tag{3.30}$$

where E_n are the eigenvalues stemming from the Hamiltonian $\hat{H}$ of the problem under consideration. The trace, which is a sum over each orbital of the system basis set, is replaced by an initial state with a random phase on each orbital of the system. Taking the average of ten initial random phase states already yields very satisfactory results. This greatly

reduces computation time. $U(t)$ can be expanded using Chebyshev polynomials (see Section 3.2.2) to allow for the mandatory order-N method to achieve reasonable computation time for systems containing millions of orbitals.

From the diffusion coefficient, the mean free path $\ell_e(E)$ and the semi-classical conductivity $\sigma_{\mathrm{sc}}(E)$ can be calculated using respectively:

$$\ell_e(E) = \frac{D^{\max}(E)}{2v(E)} \tag{3.31}$$

and

$$\sigma_{sc}(E) = \frac{1}{4}e^2\rho(E)D^{\max}(E) \tag{3.32}$$

where $v(E)$ is the charge carrier velocity at energy E, $D^{\max}$ the maximum value of $D(t)$ and e the electronic charge.

3.2.2 Numerical Techniques

Lanczos Recursion Technique

To calculate Eq. (3.28), the Lanczos recursion method is used. The core idea of this method is to transform the TB Hamiltonian $\hat{H}$ which can contain millions of elements (associated with each of the orbitals of the atoms) into a smaller tridiagonal matrix $\tilde{\hat{H}}$ [105]. This approximate representation of the original Hamiltonian is built on an orthogonal (Lanczos) basis [106]. In such basis, the operator $\delta(E - H)$ can be obtained in a computationally efficient way avoiding exact diagonalization of the original Hamiltonian.

The lanczos recursion tecnique was initially developed to obtain the eigenstates of the system [107], while here interest is only oriented towards the calculation of the DOS. The recursive approach proceeds as

follows:

$$a_1 = \left\langle \psi_1 \middle| \hat{H} \middle| \psi_1 \right\rangle \tag{3.33}$$

$$\left| \tilde{\psi}_2 \right\rangle = \hat{H} \left| \psi_1 \right\rangle - a_1 \left| \psi_1 \right\rangle \tag{3.34}$$

$$b_1 = \left\| \left| \tilde{\psi}_2 \right\rangle \right\| = \sqrt{\left\langle \tilde{\psi}_2 \middle| \tilde{\psi}_2 \right\rangle} \tag{3.35}$$

$$\left| \psi_2 \right\rangle = \frac{1}{b_1} \left| \tilde{\psi}_2 \right\rangle \tag{3.36}$$

for the first steps, while for consecutive steps:

$$a_n = \left\langle \psi_n \middle| \hat{H} \middle| \psi_n \right\rangle \tag{3.37}$$

$$\left| \tilde{\psi}_{n+1} \right\rangle = \hat{H} \left| \psi_n \right\rangle - a_n \left| \psi_n \right\rangle - b_{n-1} \left| \psi_{n-1} \right\rangle \tag{3.38}$$

$$b_n = \left\| \left| \tilde{\psi}_{n+1} \right\rangle \right\| = \sqrt{\left\langle \tilde{\psi}_{n+1} \middle| \tilde{\psi}_{n+1} \right\rangle} \tag{3.39}$$

$$\left| \psi_{n+1} \right\rangle = \frac{1}{b_n} \left| \tilde{\psi}_{n+1} \right\rangle \tag{3.40}$$

where a_n and b_n define the diagonal and off-diagonal elements of $\tilde{\hat{H}}$:

$$\tilde{\hat{H}} = \begin{pmatrix} a_1 & b_1 & 0 & 0 & \cdots & 0 \\ b_1 & a_2 & b_2 & 0 & \cdots & 0 \\ 0 & b_2 & a_3 & b_2 & \cdots & 0 \\ \cdots & \cdots & \cdots & \cdots & \cdots & \cdots \\ 0 & 0 & 0 & \cdots & b_{n-1} & a_n \end{pmatrix}. \tag{3.41}$$

To calculate the denominator in Eq. (3.28), rewrite the DOS based on the $\tilde{\hat{H}}$ as:

$$\left\langle \psi_1 \middle| \delta(E - \tilde{\hat{H}}) \middle| \psi_1 \right\rangle = \lim_{\eta \to 0} -\frac{1}{\pi} \mathrm{Im} \left(\left\langle \psi_1 \middle| \frac{1}{E + i\eta - \tilde{\hat{H}}} \middle| \psi_1 \right\rangle \right) \tag{3.42}$$

$$= \lim_{\eta \to 0} -\frac{1}{\pi} \mathrm{Im} \left(\kappa_1 \right) \tag{3.43}$$

where κ_1 is calculated using a continued fraction:

$$\kappa_1 = \cfrac{1}{E + i\eta - a_1 + \cfrac{b_1^2}{\cdots \cfrac{\ddots}{E + i\eta + a_{N-1} - \cfrac{b_{N-1}^2}{E + i\eta - a_N - b_N^2 \times \text{Term}}}}} \tag{3.44}$$

Different methods exist to terminate the continued fraction. In this Thesis, *Term* in the above expression is set to one, with the number of recursion steps n in a_n and b_n chosen large enough to attenuate as much as possible the oscillations in these recursion coefficients. A remnant oscillation is present when the physical system contains a bandgap, but results were not sensibly affected by this crude termination technique in comparison with more advanced termination methods.

Time Evolution

The time-evolution operator in Eq. (3.29) is expanded using Chebyshev polynomials:

$$\hat{U}(t) = e^{\frac{-i\hat{H}t}{\hbar}} = \sum_{n=0}^{\infty} c_n(t) Q_n(\hat{H}) \tag{3.45}$$

Q_n are modified Chebychev polynomials which act on the complete energy spectrum unlike the conventional polynomials which are limited to $[-1:1]$.

In Eq. (3.28), the evolution operator is contained in the commutator. The latter is rewritten as

$$\left[\hat{X}, \hat{U}(t)\right] \simeq \sum_{n=0}^{N} c_n(t) \left[\hat{X}, Q_n(\hat{H})\right]. \tag{3.46}$$

where Q_n is calculated recursively from Q_{n-1} and Q_{n-2}.

Detailed analysis of this technique is given in Ref. [108].

3.3 Kubo: Transverse Conductivity

In this Section, a novel approach to calculate the off-diagonal terms to the conductivity tensor is developed. Up to now, the present implementation of the Kubo Greenwood formalism only allowed to calculate efficiently the diagonal terms, which only gives acces to the longitudinal conductivity. In order to make meaningful predictions regarding the Quantum Hall effect, the off-diagonal terms have to be calculated in a computationally efficient way to be able to relate to experimentally meaningful samples.

The formalism is initially developed based on the Mahan definition of the perturbation to the ground-state Hamiltonian [109]. Consequenly, correspondance is given with the Kubo expression. Further development is achieved on the Kubo expression where the perturbation is defined by only one frequency.

The method adopted to include the magnetic field in the calculations is given in Appendix H.

3.3.1 Formalism

A quantum mechanical system without applied electric field can be described using the Hamiltonian H_0 and the density matrix

$$\rho_0 = e^{-\beta(H_0-\mu N-\Omega)}. \tag{3.47}$$

$\beta = \frac{1}{k_B T}$ is the inverse thermal energy, μ is the chemical potential, N is the number of particles and Ω is the grand potential. Such statistical approach using density matrices is often used for systems where the exact microscopical state is unknown. The conductivity is obtained as the linear response to an external electric field. Accordingly, the Hamiltonian H_0 includes all interactions but the electric field, which is treated as a perturbation to H_0. The complete Hamiltonian and density matrix are thus written as

$$H(t) = H_0 + H'(t) \tag{3.48}$$

$$\rho(t) = \rho_0 + f(t) \tag{3.49}$$

To obtain the conductivity induced by this perturbation, the macroscopic current has to be evaluated. Based on the approach using the density matrix, the macroscopic current is calculated with the current operator (derivation in Appendix C)

$$j_x = \frac{i}{\hbar}\left[H_0, P_x\right] \tag{3.50}$$

using the polarization operator

$$P_x = e_0 \sum_i R_{ix} a_i^\dagger a_i \tag{3.51}$$

with R_{ix} giving the positions of atom i in the x direction and e_0 the electronic charge. This definition of P_x is a sum over all sites of the system and thus yields a volume dependent current. This explains the volume renormalization in Eq. (3.53). A simple analysis based on the units proves that the current density in one direction now has the correct units: $\left[\frac{j}{V}\right] = \left[\frac{[H_0,P]}{\hbar V}\right] = \frac{AsmJ}{Jsm^2} = \frac{A}{m}$. This expression for the current operator is convenient for use in TB models. To calculate the conductivity at zero wave vector q, only the current operator at $q = 0$ is needed. Hence, the macroscopic current without electric field is expected to be zero and is given by

$$J_x^0 = \mathrm{Tr}[\rho_0 j_x] = 0. \tag{3.52}$$

Switching on the electric field, and using Eq. (3.49), the current-density response can be calculated using

$$\frac{J_x(t)}{V} = \frac{1}{V}\mathrm{Tr}[\rho(t) j_x] = \frac{1}{V}\mathrm{Tr}[f(t) j_x]. \tag{3.53}$$

Thus an expression for $f(t)$ is required.

Similarly to H, ρ follows the Heisenberg equation of motion

$$i\hbar \frac{d}{dt}\rho(t) = \left[H_0 + H'(t), \rho(t)\right]. \tag{3.54}$$

In the linear response theory, perturbations are considered small, and so

$$i\hbar\frac{d}{dt}f(t) = [H_0, f(t)] + \left[H'(t), \rho_0\right] \tag{3.55}$$

because $[H_0, \rho_0]$ equals zero (by definition) and second order perturbations $[H'(t), f(t)]$ are neglected. Solving this differential equation, $f(t)$ is given by

$$f(t) = f(-\infty) - \frac{i}{\hbar}e^{-itH_0/\hbar}\left[\int_{-\infty}^{t} dt' \left[H'_h(t'), \rho_0\right]\right] e^{itH_0/\hbar} \tag{3.56}$$

where

$$H'_h(t') = e^{it'H_0/\hbar}H'(t')e^{-it'H_0/\hbar}. \tag{3.57}$$

The Heisenberg picture was used to move the time dependence from the state vectors into the operators. This picture allows to get rid of the time dependence in the vectors and is often recurred to when doing time integrations. Initial conditions are defined by stating that for $t = -\infty$ there is no signal. This implies that ρ_0 and $\rho(t)$ should coincide and consequently that $f(-\infty) = 0$. Replacing $f(t)$ in Eq. (3.53) gives

$$\frac{J_x(t)}{V} = \frac{1}{V}\mathrm{Tr}\left[-\frac{i}{\hbar}e^{-itH_0/\hbar}\left[\int_{-\infty}^{t} dt' \left[H'_h(t'), \rho_0\right]\right] e^{itH_0/\hbar}j_x\right] \tag{3.58}$$

or, by introducing the time dependence into the current operator using

$$j_x(t) = e^{itH_0/\hbar}j_x e^{-itH_0/\hbar}, \tag{3.59}$$

Eq. (3.58) is given by

$$\frac{J_x(t)}{V} = -\frac{i}{V\hbar}\mathrm{Tr}\left[\int_{-\infty}^{t} dt' \left[H'_h(t'), \rho_0\right] j_x(t)\right] \tag{3.60}$$

because the trace is invariant under cyclic operations. To calculate an expression for the commutator in above equation, the definition for the perturbation introduced by Mahan is used, *i.e.* $H'(t') = \frac{i}{\omega}e^{-i\omega t'}j_y F_y = K(\omega, t')j_y F_y$ with the frequency ω. The commutator in Schrödinger

representation equals

$$\left[H'(t'),\rho_0\right] = \left[K(\omega,t')j_yF_y,\rho_0\right] = K(\omega,t')F_y\left[j_y,\rho_0\right] \tag{3.61}$$

and in Heisenberg representation by

$$\left[H'_h(t'),\rho_0\right] = K(\omega,t')F_y\left[j_y,\rho_0\right]. \tag{3.62}$$

The commutator in Eq. (3.62) is calculated doing some algebra:

$$\begin{aligned}\left[j_y(t'),\rho_0\right] &= \left[j_y(t'),e^{-\beta L}\right]\\ &= e^{-\beta L}\int_0^\beta d\lambda e^{\lambda L}\left[L,j_y(t')\right]e^{-\lambda L}\\ &= e^{-\beta(H_0-\mu N)}\int_0^\beta d\lambda e^{\lambda H_0}\left[H_0,j_y(t')\right]e^{-\lambda H_0}\\ &= \rho_0\left[H_0,\int_0^\beta d\lambda j_y(t'-i\hbar\lambda)\right]\end{aligned} \tag{3.63}$$

On the first line, Eq. (3.47) and the relation $L = H_0 - \mu N - \Omega$ are used. On the second line, the general relation $\left[A,e^{-\beta L}\right] = e^{-\beta L}\int_0^\beta d\lambda e^{\lambda L}\left[L,A\right]e^{-\lambda L}$ is exploited. The third line is explained because N commutes with both H_0 and $j_y(t)$ (which depends on P_y and consequently on $N_i = a_i^\dagger a_i$, with $[N,N_i] = 0$). For the last line, the integral is moved inside the commutator and an imaginary time shift

$$j_y(t'-i\hbar\lambda) = e^{-i(i\hbar\lambda)H_0/\hbar}j_y(t')e^{i(i\hbar\lambda)H_0/\hbar} = e^{\lambda H_0}j_y(t')e^{-\lambda H_0} \tag{3.64}$$

is applied (which is possible because H_0 and $e^{-\lambda H_0}$ commute). Eq. (3.62) can thus be rewritten as

$$\left[H'_h(t'),\rho_0\right] = \rho_0 K(\omega,t')F_y\left[H_0,\int_0^\beta d\lambda j_y(t'-i\hbar\lambda)\right] \tag{3.65}$$

and Eq. (3.60) as

$$\frac{J_x(t)}{V} = -\frac{i}{V\hbar}\mathrm{Tr}\left[\int_{-\infty}^t dt'\rho_0\left[H_0,\int_0^\beta d\lambda j_y(t'-i\hbar\lambda)\right]j_x(t)\right]K(\omega,t')F_y. \tag{3.66}$$

By shifting the time integration variable ($t' \to t' + t$) and taking into account that

$$\mathrm{Tr}\left[e^{-itH_0/\hbar}\hat{O}_h(t)e^{itH_0/\hbar}\right] = \mathrm{Tr}\left[\hat{O}_h(t)\right], \tag{3.67}$$

Eq. (3.66) becomes

$$\frac{J_x(t)}{V} = -\frac{i}{V\hbar}\mathrm{Tr}\left[\int_{-\infty}^{0} dt'\rho_0\left[H_0, \int_0^\beta d\lambda j_y(t' - i\hbar\lambda)\right] j_x\right] K(\omega, t' + t)F_y \tag{3.68}$$

where t' is the time difference between perturbation and response. Because the trace only depends on time differences, a final expression for the resulting current reads as

$$\frac{J_x(t)}{V} = -\frac{i}{V\hbar}\int_0^\infty dt' \int_0^\beta d\lambda \mathrm{Tr}\left[\rho_0\left[H_0, j_y\right] j_x(t' + i\hbar\lambda\right] K(\omega, t - t')F_y \tag{3.69}$$

by setting $t' \to -t'$. Consequently, using

$$j_x = \sigma_{\mathrm{xy}}E_y, \tag{3.70}$$

the conductivity response is given by

$$\sigma_{\mathrm{xy}}(\omega) = \frac{1}{V\hbar\omega}\int_0^\infty dt e^{i\omega t}\int_0^\beta d\lambda \mathrm{Tr}\left[\rho_0\left[H_0, j_y\right] j_x(t + i\hbar\lambda)\right]. \tag{3.71}$$

This can also be rewritten using Kubo's definition of the first order perturbation, $H'(t) = -x_y e_0 e^{-i\omega t}F_y$, as:

$$\sigma_{\mathrm{xy}}(\omega = 0) = \frac{1}{V}\int_0^\infty dt \int_0^\beta d\lambda \mathrm{Tr}\left[\rho_0 j_y j_x(t + i\hbar\lambda)\right]. \tag{3.72}$$

The correspondance between Eq. (3.71) and Eq. (3.72) is straightforward if perturbations $H'(t)$ are considered equal (to yield the same physics). Based on this assumption,

$$[H_0, j_y] = \hbar\omega j_y, \tag{3.73}$$

which implies that the current operator is of the form $j_y(t) = Ae^{i\omega t}$ depending on only one frequency.

Translating Eq. (3.72) into a many particle basis and using Eq. (3.64) yields:

$$\sigma_{\text{xy}} = \frac{1}{V}\int_0^\infty dt \int_0^\beta d\lambda \sum_n \left\langle n\middle|\rho_0 j_y e^{-\lambda H_0} j_x(t) e^{\lambda H_0}\middle|n\right\rangle . \tag{3.74}$$

The last exponential in this expression is applied to state $|n\rangle$, giving thus that

$$\sigma_{\text{xy}} = \frac{1}{V}\int_0^\infty dt \int_0^\beta d\lambda \sum_n \left\langle n\middle|\rho_0 j_y e^{-\lambda(H_0 - E_n)} j_x(t)\middle|n\right\rangle . \tag{3.75}$$

Introducing a second many particle basis through the $\sum_m |m\rangle\langle m|$ identity allows to transform the Hamiltonian dependent part into a scalar to allow for future integration with respect to λ. Doing this and casting ρ_0 on the $|n\rangle$ state, it follows that

$$\begin{aligned}
\sigma_{\text{xy}} &= \frac{1}{V}\int_0^\infty dt \int_0^\beta d\lambda \sum_{m,n} \left\langle n\middle|\rho_0 j_y\middle|m\right\rangle \left\langle m\middle|e^{-\lambda(E_m - E_n)} j_x(t)\middle|n\right\rangle \\
&= -\frac{1}{V}\int_0^\infty dt \sum_{m,n} e^{-\beta E_n} \left\langle n\middle|e^{-\beta(-\mu N - \Omega)} j_y\middle|m\right\rangle \left\langle m\middle|j_x(t)\middle|n\right\rangle \left(\frac{e^{-\beta(E_m - E_n)} - 1}{E_m - E_n}\right) \\
&= -\frac{1}{V}\int_0^\infty dt e^{-\beta(-\mu N - \Omega)} \sum_{m,n} \langle n|j_y|m\rangle\langle m|j_x(t)|n\rangle \left(\frac{e^{-\beta E_m} - e^{-\beta E_n}}{E_m - E_n}\right).
\end{aligned} \tag{3.76}$$

Because the first term from the fraction is the complex conjugate of the second term and using $A + A^\dagger = 2\text{Re}[A]$, and by removing the time dependence from the current operator, the many body expression of the conductivity is given by

$$\begin{aligned}
\sigma_{\text{xy}} &= -\frac{2}{V}\int_0^\infty dt \\
&\lim_{\eta\to 0^+} \sum_{m,n} \text{Re}\left[\langle n|j_y|m\rangle \langle m|j_x|n\rangle \frac{e^{it(E_m - E_n)/\hbar} e^{-\beta(E_n - \mu N - \Omega)}}{E_n - E_m + i\eta}\right].
\end{aligned} \tag{3.77}$$

An infinitesimal imaginary term is added in the denominator to avoid pole divergence.

For the actual implementation, it is more convenient to express σ_{xy} in a single particle basis. This is achieved in the following lines.

Using creation and annihilation operators, the current operator can be written as:

$$j_x = \sum_{k_1,k_2} j_{xk_1k_2} a^\dagger_{k_1} a_{k_2} \tag{3.78}$$

where k_i are single particle energy eigenstates. Substituting this expression in Eq. (3.77), an expression containing

$$\begin{aligned}\left\langle n\middle|a^\dagger_{k_1}a_{k_2}\middle|m\right\rangle \left\langle m\middle|a^\dagger_{k_3}a_{k_4}\middle|n\right\rangle = \\ \delta_{k_1k_4}\delta_{k_2k_3}\left\langle n\middle|a^\dagger_{k_1}a_{k_2}\middle|m\right\rangle \left\langle m\middle|a^\dagger_{k_2}a_{k_1}\middle|n\right\rangle \\ + (1-\delta_{k_1k_4})\delta_{k_1k_2}\delta_{k_3k_4}\left\langle n\middle|a^\dagger_{k_1}a_{k_1}\middle|m\right\rangle \left\langle m\middle|a^\dagger_{k_3}a_{k_3}\middle|n\right\rangle\end{aligned} \tag{3.79}$$

is obtained by differentiation between $k_1 = k_4$ (first term) and $k_1 \neq k_4$ (second term). For the first term, non-zero terms require $k_2 = k_3$. For the second one, $k_1 = k_2$ and $k_3 = k_4$, otherwise $|n\rangle$ cannot be equal to $|m\rangle$. Annihilating a particle with eigenstate k_1 and creating a particle with same eigenstate k_1 implies that $|n\rangle = |m\rangle$. In that case, only imaginary terms are left in Eq. (3.77) and thus vanish taking the real part. Keeping only the first term of Eq. (3.79), Eq. (3.77) is written as:

$$\begin{aligned}\sigma_{\mathrm{xy}} = -\frac{2}{V}\int_0^\infty dt \lim_{\eta\to 0^+} \mathrm{Re}\left[\sum_{k_1,k_2}\sum_{m,n} j_{yk_1k_2}j_{xk_2k_1}\right. \\ \left.\left|\left\langle n\middle|a^\dagger_{k_1}a_{k_2}\middle|m\right\rangle\right|^2 \frac{e^{it(E_m-E_n)/\hbar}e^{-\beta(E_n-\mu N-\Omega)}}{E_n-E_m+i\eta}\right]\end{aligned} \tag{3.80}$$

Considering non-interacting particles, for which the total energy of the state $|m\rangle$ is a sum of single particle states $|k\rangle$, weighted with the corresponding occupation numbers is given by

$$E_m = \sum_k \epsilon_k n^m_k, \tag{3.81}$$

Because the energies for the single particle subspaces of the states $|m\rangle$ and $|n\rangle$ only differ for k_1 and k_2, the weighted sum reduces to these two values for the energy difference term in Eq. (3.80) and can thus be expressed as

$$\sigma_{\mathrm{xy}} = -\frac{2}{V}\int_0^\infty dt \lim_{\eta\to 0^+} \mathrm{Re}\left[\sum_{k_1,k_2}\sum_{m,n} j_{yk_1k_2} j_{xk_2k_1} \left|\left\langle n\middle|a_{k_1}^\dagger a_{k_2}\middle|m\right\rangle\right|^2 \frac{e^{it(\epsilon_{k_2}-\epsilon_{k_1})/\hbar} e^{-\beta\left[\sum_p(\epsilon_p-\mu)n_p^m-\Omega\right]}}{\epsilon_{k_1}-\epsilon_{k_2}+i\eta}\right]. \quad (3.82)$$

$\langle n| a_{k_1}^\dagger$ counts the number of electrons in single particle state k_1 for the many wave function $\langle n|$ (similar interpretation for $a_{k_2}|m\rangle$) Because for each $|n\rangle$, there can only be one $|m\rangle$ for which the prefactor does not vanish, the sum on n can be removed. The term in the second sum on m can be replaced by $n_{k_1}^m$, which is either 0 or 1 which allows to remove the absolute square and introduce the Fermi-Dirac distribution for the state k_1 defined as

$$f(\epsilon_k-\mu) = \sum_m n_{k_1}^m e^{-\beta\left[\sum_p(\epsilon_p-\mu)n_p^m-\Omega\right]} \quad (3.83)$$

into Eq. (3.82) which yields

$$\sigma_{\mathrm{xy}} = -\frac{2}{V}\int_0^\infty dt \lim_{\eta\to 0^+} \mathrm{Re}\left[\sum_{k_1,k_2} j_{yk_1k_2} j_{xk_2k_1} \frac{e^{it(\epsilon_{k_2}-\epsilon_{k_1})/\hbar}}{\epsilon_{k_1}-\epsilon_{k_2}+i\eta} f(\epsilon_{k_1}-\mu)\right]. \quad (3.84)$$

It follows that

$$\sigma_{\mathrm{xy}} = -\frac{2}{V}\int_0^\infty dt \lim_{\eta\to 0^+} \sum_k f(\epsilon_k-\mu)\mathrm{Re}\left[\left\langle k\middle| j_y \frac{1}{\epsilon_k - H_0 + i\eta} j_x(t)\middle|k\right\rangle\right] \quad (3.85)$$

Eventually, σ_{xy} in the many-body basis $|n\rangle$ [see Eq. (3.77)] has thus been reevaluated in the single particle basis $|k\rangle$. These single particle states $|k\rangle$ and the corresponding eigenstates ϵ_k are not exactly known. To solve this lack of information, $\int_{-\infty}^{\infty} dE\delta(E - H_0)$ is introduced to integrate over all states:

$$\sigma_{\mathrm{xy}} = -\frac{2}{V}\int_0^{\infty} dt \int_{-\infty}^{\infty} dE f(E-\mu) \lim_{\eta\to 0^+} \sum_k \mathrm{Re}\left[\left\langle k\middle|\delta(E-H_0) j_y \frac{1}{E-H_0+i\eta} j_x(t)\middle|k\right\rangle\right] \quad (3.86)$$

where only the states $E = \epsilon_k$ are not equal to zero. Similar to the approach for the longitudinal conductivity, the trace is replaced by an average over random-phase states $|\Psi_{RP}\rangle = \Psi_1$. This state is normalized to one using the number of sites N_s. The boundary of the time integral is replaced by t' (which tends to ∞ if infinite computation time is available). The *approximately resolved* identity

$$\sum_{j=1}^{N_{\mathrm{recurs}}} |\Psi_j\rangle\langle\Psi_j| \simeq 1 \quad (3.87)$$

is also introduced into Eq. (3.86) so that

$$\sigma_{\mathrm{xy}}(t') = \frac{2N_s}{V}\int_0^{t'} dt \int_{-\infty}^{\infty} dE f(E-\mu) \lim_{\eta\to 0^+} \sum_{j=1}^{N_{\mathrm{recurs}}} \mathrm{Re}\left[\left\langle \Psi_1\middle|\delta(E-H_0)\middle|\Psi_j\right\rangle\left\langle \Psi_j\middle| j_y \frac{1}{E-H_0+i\eta} j_x(t)\middle|\Psi_1\right\rangle\right]. \quad (3.88)$$

This identity allows the separate the complicated product into simpler terms which are efficiently computed using the Lanczos recursion techniques for tridiagonalized matrices, which are routinely used for the calculation of the longitudinal conductivity. By moving the time dependence out of the operator $j_x(t)$ using Eq. (3.59), the corresponding evolution operator $U(t) = e^{-itH_0/\hbar}$ can be applied on the right to $|\Psi_1\rangle$

and on the left to $\langle\Psi_j|j_y|$, and by using the fact that

$$\langle\Psi_1|\delta(E-H_0)|\Psi_j\rangle = -\frac{1}{\pi}\mathrm{Im}\left[\left\langle\Psi_j\middle|\frac{1}{z-H_0}\middle|\Psi_1\right\rangle\right] \equiv -\frac{1}{\pi}\mathrm{Im}[\kappa_j] \quad (3.89)$$

the final expression for numerical implementation of the transverse conductivity is found:

$$\sigma_{\mathrm{xy}}(t') = \frac{2}{\pi V_{\mathrm{at}}}\int_0^{t'} dt \int_{-\infty}^{\infty} dE f(E-\mu) F_{\mathrm{damp}}$$
$$\lim_{\eta\to 0^+}\sum_{j=1}^{N_{\mathrm{recurs}}} \mathrm{Im}[\kappa_j]\mathrm{Re}\left[\left\langle\Psi_j\middle|j_y U^\dagger(t)\frac{1}{E-H_0+i\eta}j_x U(t)\middle|\Psi_1\right\rangle\right] \quad (3.90)$$

where F_{damp} is an added artificial damping factor:

$$F_{\mathrm{damp}} = e^{-\epsilon_{\mathrm{damp}}t} \quad (3.91)$$

with ϵ_{damp} usually ranging from 0.01 for short computation times to smaller values for longer computation times. This damping factor allows to avoid the numerical necessity to go to infinite times to reach a steady state. On physical grounds, this is reasonable also, because experimental contact physics may generate damping as well.

3.3.2 Numerical Implementation

Proceeding with Eq. (3.90), a computationnaly efficient approach needs to be used to maximally benefit from the available resources and reach reasonable computation times. The difficulty compared to the calculation of σ_{xx} lies in the fact that the wave vectors Ψ_j need to be evolved and stored for each value of j. Formerly, these vector elements were calculated as well, but were only needed to calculate the DOS. Storing these wavevectors is straightforward using a highly parallelized infrastructure where each Ψ_j is stored on one processor and used independently to calculate the time dependent part of Eq. (3.90). Once each term of the time dependent part is calculated, it has to be multiplied with the time independent part $\mathrm{Im}[\kappa_j]$ and reduced on the master node of the parallelized infrastructure. These reduced sums [*i.e.* the second

line of Eq. (3.90)] are written at each time step to be used later for post-processing where the two integrations on the first line are performed. Doing so allows to test different damping factors depending on required temperature convergence.

Time-independent term

The independent part $\mathrm{Im}[\kappa_j]$ is a generalized density routine where, instead of the first element of the inverse of $z - H_0$ (with $z = E + i\eta$), the whole column is computed. The continued fraction is expanded beyond the calculation of κ_1 [See Eq. (3.44)] as follows. The system

$$\sum_n (z - \tilde{\hat{H}})_{mn} \kappa_n = \delta_{m1}, \tag{3.92}$$

with $\tilde{\hat{H}}$ defined previously [Eq. (3.41)], is written explicitely as

$$\begin{aligned}
(z - \tilde{\hat{H}}_{11})\kappa_1 + \tilde{\hat{H}}_{12}\kappa_2 &= 1 \\
\tilde{\hat{H}}_{21}\kappa_1 + (z - \tilde{\hat{H}}_{22})\kappa_2 + \tilde{\hat{H}}_{23}\kappa_3 &= 0 \\
\cdots &= 0 \\
\tilde{\hat{H}}_{nn-1}\kappa_{n-1} + (z - \tilde{\hat{H}}_{nn})\kappa_n + \tilde{\hat{H}}_{nn+1}\kappa_{n+1} &= 0.
\end{aligned} \tag{3.93}$$

The usual continued fraction calculates κ_1, while the other terms are computed recursively with:

$$\begin{aligned}
\kappa_2 &= \frac{1 - (z - \tilde{\hat{H}}_{11})\kappa_1}{\tilde{\hat{H}}_{12}} \\
\kappa_3 &= \frac{-\tilde{\hat{H}}_{21}\kappa_1 - (z - \tilde{\hat{H}}_{22})\kappa_2}{\tilde{\hat{H}}_{23}} \\
\cdots &= \cdots \\
\kappa_{n+1} &= \frac{-\tilde{\hat{H}}_{nn-1}\kappa_{n-1} - (z - \tilde{\hat{H}}_{nn})\kappa_n}{\tilde{\hat{H}}_{nn+1}}
\end{aligned} \tag{3.94}$$

Only the imaginary part of these elements are required. This time-independent matrix inversion step thus scales linearly with the num-

ber of elements. The vector elements Ψ_j obtained by the continued fraction of κ_1 are distributed among each processor to be used in the time-dependent term. Accordingly, parallelization is maximal when the number of processors equals the number of recursion steps j.

Time-dependent term

The time-dependent step is a sequential run on each processor of the parallelized system. This step can be divided into (i) the evolution of both $|\Psi_1\rangle$ (which is done on the master node) and $j_y^\dagger |\Psi_j\rangle$ (which is performed on each node containing $|\Psi_j\rangle$) and (ii) the recursion of both evolved quantities from (i). Setting $j_y^\dagger |\Psi_j\rangle = |\beta\rangle$ (and $|\beta_1\rangle = U(t)|\beta\rangle$) and $|\alpha_1\rangle = j_x U(t)|\Psi_1\rangle$, the recursion in (ii) is calculated as

$$\begin{aligned}\mathrm{Re}\left[\left\langle\beta_1\middle|\frac{1}{z-H_0}\middle|\alpha_1\right\rangle\right] &= \sum_k \mathrm{Re}\left[\left\langle\beta_1\middle|\frac{1}{z-H_0}\middle|\beta_k\right\rangle\left\langle\beta_k\middle|\alpha_1\right\rangle\right] \\ &= \sum_k \mathrm{Re}\left[\lambda_k \langle\beta_k|\alpha_1\rangle\right]\end{aligned}$$

where the identity $\sum_k |\beta_k\rangle\langle\beta_k| = 1$ was introduced. The recursion of (ii) reduces to the recursion of the elements λ_k, similar to the recursion used in the time-independent part, except now the elements are fully complex. The recursion has to be calculated with respect to the index k starting from vector $|\beta_1\rangle$. The overlaps $\langle\beta_k|\alpha_1\rangle$ are calculated simultanuously during the recursion routine. Performing the multiplication and the sum over indices k, the results from these sequential runs on each node can finally be reduced to the master node.

Energy and time integration

Both the energy and time integration are kept for post-processing. The advantages are twofold. First, the damping factor is not known a priori and can thus be varied according to ones needs. This damping factor depends a lot on natural damping introduced by disorder and contact damping artificially introduced through this factor. If no disorder were present (which physically makes no sense when measuring the quantum Hall effect in two dimensional systems), damping would be solely de-

pending on the damping factor. Second, analyzing the evolution of the reduced sums from the second line of Eq. (3.90) with time allows to check if the time step chosen for the calculation is small enough to correctly probe the evolution of the wavepackets and large enough to allow for long computation times. Prefactors from Eq. (3.90) are also introduced during the post-processing phase.

Part II

Results

Introduction

In the following Chapters, different results obtained during this PhD thesis are discussed. The way to organize this Results Part is chosen to reflect the different kinds of disorder used to modify graphene's properties.

In Chapter 4, results obtained on an academic model of divacancies are presented. This academic model is a simplified version of the TB model used for epoxy impurities discussed in Chapter 5. The motivation of this study is closely related to a follow up paper [24] to the first paper in 2004 which proved the existence of 2-dimensional graphite. For the specific honeycomb structure of so-called graphene, a different Landau level spectrum was predicted compared to conventional 2DEGs (see Section 2.2 for more in depth discussion of their similarities and differences).

Ever since, the QHE effect has been at the center of more and more theoretical and experimental papers, trying to tailor the spectrum of localized and extended states. Until recently, focus was mostly oriented towards ultraclean graphene, which allows exotic physics to take place. Doing so, many authors have tried to lift either the valley or spin degeneracy of the four-fold degenerate LL0, which gives rise to a zero energy Hall plateau. Only recently, the specific role of disorder has seen an uprise of interest in the litterature.

The longitudinal conductivity (see Section 4.2) from our calculations hints towards the existence of critical QHE states which are related to impurity-pinned disorder states. This existence is confirmed by the transverse conductivity (see Section 4.3) where a zero energy Hall plateau forms, not related to the usual spin or valleyspin symmetry

breaking interpretation. The proposed origin for such *new* zero energy Hall plateau might be considered one of the most important results from this Thesis.

Chapter 5 focuses on the functionalization of graphene with oxygen atoms put in *bridge* (hereafter refered to as *epoxy*) position. This model is first used in an attempt to understand the transport behavior of graphene after ozone treatment. This treatment was achieved experimentally by the group of Professor Adrian Bachtold in Barcelona, where most of the experimental measurements were done by Dr. Joël Moser. Ozone molecules adsorb on the graphene basal plane with a binding energy of 0.25 eV, and the physisorbed molecules can chemically react with graphene to form epoxide groups and oxygen molecules [110]. These oxygen molecules can be removed by adequate treatment, to only keep the epoxy groups. This collaboration with the experimental group came in place to attempt to confirm the hunch they had about the presence of quantum localization effect in their samples. Such phenomenon is now widely accepted and attributed to the presence of short-range scatterers which allow counterpropagating charge carriers to occupy inequivalent valleys (see Section 2.1.2).

In Section 5.2, focus is driven towards the semi-classical and quantum transport behavior at zero magnetic field. In Section 5.3, attention is shifted towards the transport response of this functionalized graphene under finite magnetic fields. This Section extends the longitudinal conductivity results on the academic divacancy model from Chapter 4 to this more realistic disorder model, hinting towards some universality of the impurity related critical states. Finally, Section 5.4 briefly introduces Hall conductivity results on this model, whose interpretation appears to be less straightforward than the one for divacancies in Section 4.3.

In Chapter 6, the transport behavior of hydrogenated graphene is looked into. This study was motivated trying to elucidate some controversy regarding the existence of magnetism in graphene. The choice for hydrogen atoms is straightforward as it relies solely on the removal of one π-electron, which can induce a local magnetic moment (in opposition to already magnetic impurities, which would make the seperation

between intrinsic and extrinsic magnetism more complicated) and also by the fact that a random distribution of single hydrogen atoms can either preserve or break the sublattice symmetry.

More specifically, in Section 6.3, the magnetoresistive response of graphene is calculated in an attempt to give guidance to experimentalists to interpret possible coupling between local magnetic moments in graphene. In Section 6.4, sublattice dependent transport behavior is calculated and linked with the different magnetic ordering ground states for hydrogenated graphene.

Finally, Chapter 7 compares different kinds of disorder, including both the disorder models discussed in the two previous chapters as well as other disorder models, in order to gain a better global understanding of functionalized graphene. Such comprehensive picture trying to establish generalities is mandatory to help experimentalists and industry choose the right absorbants to tailor graphene's properties to their specific needs.

Chapter 4

Divacancies

4.1 Introduction

In this Chapter, results obtained on an academic model of so-called *divancancies* are analyzed. Real divancies in graphene are subject to reconstruction. This was avoided on purpose to capture only the physics responsible for some peculiar observations at LL0. The main purpose of this study is to get some understanding of the effect of sublattice symmetry-preserving disorder on the QHE in graphene. This simplified model will also help rationalizing results from the next Chapter on the more realistic epoxy oxygen model. The prediction of a new zero energy plateau in the Hall conductivity is confirmed with the new formalism calculating the off-diagonal conductivity terms (see Section 3.3 for details on methodology). The convergence studies on the different parameters of importance for the transverse conductivity are presented in Appendix E. Other convergence studies related to this formalism are presented in Appendix F, for the case of Anderson disorder.

4.2 Longitudinal Conductivity

4.2.1 Equivalent Model

The simple case of non-reconstructed divacancy defects in otherwise clean graphene, i.e. removed pairs of first-neighbor carbon atoms, is

considered. Such divacancies are described by removing the p_z orbitals of the missing carbon atoms from the Hamiltonian of pristine graphene. These defects are strictly related to the epoxy adsorbates from the next Chapter, because the presence of oxygen atoms leads to an energy shift of the corresponding bridged carbon atoms by $\epsilon = 1.5$ eV away from zero energy (not taking into account the modified hopping terms), thus mimicking a divacancy to a certain extent. Figure 4.1 allows for a closer examination of the respective TB models, where the value of the ϵ_0 shifts from a zero value in the pristine case, to a finite ϵ_1 value in the epoxy case and an infinite value ϵ_∞ in the case of the non-reconstructed divacancy. An infinite onsite energy has the same effect as completely removing this p_z orbital. The graphene sublattice symmetry is preserved in all cases, since the bridged/missing carbon atoms belong equally to both sublattices. The effect of the magnetic field is included in both cases by a Peierls phase (see Appendix H).

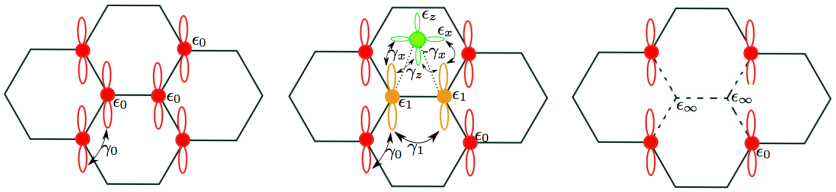

Figure 4.1: Tight-binding models for pristine graphene (left), epoxy defect (central) and divacancy (right). Carbon atoms and corresponding p_z orbitals are represented in red (orange for bridging carbon atoms), while the oxygen atom with its p_x and p_z orbital are colored in green.

The analogy between divacancy and epoxy disorder is only appropriate at low energies and does not capture some important aspects of the oxygen functionalization which induces electron-hole asymmetry. The divacancy disorder model gives rise to a new class of impurity related critical states, and allows to generalize similar results in the epoxy case to a larger class of adsorbates covalently grafted to the graphene surface.

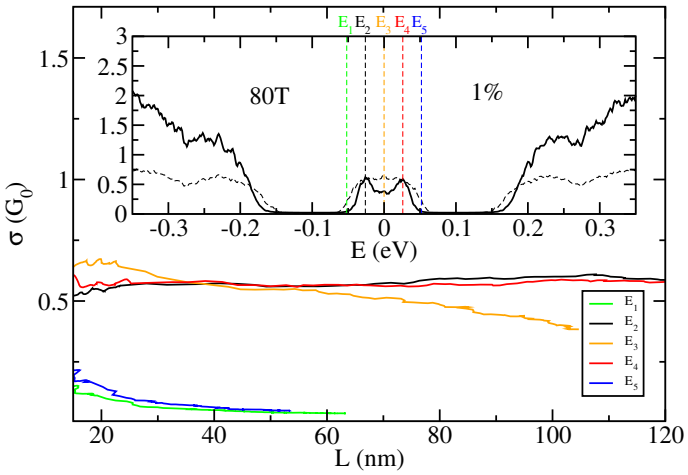

Figure 4.2: Main frame: length dependent conductivity for the divacancy at selected energies in the inset. Inset: conductivity at 80T and 1% of double vacancies (solid line) and superimposed rescaled DOS (dashed line).

4.2.2 Longitudinal Conductivity

Figure 4.2 illustrates the conductivity as a function of L for 1% of divacancies at 80T, at highest computation time, where the steady state is reached. The inset shows that, around $E = 0$ eV, the low-energy conductivity σ develops a double peak structure for σ, while the DOS exhibits a broad feature at $E = 0$ eV. The scaling analysis based on the length dependent conductivity in the main frame shows the extended nature of the states at the energies E_2 and E_4 and the progressively vanishing conductivity at $\sigma(E = 0)$. Localized states exhibit a decreasing conductivity with length, while extended states saturate without further decrease.

4.2.3 Spatial Extent of Low-Energy States

In this Section, the low-energy conductivity splitting for divacancies is further scrutinized by focusing on the spatial extend of the states at different energies. To this end, divacancies in a very large graphene sample (armchair ribbon) in the presence of high magnetic fields are

considered. By means of the Green's function approach [111], the total DOS and the LDOS are evaluated to gain microscopic insight into the electronics of states and their localization at divacancies under magnetic field. By excluding the regions close to the edges (with a large safety width of about 25 nm), edge states are excluded from the results, thus giving a bulk picture.

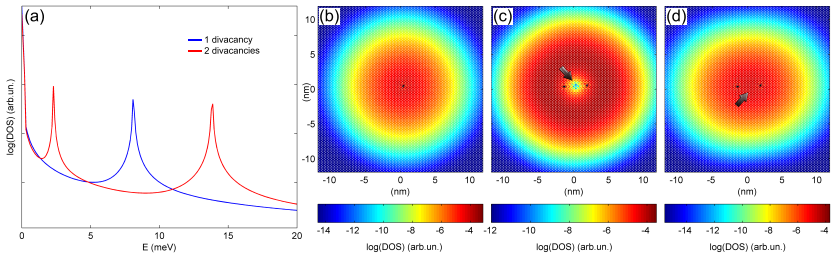

Figure 4.3: (a) DOS at $B = 80T$ in a region around the defects, in the presence of a single divacancy or two divacancies at a distance of 3.5 nm. (b) LDOS around the single divacancy corresponding to the peak at $E = 8.1$ meV. (c) LDOS around the two divacancies corresponding to the low-energy peak at $E = 2.3$ meV. (c) LDOS around the two divacancies corresponding to the high-energy peak at $E = 13.9$ meV. The divacancies are indicated by black points.

In a first step, a single divacancy at 80 T is considered. The DOS evaluated in a region around the defects clearly shows a peak at $E = 8.1$ meV, see Fig. 4.3(a). Because of the electron-hole symmetry for the divacancy, only positive energies are considered. The LDOS of the corresponding bound state is reported in Fig. 4.3(b) where the extension of the state is of the same order as the magnetic length ($l_B = 2.9$ nm). Moreover, the energy of the bound state increases with the magnetic field.

In order to investigate the coupling of defect induced states, in a second step, a pair of divacancies at a distance of about 3.5 nm is studied. Figure 4.3(a) shows that the single defect level splits into two new levels at $E = 2.3$ meV and $E = 13.9$ meV, which suggests that these two levels correspond to the symmetric and the antisymmetric combinations of the two single-defect states. This conjecture is confirmed by the LDOS reported in Figs. 4.3 (c) and (d). The low energy state corresponds to

the antisymmetric combination, characterized by a LDOS depletion in between the two divacancies, see the arrow in Fig. 4.3(c). On the other hand, the high-energy level corresponds to the symmetric combination, with a higher and more homogeneous LDOS in between the two defects, see the arrow in Fig. 4.3(d).

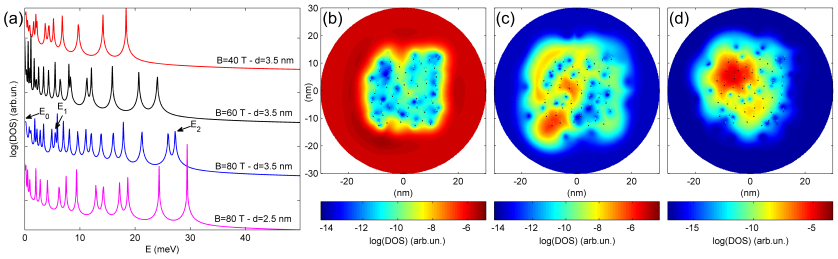

Figure 4.4: (a) DOS in a region around the defects, in the presence of a 50 divacancies at different distance and under different magnetic fields. Curves are shifted along the $y-$axis to avoid superposition. $d = 2.5$ nm (pink - 80T) and $d = 3.5$ nm (red - 40T, black - 60T and blue - 80T) correspond to about 0.5% and 0.3% of impurities respectively.(b) LDOS in a region around the divacancies at $E_0 \approx 0.1$ meV. (c) LDOS in a region around the divacancies at $E_1 \approx 5.5$ meV. (d) LDOS in a region around the divacancies at $E_2 \approx 27.2$ meV. The divacancies are indicated by black points.

In a third step, the presence of 50 divacancies is analyzed. These divacancies are randomly placed, with a minimum distance of 3 nm and a maximum distance $d = 3.5$ nm between adjacent divacancies. As expected, the number of DOS peaks (resulting from linear combinations of bound states) strongly increases and the states occur in a wider energy window, see the blue line in Fig. 4.4(a). At very low energy ($E_0 \approx 0.1$ meV), the standard Landau level (LL0) is found, whose states are located exclusively outside the divacancy region, that is the red region outside the divacancy island in Fig. 4.4(b), where they are quite homogeneously distributed. These states obviously do not penetrate inside the island region (blue, low LDOS). When defects are randomly distributed all over the sample , the LL0 states are confined in the regions with low defect density and cannot easily percolate through the defective sample. As a consequence the conductivity at $E = 0$ is strongly reduced.

At slightly higher energies [see arrows in Fig. 4.4(a)], rather localized states are found, as seen from the inhomogeneous LDOS in Fig. 4.4(c) for E_1=5.5 meV (the large number of blue spots correspond to low LDOS values). As a consequence, transport is strongly affected by scattering. With increasing energy, a clear tendency is observed that the states are more homogeneously distributed over the divacancies, or more precisely over groups of many close divacancies. For example, in Fig. 4.4(d), the LDOS corresponding to the state at $E_2 = 27.2$ meV spreads over a group of about 14 divacancies (red feature). To summarize, only the higher energy states (derived from linear combinations of impurity-pinned states) are extended and are expected to give large conductivity, while zero-energy states and low energy states are more localized. This mechanism fully clarifies the origin of the two conductivity peaks and the zero energy dip.

4.2.4 Scaling of Conductivity Splitting

The magnetic-field and concentration dependence of the DOS is illustrated in Fig 4.4(a). As for the case of a single divacancy, the peaks shift to higher energies when increasing the magnetic field When reducing the maximum spacing d to 2.5 nm, the close proximity between divacancies strengthens the coupling between the corresponding bound states and increases the energy splitting of the peaks.

4.3 Transverse Conductivity

In this Section, results confirming the prediction based on the longitudinal conductivity suggesting the appearence of a new zero energy plateau are presented. The correspondence between the σ_{xy} curves and the σ_{xx} curves is pictured. These results are some of the most crucial observations made during this Thesis. The numerical stability and convergence studies for the σ_{xy} curves are presented in Appendix E.

Figure 4.5 is the central part of this Section. Firstly, it validates the prediction on delocalized states carried by disorder from the σ_{xx} analysis. Indeed, the onset of change in σ_{xy} conductivity after the plateau

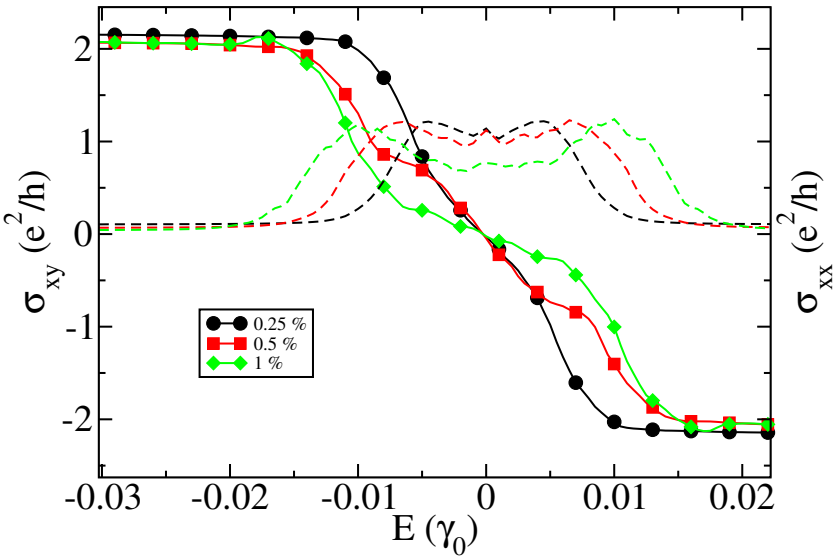

Figure 4.5: Superposition of σ_{xx} and σ_{xy} at 80 T. σ_{xx} is taken at $15400\frac{\hbar}{\gamma_0}$ and σ_{xy} at 1600 (0.25% and 0.5%) or $1575\frac{\hbar}{\gamma_0}$ (1%). Damping factors are equal to 0.001 for all concentrations.

of constant value, corresponds to the energies of the peaks of disorder related delocalized states in σ_{xx}. Secondly, it confirms the validity of the σ_{xy} implementation. And finally, it indicates the situation might be even more peculiar for weaker concentration.

For 1%, the situation is as anticipated. A zero energy Hall plateau develops between the delocalized states triggered by this specific disorder. For 0.5% of divacancies, the LL0 is partly recovered on top of the higher disorder situation, which leads to the partial disappearance of the new zero energy plateau leading to a three step behavior between $2\frac{e^2}{h}$ and $-2\frac{e^2}{h}$. This interpretation finds backup in the corresponding σ_{xx} calculation. Finally, for 0.25%, the energy splitting between delocalized states is probably too weak to properly develop the zero energy Hall plateau induced by localized states. The difference in slope in σ_{xy} probably relates to 3 sets of delocalized states, namely two sets of disorder percolated states and one set of bulk pristine graphene delocalized

states. This latter central set has a different scaling behavior because of the competing effect of disorder at $E = 0$.

4.4 Comparison with Experiment

Presently, no experiment has been conducted yet on this specific divacancy case. Two hurdles need to be overcome to achieve the necessary experimental conditions. Firstly, a adequate functionalization method is required to obtain a random distribution of divacancies (or oxygen atoms in epoxy position, as will become clear in the next Chapter). For oxygen atoms, the group of Prof. Hersam has developed such technique [112]. Secondly, high magnetic fields in the tens of Teslas might be necessary to fully develop a new zero energy Landau level. Fields as high as 45 Tesla can be reached in the DC regime, while using pulsed magnetic fields, one can get close to 100 Tesla, at the time of writing. Such experiments are very costly and require very skillful experimentalists. Particular attention is probably also required to avoid contamination of the measurements by the edges playing an important role carrying delocalized states. The edges could shunt out the observation of the disorder-specific states.

Very recently, an experimental paper was published, which could very well be related to the physics described in this Chapter. Y. W. Nam *et al.* have performed QHE measurements on graphene grown by chamical vapour deposition. The samples were irregularly decorated with disordered multilayer graphene patches and, possibly, with hydrogen atoms. The authors tentatively relate the unusal dip in σ_{xx} and plateau in σ_{xy} with disorder related physics (see Fig. 4.6). Nevertheless, the discussion is very speculative at present and would require additional characterization and measurements to confirm if the model developed in this Chapter explains their observations. There is reason to believe it is, as the multilayer graphene patches might act as antidot disorder centers (for which the divacancy is the smallest sublattice preserving example), carrying circumventing magnetic field bound states [113, 114, 115]. Also the authors claim that, at zero energy, (localized) states are present

rather than that a real bandgap develops. This is consistent with the present model. Further measurements to clarify the origin of this new zero energy plateau might include checking if the magnetic field dependency agrees with the scaling depicted in Fig. 5.25 in the following Chapter.

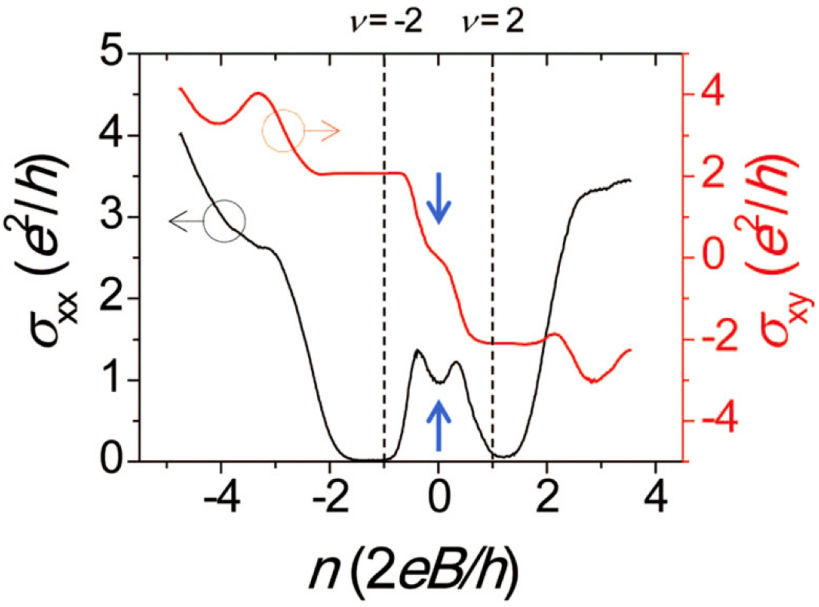

Figure 4.6: Longitudinal and Hall conductivity versus the carrier density n. Arrows indicate an unusual dip in σ_{xx} and platau in σ_{xy}. Figure taken from Nam *et al.* [116].

4.5 Conclusions and outlook

In this Chapter, unexpected critical states are observed both in the σ_{xx} and σ_{xy} curves. These states have been linked to the specific role of the disorder. The energy of these states is dependent both on the impurity concentration and the magnetic field strength. A new zero energy Landau level appears for sufficiently high divacancy concentration.

To conclude this Chapter, let's try to give a physical interpretation to this particular behavior. Note that this interpretation is speculative and requires further thought.

From the realspace density plots in Fig. 4.4, the spatial extent of the states seem to be different from energy to energy. Specifically, at the highest energy [(d) panel], the state seems to cover the impurities more uniformly. How to interpret the existence of such a state covering up all the divacancies?

For sake of simplicity, let's first go back to Fig. 4.3. There, only two sets of divacancies are considered. Reducing the divacancy to a single atom, giving rise to one resonant energy state [blue curve, panel (a)], the latter can be viewed as an atomic orbital. By bringing two such divacancies with their respective atomic orbitals together, they start to interact, creating a molecular orbital with a bonding and anti-bonding contribution (red curve). An crude analogy with molecules is thus achieved. Surprisingly, the state of lowest energy is anti-symmetric and the one of highest energy is symmetric in the sense that it has quasi-spheric symmetry with highest density concentration between the two divacancies.

Extending this analysis and analogy for the two divacancies to the set of 50 divacancies in Fig. 4.4, the latter should behave like a molecule containing 50 atoms. And so, the state covering up all atoms, would be the most symmetric contribution stemming from the hybridization of all 50 atomic orbitals. To fill this state, higher energy electrons are required than the ones required to fill the low energy anti-symmetric states, which makes it tricky to use the same bonding/anti-bonding terminology as for molecular physcis where symmetrically bonding states are filled first.

The same analogy can be made for the hole contribution to the current, by looking at the similar resonant states at negative energies (not shown here).

Thanks to this analogy, it is tempting to think of the system of divacancies as a hugh *quasi*-molecule carried by the graphene lattice. The bond lengths between the atoms making up this artificial molecule are much larger than the ones in conventional molecules. The distance

between divacancies is equal to 2.5 nm for a concentration of 0.5% for instance, which is much larger than a normal interatomic distance in the Å-regime. Graphene thus seem to play an important role as a medium to carry the electrons between functionalizing atoms.

Further calculations are required to check the validity of this picture. For instance, by increasing the magnetic field which has smaller magnetic length (or similarly, decreasing the impurity concentration), the effect of the distance between impurities can be assessed on the robustness of such extended state. Up to now, all cases studied in this Thesis have magnetic lengths which are larger than the distance between impurities. One can expect that at some point, the interaction becomes to weak to develop a truly disorder-induced extended (*quasi*-molecular) state. Indeed, for lowest concentrations (0.25 and 0.5%) the LL0 seems to robust for longer time. The spatial extent of this magnetic field dependent resonant state decays exponentially away from the impurity, hinting towards an exponentially decaying interaction radius. A first calculation at 1280 T, which has a magnetic length of 0.71 nm, and thus, if doubled to get the diameter of the interaction surface, 1.42 nm (which is smaller than the average distance of 2.5 nm between impurities), confirms that the contribution from these satellite impurity states to σ_{xy} becomes negligible. Calculations are still preliminary and thus go outside the scope of this work.

It is worth mentioning that this analogy of a *quasi*-molecule inside the graphene lattice is only valid at finite magnetic field. At zero field, the orbitals of the atoms do not seem to couple to form such extended state. The zero field analysis is performed on a more realistic oxygen model in the next Chapter.

Chapter 5

Epoxy Oxygen

5.1 Introduction

This Chapter discusses the results obtained for a random functionalization of graphene with oxygen atoms in *epoxy* position. Such oxygen atoms are more elaborate versions of the academic divacancy model presented in the previous Chapter, as was shown in Fig. 4.1. These impurities are modeled using accurate DFT calculations, which makes comparison with real disorder in experimental samples more reliable and meaningful.

In a first stage, the objective is to explain results obtained by the group of Prof. A. Bachtold, who treated graphene samples with an ozone flux. Such flux mainly induces impurity sites of oxygen atoms in epoxy position [110]. Unfortunately, no STM images are availabe for these samples. Experimental measurements hinted towards quantum localization phenomena in these samples (see Figs. 5.1 and 5.2, both taken from Moser *et al.*[22]), which is confirmed in Section 5.2 by simulation. Figure 5.1 pictures the effect of increasing the temperature on the resistance of the treated ozone sample. Temperature has the tendency to break the phase coherence which is required to have constructive interference between counterpropagating paths, and so, resistivity should decrease, as is observed. In Fig. 5.2, magnetoresistive measurements confirm the localization interpretation, because a magnetic field also breaks the phase coherence (because it does not preserve time reversal symmetry).

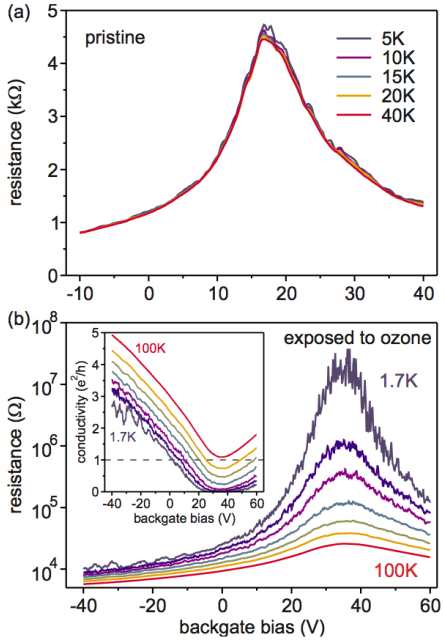

Figure 5.1: Four-point resistance before (a) and after (b) ozone treatment. Resistivity decreases with temperature in (b).

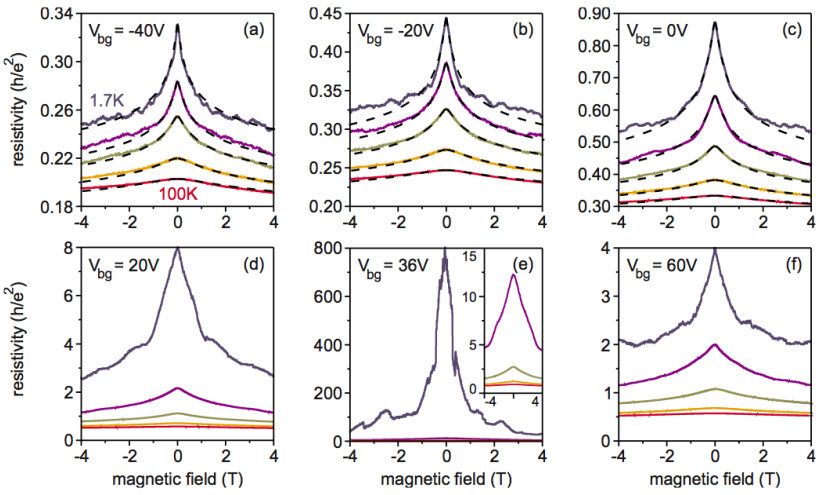

Figure 5.2: Resistivity of the ozonated sample as a function of magnetic field at different back gates voltages. (e) corresponds to the Dirac point energy.

Recently, the group of Prof. M. Hersam developed an oxidation method which allows for a truly random distribution of oxygen atoms in epoxy position on the graphene sample [112]. This is shown by STM in Fig. 5.3, making it a promising sample preparation approach for future experiments required for the second step of the study.

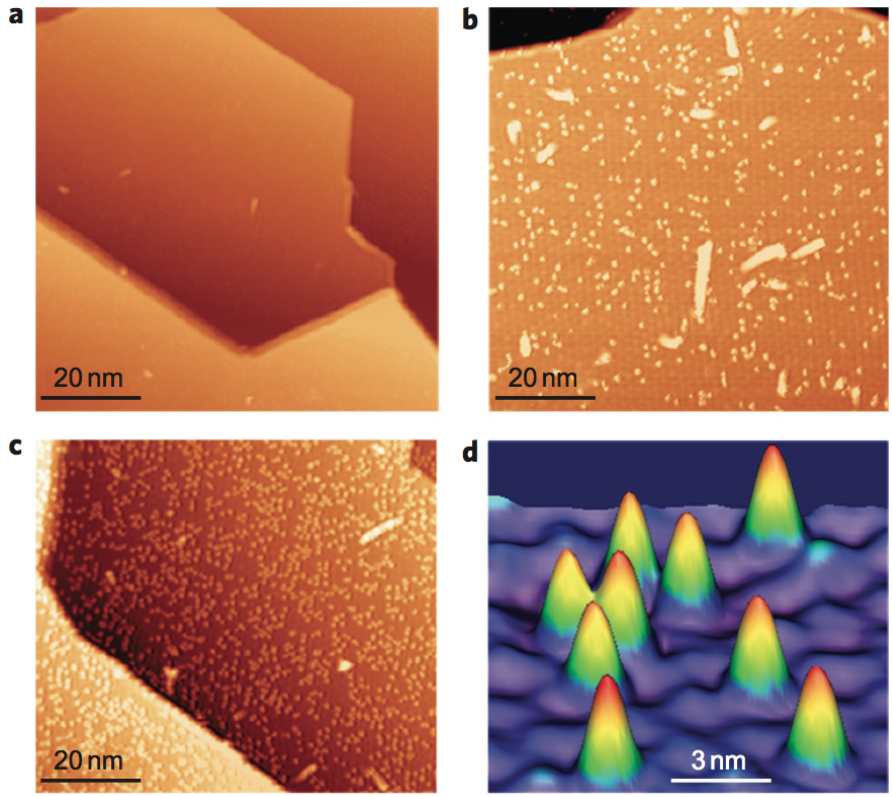

Figure 5.3: STM images taken from the paper by M. Z. Hossain [112]. (a) epitaxial graphene. (b) and (c) exposure to atomic oxygen at different dose. Bright protrusions are attributed to chemisobed oxygen atoms. (d) 3D rendered STM image of nine chemisorbed oxygen atoms.

In this second step, an external magnetic field is included to complement the σ_{xx} and σ_{xy} calculations from the previous Chapter on divacancies, by working on this more realistic disorder model. Similar disorder-dependent critical states are observed, as well as a different, and surprising, non integer quantization of the step height in the QHE.

5.2 Zero Field Limit

5.2.1 From *Ab Initio* to Tight-Binding Models

To start, a good understanding of the impurity potential is acquired before extracting TB parameters for implementation in the Kubo formalism. This is achieved in this Section.

Fig. 5.4(a) illustrates the oxygen atom in epoxy position after *ab initio* geometry optimization. In order to investigate the chemical bonding of oxygen on graphene, the charge density difference is calculated. Plotting such charge density difference allows for a visual understanding on how the electronic clouds associated with the orbitals are altered by chemical bonding. Fig. 5.4(b-c) illustrates this charge density difference ρ^{diff} defined as follows:

$$\rho^{\text{diff}} = \rho^{\text{tot}} - \rho^{\text{O}} - \rho^{\text{graph}} \tag{5.1}$$

where ρ^{0} and ρ^{graph} represent the charge densities of freestanding oxygen and graphene respectively. ρ^{tot} is the charge density of the total system in its bound state.

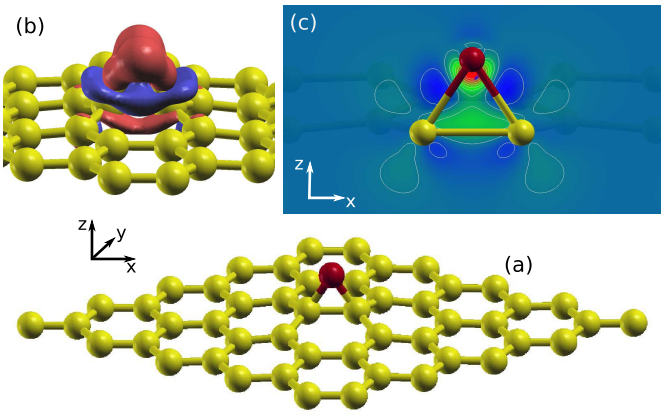

Figure 5.4: An oxygen atom in epoxy position on a 5×5 cell (a). 3D (b) and 2D (c) charge density difference as defined in Eq. (5.1). Charge accumulation in red/green and charge depletion in blue. Isovalues of 0.006 $|e|/\text{Å}^3$ and -0.006 $|e|/\text{Å}^3$ for the 3D charge density difference.

In Fig. 5.4(b), the charge accumulation in red and the charge depletion in blue indicate a covalent bonding between the carbon and the oxygen atoms. Oxygen is known to exhibit an acceptor behavior (attracts electrons on the s and p_y orbitals). Its p_y orbital does not participate in the bonding as the electronic cloud around the oxygen keeps its conventional p-orbital form.

In Fig. 5.4(c) the accumulation of electrons is rendered in red and green and the depletion in blue. The typical π-orbitals of sp^2 graphene are broken by the epoxy bonds. Indeed, this bonding causes a charge depletion (blue region) in the π electron cloud located above and under the σ bond associated with the underlying carbon atoms. The latter σ bond thus encounters a slight charge accumulation (green region). Additionally, the electronic charge transfer calculated with a Hirshfeld [117, 118] (Voronoi [118, 119]) integration adds up to -0.256 $|e|$ (-0.266 $|e|$) of charge transfer towards the oxygen (red and green region close to the oxygen atom), which indicates that the bonding is also slightly ionic. These two integration techniques yield better results than the frequently used Mulliken integration since they are basis independent [120]. The oxygen bound in epoxy position is found to perturb graphene, but not in a purely sp^3-hybridization way as in the hydrogenation case.

A Crystal Orbital Hamilton Population (COHP) study [121, 122] partitions the band structure energy in terms of orbital pair contributions. Positive density values represent the bonding states, while negative values describe anti-bonding states when plotting the conventional -COHP. Fig. 5.5 presents a COHP study on the orbitals participating to the bonding between the oxygen atom in epoxy position and its neighboring carbon atom. In the following analysis, conclusions are drawn for the region of interest for transport properties $[-1\text{ eV}; 1\text{ eV}]$ only; given bonds may have different bonding or antibonding behaviors away from the Fermi energy.

One first notes that the contributions of the s [panel (a)] and p_z [panel (c)] orbital of oxygen bonding with a neighboring carbon are analog. Both these orbitals have a dominant antibonding contribution with the p_x and s orbital of carbon at the right of the Fermi energy. The

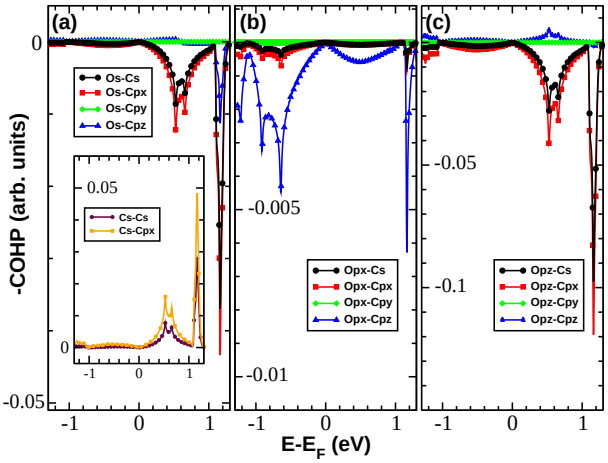

Figure 5.5: *Ab initio* COHP analysis of the orbitals participating to the bonding of the oxygen atom in epoxy position with its neighboring carbon atoms. Region of interest between -1 eV and 1 eV with respect to the Fermi level. Positive and negative values indicate bonding and antibonding interactions, respectively. (a), (b) and (c) panels correspond to s, p_x and p_z orbitals of oxygen, respectively.

COHP study between both first neighboring carbon atoms [Fig. 5.5 (a), inset] shows that these two orbitals of carbon, also responsible for the σ bond hybridization, strongly bind at the same energies ($E \sim 0.5$ eV and 1.2 eV), with analog contributions, typical for the σ-like hybridization between carbon atoms. These four orbitals (O_{p_z}, O_s, C_{p_x} and C_s) thus form a hybridized electronic cloud with bonding contributions between the two carbon atoms and antibonding contributions between oxygen and carbon. This result is in agreement with the charge density rearrangement observed in Fig. 5.4. The electronic charge depletion of the π orbitals observed in Fig. 5.4 can be rationalized with a COHP study for a larger energy window (not shown here). The π electrons are partly drawn into the σ bond between the carbon atoms. The remaining p_z electrons of carbon [blue lines in (a), (b) and (c)] interact mainly with the p_x, p_z and s orbitals of oxygen. Finally, the p_y orbital of oxygen does not interact with carbon in this energy window.

Consequently, a TB model with first-neighbor interactions including both p_x and hybridized s/p_z orbitals of oxygen with the p_z and s/p_x orbitals of carbon should be sufficient to accurately model the effect of epoxy groups on graphene. The combined contributions of the three orbitals of carbon binding with oxygen is renormalized to only one orbital in a π-like model. The matrix elements of the TB Hamiltonian are given by:

$$\mathcal{H}_{ij} = \sum_{ij} \gamma_{ij} a_i^\dagger a_j + \sum_i \epsilon_i a_i^\dagger a_i. \tag{5.2}$$

At first, a $\sqrt{3} \times \sqrt{3}$ R 30° supercell with one epoxy atom was simulated using DFT to extract a band structure with limited folding of the Brillouin zone (not shown here). The bands near the Fermi energy are nicely fitted using the following TB parameters [nomenclature, see Fig. 5.6(c)]: $\epsilon_x = -2.5$ eV, $\epsilon_z = -1.0$ eV, $\epsilon_1 = 1.5$ eV, $\gamma_x = 1.8\gamma_0$, $\gamma_z = -1.5\gamma_0$ and $\gamma_1 = 0.0$ eV with $\gamma_0 = -2.6$ eV.

Finally, to confirm the validity of the model, these TB parameters are used to generate the band structure of a 5×5 supercell containing a single epoxy oxygen, which is superimposed with its DFT counterpart [see Fig. 5.6(a)]. The electronic path chosen to plot the band structure contains all inequivalent high-symmetry segments in the 2D Brillouin zone of a 5×5 graphene supercell [123] [see Fig. 5.6(b)]. Note the band crossing at the Fermi energy is shifted away from the K_2 point. The localized flat band (visible around the Γ point) appearing in the DFT band structure around -2.5 eV is missing in the TB band structure. This originates from a strong interaction between the p_y orbital of oxygen with the p_y orbital of carbon. Both orbitals are missing in the TB model. These band structures were calculated for one orientation of the epoxy group on graphene[see Fig. 5.6(d)]. For the two other possible orientations of the epoxy oxygen the crossings occur close to K_1 or K_3 for symmetry reasons. In conclusion, the TB model seems to be sufficient to accurately model random positions and random orientations of impurities, as long as these epoxy oxygens do not notably affect each others local potential, which is assumed to be satisfied for the range of concentrations of impurities considered here. These range of concentra-

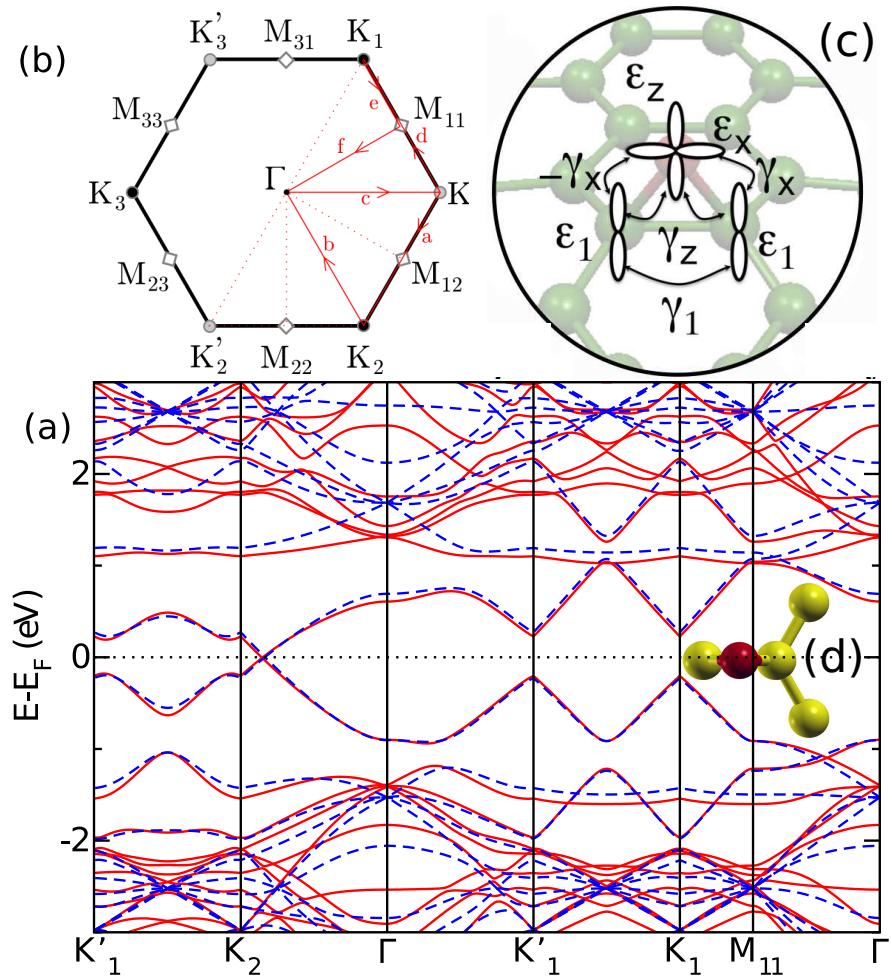

Figure 5.6: Electronic band structure of a 5×5 graphene supercell containing a single epoxy group. The DFT (red-solid) and TB (blue-dashed) band structures (a) are described along high-symmetry paths as described in the Brillouin zone (b). Nomenclature of extracted TB parameters is illustrated in (c). One possible orientation of the oxygen atom in epoxy position is described herewith. The two other inequivalent orientations are obtained by rotating the oxygen atom in epoxy position by 120° around the central carbon atom in (d).

tions are close that what is experimentally accessible with the method of the group of Prof. Hersam [112]. For the ozonation method, no concentration characterization is available.

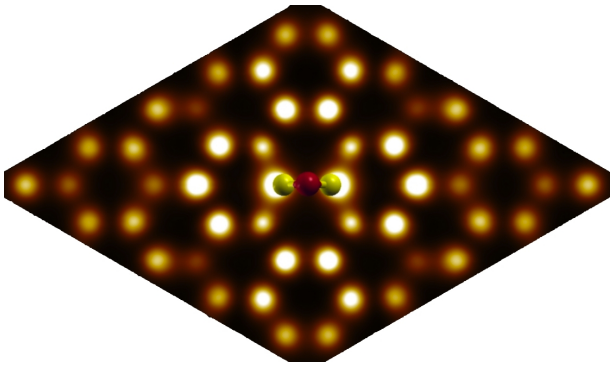

Figure 5.7: DFT STM image of empty states, *ie.* Local DOS for one oxygen atom in epoxy postion, integrated between 0 and 0.5 eV. Both sublattices are affected equally preserving the pseudospin symmetry in graphene.

Eventually, in Fig. 5.7, the twofold D_{2h} symmetry in the simulated STM image obtained by integrating the local DOS (LDOS) proves the analogy with a double impurity defect, by comparison with the LDOS in Fig. 2 of Ref. [124]. The LDOS of empty states is spatially integrated between 0 and 0.5 eV. A similar pattern (in the sense of preserved sublattice symmetry, not shown here) is obtained for hole carriers, by integration between and 0 and -0.5 eV.

5.2.2 DOS and Energy Shift

The evolution of the DOS, calculated from Tr $\left[\delta(E-\hat{H})\right]$, with increasing impurity density is reported on Fig. 5.8. The termination term (see Section 3.2.2) is the one usually used for metals, which considers that the oscillation of the recursion coefficients is rapidly damped with the number of recursion steps. After 500 recursion steps damping is sufficient, although a very small remnant oscillation caused by the small energy gap at high energy is observed. This is quantitatively correct at low energies and qualitatively sufficient at the border of the energy

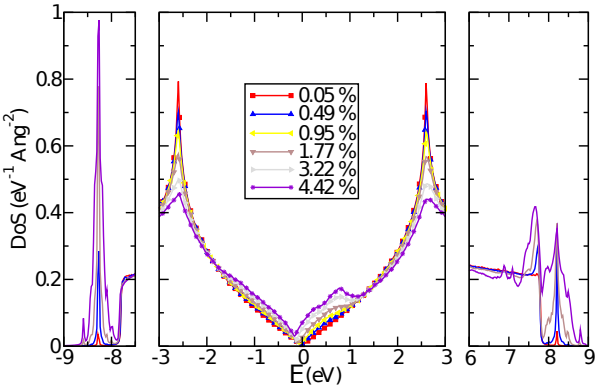

Figure 5.8: Main frame: DOS for various impurity densities ranging from 0.05 to 4.42 %. The minimum of DOS shifts slightly with the addend concentration due to the changes in hopping parameters and on-site energies in the TB model. Side panels: δ-like peaks corresponding to impurity bands at lower (left) and higher (right) energies.

spectrum where the energy gaps occur, by comparison with other more sophisticated termination methods.

Although DFT calculations on similar concentrations exhibit a shift of the Fermi energy compared to the pristine case, no shifts are applied yet to point out the similarity with other studies [125, 126] covering the effect of ideal impurities (*ie.* the influence of the change of respectively the on-site energy and the hopping parameters) on the DOS of pristine graphene.

A apparent shift (before pinpointing the exact position of the Fermi energy, by integration) of the minimum of the DOS is observed with increasing impurity concentrations. Even though formally the rigid band theorem cannot be used for atoms that do not have the same valence (*ie.* carbon and oxygen) [29], the shift is found to be linear with increasing concentrations (x) and the second order corrections $O(2)$ can thus be neglected [see Fig. 5.9 (inset)]:

$$\Delta\epsilon_n = xU + \mathcal{O}(2) + ... \tag{5.3}$$

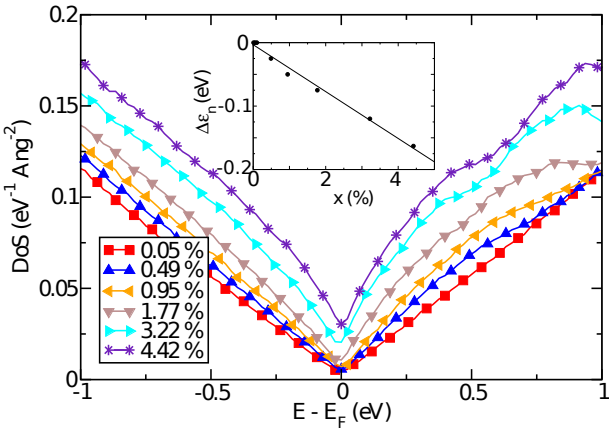

Figure 5.9: Main frame: Realignment of the minimum of DOS and charge neutrality point (CNP: position obtained by DOS integration) at 0 eV. Inset: linear increase of energy shift $\Delta\epsilon_n$ with increasing concentrations of epoxy groups (x in %). Rigid band theorem (see text) implies an impurity induced potential of ~ -3.7 eV.

where U is the local potential induced by the epoxy defect. A linear fit of $\Delta\epsilon_n$ versus x implies a value of U equal to ~ -3.7 eV.

In addition, the Van Hove Singularities (VHS) are smoothened out and decreased in amplitude with increasing concentrations of epoxide groups, in agreement with previous observations [97, 125, 126]. Also, a small increase of the DOS appears at the minimum of the DOS with increasing impurity concentration.

The bumps in densities of states on the left and on the right of the minimum of DOS (Fig. 5.8, middle panel) correspond to the resonant energies between the oxygen atoms in epoxy position and the graphene sheet [124], while the δ-like peaks in the side panels at high energies correspond to flat impurity bands. As discussed in Section 5.2.1, the localized state close to the left VHS caused by the strong interaction between both p_y orbitals of oxygen and carbon is missing in this simplified TB model.

Finally, oxygen in epoxy position triggers a shift of the Fermi energy which compensates the shift of the minimum of DOS discussed above (see Fig. 5.9). This Fermi energy is obtained by integrating the TB DOS

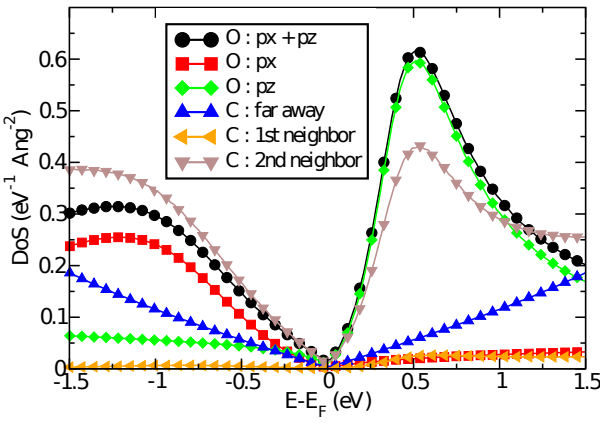

Figure 5.10: PDOS. The p_x (p_z) orbital of oxygen mainly contributes on the left (right) side of the Fermi energy. Negligible contributions are predicted for first-nearest neighboring carbon atoms. Second carbon nearest neighbors do contribute to the resonant energy bump with oxygen.

and counting the number of electrons present in the system. In the next Sections, transport calculations will implicitly include this realignment of minimum of DOS with the Fermi energy, thus locating the charge neutrality point (CNP) at $E = 0$ eV.

In Fig. 5.10, a Projected DOS (PDOS) evidences that the bump on the right side of the Fermi level originates from the p_z orbital and the one on the left from the p_x orbital of oxygen, in agreement with the previous COHP DFT study. Fig. 5.10 also indicates that the first-nearest neighboring carbon atoms do not contribute to the total DOS in contrast to the second nearest neighboring carbon atoms. The PDOS suggest the oxygen atom attracts most of the electronic density and thus weakens the density on the first-neighboring carbon. Such analysis agrees with existing literature [78, 127] and with the STM image in Fig. 5.7.

5.2.3 Diffusion Coefficient and Transport Regimes

The diffusion coefficient $D(t)$ inherently contains all the information needed to calculate transport properties [see Eqs. (3.31) and (3.32)].

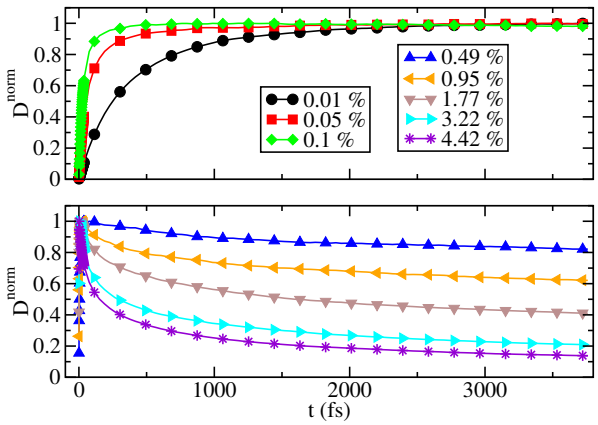

Figure 5.11: Time evolution of diffusion coefficient (normalized) at $E = 0.5$ eV for different impurity concentrations.

Its time evolution or dynamics also clarifies the dominant transport regime at the considered time scale (*ie.* ballistic, diffusive or localized). Fig. 5.11 illustrates the typical behaviors of the normalized diffusion coefficients

$$D^{\text{norm}}(t) = \frac{D(t)}{D^{\text{max}}} \tag{5.4}$$

for an energy $E = 0.5$ eV. This energy is chosen as illustration because disorder effects are more prominent there in the DOS curve. As expected, the conduction in pure graphene is simply ballistic. The smallest simulated impurity concentration (*ie.* 0.01 %) does not reach its maximum for the diffusion coefficient for the total elapsed time considered here (approx. 3800 fs). The slope of $D(t)$ gives access to a $v^2(E)$ value still in close agreement with the theoretical (analytical) value v_F^2 for energies E close to E_F. For instance, at 0 eV and for 0.01 %, $v(E) = 2.11\text{Å}\gamma_0/\hbar$, while $v_F = 2.13\text{Å}\gamma_0/\hbar$. For intermediate concentrations (0.05 and 0.1 %) $D^{\text{norm}}(t)$ evolve from the ballistic regime to the diffusive regime for the simulated times. At higher concentrations (0.49 %) $D^{\text{norm}}(t)$ reach a diffusive regime sharply, followed by a clear decrease with time, signature of quantum interferences leading the charge carrier localization.

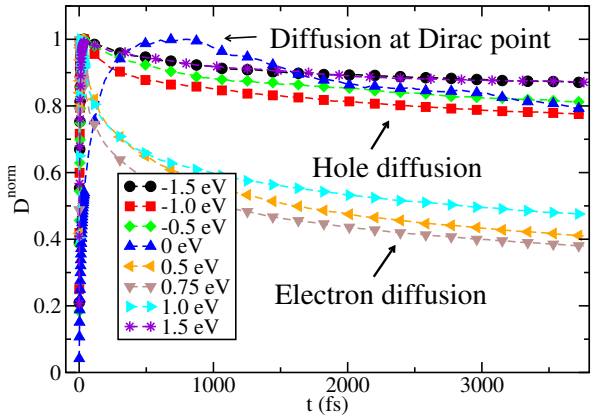

Figure 5.12: Normalized diffusion coefficient versus time for $x = 1.77$ % at different energies.

Fig. 5.12 presents diffusion coefficients $D^{\mathrm{norm}}(t)$ of 1.77 % of impurities at different energies. Localization effects follow an asymmetric behavior between electrons and holes. The predominant resonant peak at the right of the charge neutrality point (CNP) causes much stronger localization effects than the weaker and more smeared out peak at the left of the CNP (in analogy with the PDOS in Fig. 5.10). Such asymmetry is of crucial importance to synthesize possible electronic devices made of functionalized graphene requiring an efficient switch between a conducting and an insulating behavior [128, 129]. Localization effects are more significant around 0.75 eV. One finally notes the peculiar behavior of the diffusion coefficient exactly at the CNP. Numerically, this point is more problematic to simulate since the density of charge carriers may be very scarce. Nevertheless, the results suggest that the saturation limit of the Diffusion coefficient is reached for longer simulation time and then turns into a moderate decrease characteristic of quantum effects.

This discussion on the diffusion coefficient points out two different regimes which are approached separately in the remaining Sections. Firstly, the semi-classical quantities, which neglect quantum effects, are discussed in Section 5.2.4. Secondly, the localization regime is analyzed in Section 5.2.5.

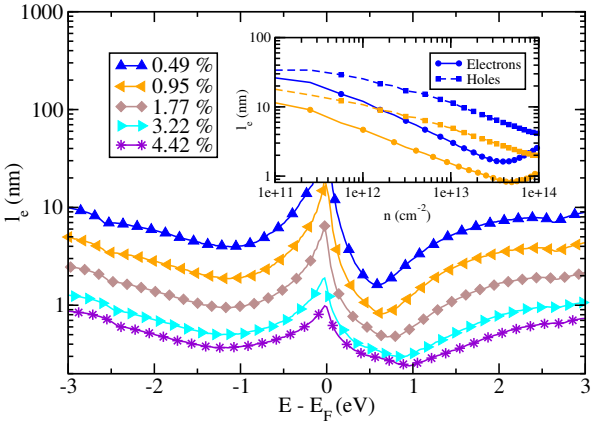

Figure 5.13: Energy dependent mean free paths for different impurity concentrations. Inset: mean free path versus hole (dashed/squares) and electron (solid/circles) carrier density for epoxy concentrations of 0.49 % and 0.95 %.

5.2.4 Semi-Classical Regime

Analysis of Elastic Mean Free Paths

Using Eq. (3.31), the mean free path ℓ_e is calculated using the diffusion coefficient and plotted in Fig. 5.13 for energies between the two VHS at -2.6 eV and 2.6 eV. For the considered elapsed times, the diffusive regime is not reached at every energy for the smallest impurity concentrations (*ie.* $n_i < 0.1$ %, see Fig. 5.11, upper panel). Therefore, the mean free path can not be estimated for these small concentrations. For concentrations larger than 0.5 %, the diffusive regime is reached within the entire energy window. The dip in the mean free path at the right of the CNP (and in a lesser extent, at the left of the CNP), indicating larger scattering effects, shifts away from the CNP and becomes smoother with increasing concentration of oxygen atoms in epoxy position. Such dips correspond to the resonance peaks found in the DOS which are induced by the oxygen. The inset of Fig. 5.13 confirms the predicted asymmetry, affecting the electrons more strongly. The largest concentrations scatter more uniformly across the entire energy window. In addition, the evolution of the mean free path with impurity concentration follows a simple

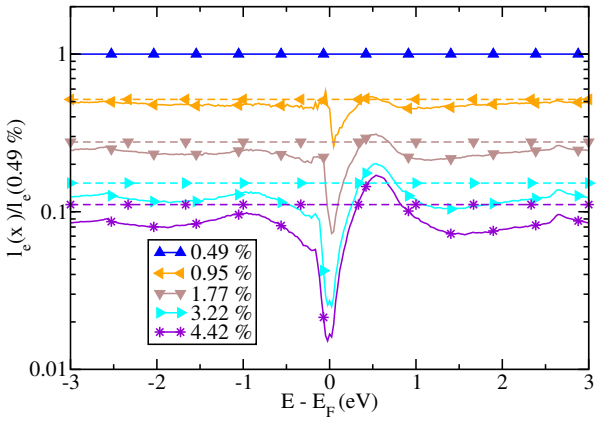

Figure 5.14: Ratio of mean free paths at two selected impurity densities. $\ell_e(x_1)/\ell_e(x_2)$ (solid lines) and x_2/x_1 (dashed lines) with $x_2 = 0.49$ %.

scaling law as expected from a Fermi golden rule (Fig. 5.14):

$$\frac{\ell_e(x_1)}{\ell_e(x_2)} = \frac{x_2}{x_1}. \tag{5.5}$$

Such scaling is straightforward to explain because the mean free path is of the order of the distance between impurities, the latter being linear with the impurity concentration. Agreement fails at the Dirac point and gets worse for higher concentration.

Mobility

In Fig. 5.15 (mainframe) the mobility of the charge carriers is estimated theoretically using:

$$\mu(E) = \frac{\sigma_{\rm sc}(E)}{ne}. \tag{5.6}$$

Scattering effects are affecting the electron mobility more strongly than the hole mobility. This asymmetry is reduced for the largest impurity concentrations [see Fig. 5.15 (inset)]. The gate voltage V_g was estimated from the experimental gate capacitance C_g ($\sim 1.1510^{-4}$ Fm$^{-}2$), using $n = C_g V_g/e$ and $k = \sqrt{\pi n}$.

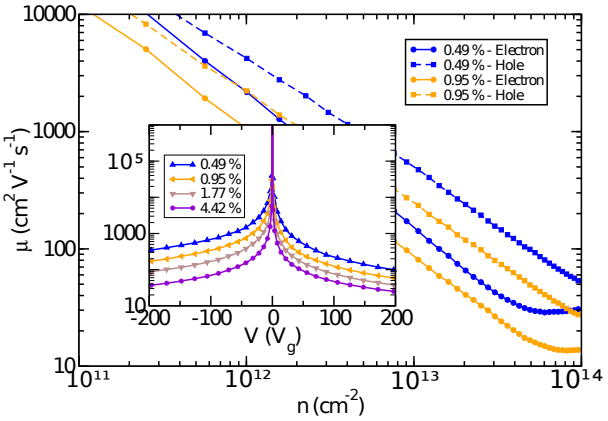

Figure 5.15: Main frame: electron and hole mobility for usual experimental carrier densities. More severe scattering effects for negative charge carriers cause an asymmetry in mobility compared to the hole mobility. Inset: same mobilities with respect to the gate voltage V_g.

Experimentalists usually consider the absolute value of the mobility as a key quantity to characterize samples and corresponding inherent disorder. Temperature breaks the phase coherence of electrons along the scattering path and generally reduces quantum interference effects. Accordingly, the use of the semi-classical conductivity in evaluation of $\mu(E)$ (Eq. 5.6) is a reasonable approximation to analyze the experimental data. On the same basis, computed semi-classical conductivities are expected to be more valuable for comparison with conductivities measured experimentally at room temperature. One may argue that in such a non-zero temperature environment, electron-phonon coupling may play also a significant role. However, inelastic scattering lengths due to electron-phonon coupling are extremely long in graphene and may thus be disregarded too, at least as a first approximation.

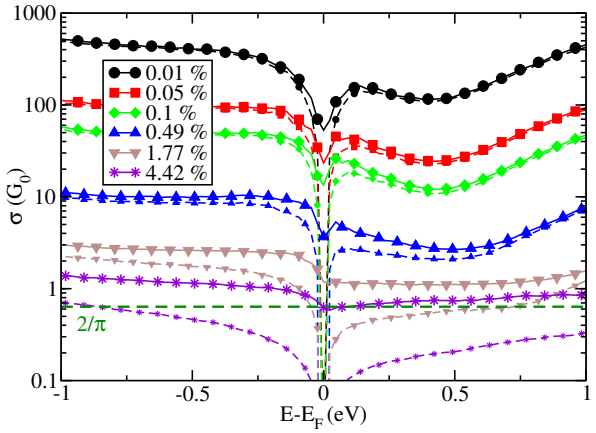

Figure 5.16: Comparison between the numerical Kubo conductivity $\sigma_{\rm sc}$ (solid lines) and the Drude approximation $\sigma_{\rm D}$ (dashed lines) for different impurity concentrations. Minimum theoretical value $2/\pi G_0$ is plotted in horizontal dashed green line.

Numerical Kubo Conductivity and Drude Approximation

The semi-classical Kubo-Greenwood conductivity $\sigma_{\rm sc}$ can be compared to the Drude approximation close to the Dirac point:

$$\sigma_{\rm D}(E) = \frac{4e^2}{h}\frac{k(E)\ell_e(E)}{2} \tag{5.7}$$

where $E = \hbar v_{\rm F} k$ with v_F the Fermi velocity close to the Dirac point ($d_{cc} \approx 1.42$ Å):

$$v_F \approx \frac{3\gamma_0 d_{cc}}{2\hbar} \approx 1 \times 10^6 m s^{-1} \tag{5.8}$$

The limitations of the Drude approximation are put into context in a Review paper[130] and the limitations of the Born approximation in the Boltzmann theory of conductivity have been analyzed in Ref. [131].

Fig. 5.16 compares the semi-classical value of the Kubo-Greenwood conductivity $\sigma_{\rm sc}$ (solid lines) with the Drude conductivity $\sigma_{\rm D}$ (dotted lines), extracted from Eq. (3.32) and (5.7) respectively. The Drude approximation seems to be valid only for small impurity concentrations in the energy window $[-1\ {\rm eV}; 1\ {\rm eV}]$. For larger densities, the conduc-

tivities are underestimated by a factor of two for energies close to the CNP. Moreover, σ_{D} is ill-defined at the CNP [see Eq. (5.7)]. Indeed, at the CNP, $k = 0$ and consequently, σ_{D} vanishes. However, theoretical work [98, 132, 133] reports extensively on a minimum value of the semi-classical conductivity equal to $2/\pi G_0 = 4e^2/\pi h$ (when neglecting quantum interferences). To avoid the singularity at 0 eV, the mean free path could be calculated analytically, including its k dependence explicitly. As illustrated by the calculations for larger impurity concentrations, the variations of the DOS with disorder have to be included, as it is presently the case in the Kubo formula [Eq. (3.32)]. These variations account for single and multiple scattering events mentioned in Ref. [134]. Up to some numerical discrepancy, the semi-classical minimum value of conductivity is confirmed.

Additionally, an asymmetry exists between the electron and hole conductivities. This effect is weakened but not cancelled with increasing impurity concentrations. This is similar to the asymmetry already observed for both charge carriers in their respective mean free paths and mobilities. Albeit physically different, the stronger quantum localization effects on the electron side are directly linked to the stronger classical scattering effects on the same energy window (see Fig. 5.12). This will be emphasized in Section 5.2.5 by studying the evolution of the conductivity with time deep into the diffusive regime.

Short-Range *vs* Long-Range Scattering

The nature of scattering range induced by oxygen atoms placed in epoxy position can be discussed using the scaling properties of semi-classical quantities. Both the scattering time and the conductivity are here briefly outlined [135].

The elastic scattering time is defined by

$$\tau(E) = \frac{\ell_e(E)}{v(E)}. \tag{5.9}$$

Using the dispersion relation $E = \hbar v_F k$, $\tau(E)$ can be estimated in terms of the Fermi wave vector k. According to Nomura *et al.* [136] who also

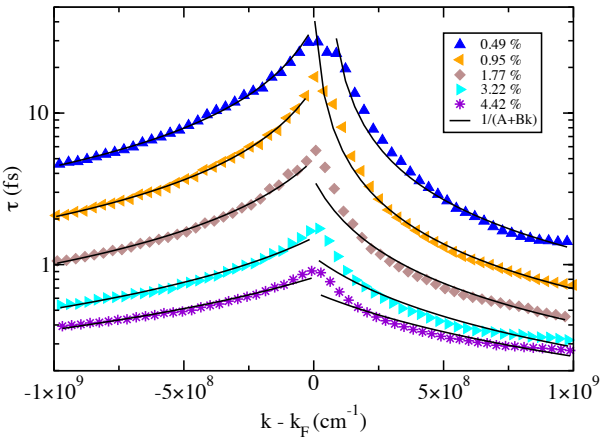

Figure 5.17: Scattering times in function of Fermi wave vector k for different oxygen densities. Numerical fits for each data set based on a regression algorithm with fitting parameters A and B (black) to account for the generalized inverse function. Hole and electron scattering times were fitted separately.

used the Kubo-Greenwood approach, the following conclusions apply. Long range (lr) and short range (sr) disorder scattering times scale respectively as follows:

$$\tau_{\mathrm{lr}} \propto k \text{ and } \tau_{\mathrm{sr}} \propto \frac{1}{k} \tag{5.10}$$

Following such criterion, the data with corresponding numerical fits (Fig. 5.17) clearly indicate a short-range scattering behavior of oxygen in epoxy position. Such short-range scattering time should diverge at the CNP. This does not happen within the Kubo formalism since the DOS remains finite close to the CNP, in contrast with the prediction of the Drude approximation.

A similar analysis based on the scaling of conductivity is not straightforward. According to Ref. [136], conductivity should scale linearly with n for long range disorder, while short range conductivity should display a non-linear behavior, approaching the constant Boltzmann (or Drude) conductivity σ_{D} for $|E_F| \gg \hbar/\tau$. In Fig. 5.16, the behavior close to the Dirac point behaves differently depending on the impurity concen-

tration. For smaller impurity concentrations, the conductivity tends to decrease for energies corresponding to reasonable carrier concentrations (up to 10^{13}cm^{-2}), while it increases slightly for larger impurity concentrations. The Drude conductivity never reaches a constant plateau for the whole of the energy E or carrier n range. The short-comings of this conductivity have already been pointed out.

This subject is still debated, as other models [39, 131, 132, 137] predict a dominant linear dependency (with logarithmic corrections) for both long range and short range conductivity.

Additionally, it has been observed experimentally [138] that a quasi-ballistic regime exhibits a non-linear behavior with n, while a more disordered system scales linearly with n. Comparison with experiment becomes particularly tricky as most of previously mentioned analytical models disregard important multiple scattering effects on the computed conductivity.

Another important remark is that most theoretical predictions have been derived assuming restrictions on disorder models which are partly invalidated in the present study. Indeed, the epoxy defects have been derived from accurate first-principle calculations, and the resulting TB model brings more realism and generality when compared to simplified academic models. As a matter of fact, the DOS (Fig. 5.9) evidences resonant energy bumps, driven by randomly distributed oxygen, which could cause squared logarithmic corrections [132]. The data cannot really be accurately fitted to obtain the different corrections to the scaling in this context.

This dominant short-range disorder is at the root of the quantum effects presented in the remaining Sections.

5.2.5 Evolution of the Kubo Conductivity with t (or L)

The semi-classical expression of the Kubo-Greenwood conductivity [Eq. (7)] restricts the transport to the diffusive regime, *ie.* when suppressing quantum interferences. To follow the time evolution spreading of the quantum wave packets, the expression of $D_x(t)$ in Eq. 3.26 should be replaced as follows:

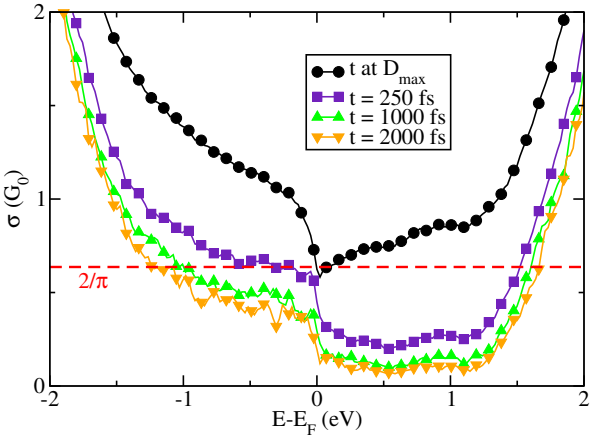

Figure 5.18: Kubo conductivities at different elapsed times of wave packet evolution for 4.42 % of impurities.

$$D_x(t) = \frac{\partial(\Delta X^2(t))}{\partial t} \tag{5.11}$$

When replacing $D^{\max}$ by the new expression of $D(t)$ in Eq. (3.32), the Kubo conductivities are obtained at different time scales as depicted in Fig. 5.18 for a 4.42 % impurity density. The time-evolution of the conductivity is found not to be uniform over the energy spectrum, indicating there might be different transport regimes depending on the charge carrier energies and impurity concentrations for a given length scale.

According to the scaling theory of localization [139], there are two possible behaviors for the conductivity corresponding to the weak and strong localization regimes which read as follows:

$$\sigma(L) = \sigma_{\rm sc} - \frac{e^2}{\hbar\pi^2} \ln\left(\frac{L(t)}{\sqrt{2}\ell_e}\right) \tag{5.12}$$

$$\sigma(L) \sim \exp\left(-\frac{L(t)}{\xi}\right) \tag{5.13}$$

where the localization length ξ gives an estimation of the distance covered by a charge carrier before it is totally trapped due to this multiple

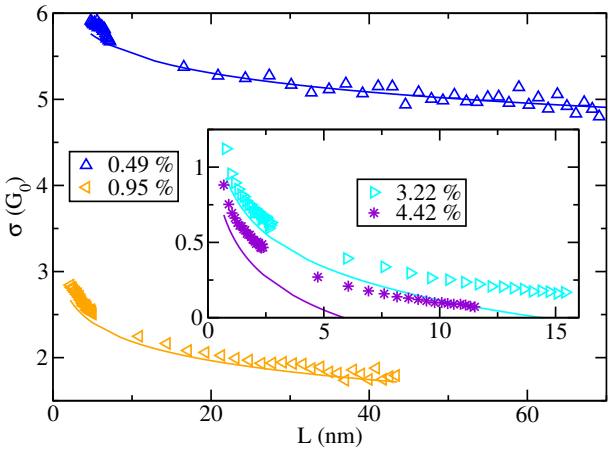

Figure 5.19: Kubo conductivities for $L > L^{\max}$, which include weak localization corrections to the semi-classical conductivity, for different impurity densities at energy 0.8 eV. The numerically estimated conductivity $\sigma(L)$ (obtained using Eqs. 5.11 and 5.14, symbols) contains numerical jiggling caused by the very sensitive derivation in Eq. 5.11. The conductivity obtained using Eq. (5.12) is plotted in solid lines. Only one out of five points are plotted in the inset for clarity reasons.

scattering effects. The exact prefactor for the weak localization correction is calculated in Appendix B. The diffusion length is defined as

$$L(t) = 2\sqrt{2\Delta X^2(t)}. \tag{5.14}$$

This definition of L is reasonable when saturation of the diffusion coefficient has been reached. The extra factor $\sqrt{2}$ in Eq. 5.12 compared to the correction obtained by Lee *et al.* [139] comes from a different definition of $D(t)$. Both numerical estimation of $\sigma(L)$ (symbols) and analytical $\left[\sigma_{\rm sc} - e^2/\hbar\pi^2 \ln\left(\frac{L(t)}{\sqrt{2}\ell_e}\right)\right]$ from Eq. (5.12) (solid lines) are plotted in Fig. 5.19 for $L > L^{\max}$. The numerical part contains small jiggling caused by the very sensitive derivation in Eq. (5.11).

The corrections to the semi-classical conductivity in the low impurity limit (mainframe) follows the logarithmic behavior, from which an estimation of ξ can be deduced. ξ corresponds to the length where the cooperon corrections equal the semi-classical conductivity [139]. Start-

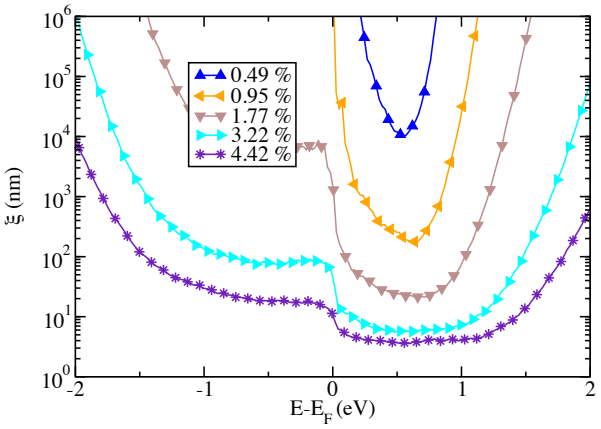

Figure 5.20: Localization lengths estimated using Eq. (5.15) for different impurity concentrations.

ing from Eq. (5.12), the localization length is thus estimated with

$$\xi(E) = \sqrt{2}\ell_e \exp\left(\frac{\pi\sigma_{\rm sc}}{G_0}\right) \tag{5.15}$$

with the computed ℓ_e and $\sigma_{\rm sc}$ and corresponds to the 2D generalization of the Thouless relationship [140, 141]. These localization lengths are plotted in Fig. 5.20.

For larger concentrations, the cooperon corrections to the semi-classical conductivity seem to saturate and depart from the perfect logarithmic behavior (Fig. 5.19, inset). The corrections obtained numerically become smaller than what is predicted due to a transition to the strongly localized regime following an evanescent exponential behavior. This can be rationalized invoking the Ioffe and Regel criterion [142] which states that the appearance of strong localization becomes significant for impurity concentrations satisfying $k_F\ell_e = 1$. Such a criterion implies a mean free path of the order of the interatomic distance, which is actually the case for 4.42 % of impurities where the mean free path is estimated to be below 3Å for the energy window from 0.5 eV to 1.0 eV.

In Fig. 5.21, by fitting the exponential behavior of Eq. (5.13), values for ξ equal to 8.4 and 4.8 nm are estimated for 3.22 % and 4.42 % of

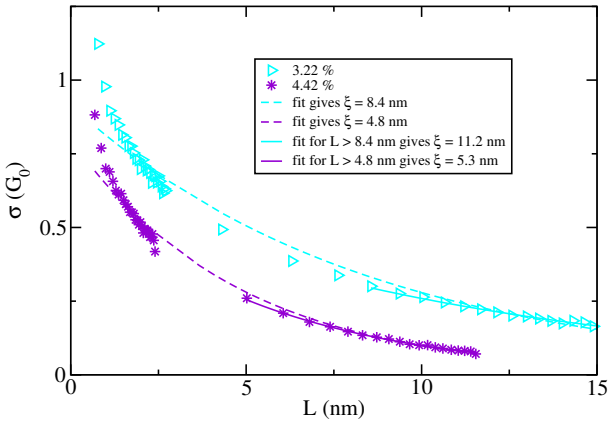

Figure 5.21: Exponential fits [Eq. (5.13)] to estimate localization lengths ξ in the strongly localized regime at energy 0.8 eV. A first fit (dashed lines) for the whole of the available data allows us to estimate a length L for which wavepackets are localized. A second fit (solid lines) for values larger than L gives us new estimates for ξ.

impurities respectively at an energy of 0.8 eV (dashed lines). Refitting $\sigma(L)$ for the region at the right of these values (solid lines), convincing exponential decays are obtained and more accurate estimates for ξ equal to 11.2 and 5.3 nm, respectively. Both these estimates and the ones obtained by Eq. (5.15) in Fig. 5.20 are of the same order of magnitude, thus validating the results. Experimentalists however often use the Drude approximation σ_D instead of the correct semi-classical conductivity $\sigma_{\rm sc}$ in Eq. (5.15). The inaccuracy of the Drude approximation for largest impurity concentrations causes the localization length to be underestimated by an order of magnitude.

5.3 Longitudinal Conductivity

While the previous Section focuses on the zero field limit, this Section scrutinizes the same systems under magnetic field. The effect of a perpendicular magnetic field is included in the TB model through the Peierls phase method (see Appendix H).

5.3.1 Disorder-Induced Asymmetry in QHE

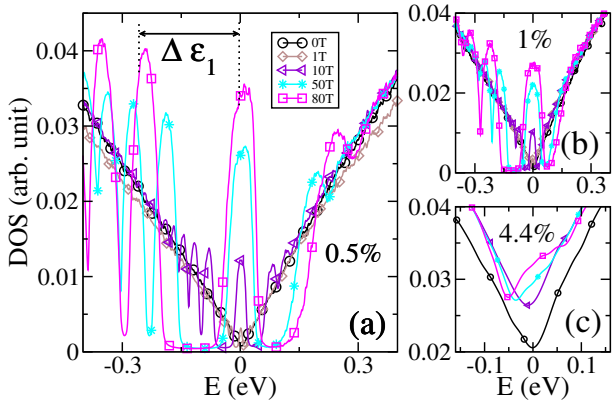

Figure 5.22: Density of states for various magnetic fields B and oxygen concentrations. Epoxy defect concentrations are 0.5% (a), 1% (b) and 4.4% (c) with the magnetic field ranging from 1 Tesla to 80 Tesla.

The evolution of the electronic structure under high magnetic fields is first scrutinized by varying the density of adsorbed oxygen impurities. Figure 5.22 presents the density of states (DOS) for three different epoxy defect densities, namely 0.5% (a), 1% (b) and 4.4% (c). For the lowest concentration of 0.5%, magnetic fields higher than 1 T are required to observe the onset of the zero-energy LL, whereas no LL signature is observed at higher energies for 1 T. By further increasing the field to 10, 50 and 80 T, the sequence of LLs clearly develops on the hole side of the spectrum, with distances between LLs ($\Delta\epsilon_n$) in full agreement with the expected $\sqrt{B}$ spacing (for example $\Delta\epsilon_1 \approx 0.3$ eV at 80 T)[65]. In contrast, LLs only partially develop in the electron region of the spectrum. The 1% density is also shown to inhibit any LL on the electron side of the spectrum, whereas the formation of LLs in the hole side becomes more difficult and requires higher magnetic fields. For densities as high as 4.4%, a total disappearance of LLs is observed throughout the whole spectrum and even fields as large as 80 T fail to generate the zero-energy level.

5.3.2 Magnetoconductivity Fingerprints

The conductivity σ is further analyzed for several representative defect densities and magnetic fields. Figures 5.23 (a) and (b) show $\sigma(E)$ in units of the conductance quantum ($G_0 = 2e^2/h$), computed at the largest accessible time scale ($t = 5.7$ ps) for impurity densities of 1% (a) and 0.5% (b) at $B = 80$T. The rescaled B-dependent DOS is superimposed (dashed lines) for the sake of comparison.

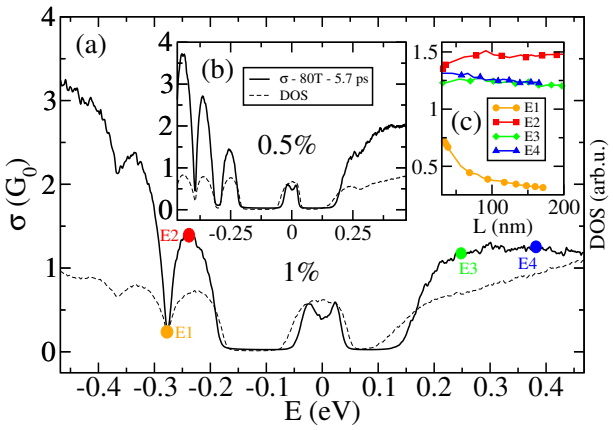

Figure 5.23: (a) $\sigma(E)$ in units of the conductance quantum for 1% epoxy defect density. (b) $\sigma(E)$ for 0.5% epoxy defect density. Dashed lines denote the corresponding (rescaled) DOS in both panels. (c) Length dependent $\sigma(L)$ at four selected energies indicated in (a).

The electron-hole asymmetry reported for the DOS consistently develops for the conductivity as well, and is even more pronounced. It is worth noticing that $\sigma(E)$ downscales with the defect density for sufficiently high electron energies (compare for instance Figs. 5.23 (a) and (b) at $E = 0.4$ eV), whereas it hardly changes for the lowest energy LL0, as well as for the first (LL-1) and second (LL-2) Landau levels on the hole side of the spectrum.

Figure 5.23(c) provides a clearer insight into the transport properties on the electron and hole side of the spectrum by showing the length-dependent conductivity σ at 80T for the selected electron energies E_1 to E_4 indicated in Fig. 5.23(a). On the electron side, at E_3 and E_4,

the conductivity slowly decreases with L, thus indicating the transition from diffusive to localized regime. This is consistent with the impeded formation of LLs in this energy region. On the hole side of the spectrum, E_2 corresponds to the σ peak (LL-1 center) and E_1 corresponds to the σ minimum in between LL-1 and LL-2. At E_2 the conductivity does not decrease with L, thus clearly confirming that the states remain delocalized. On the contrary, at E_1 states localize with a rapidly decreasing σ.

The main finding of the study is described in Fig. 5.24 and Fig. 5.25 and is analog to the physics already described for the divacancy model. In Figs. 5.23 (a) and (b)] a doubly peaked conductivity is observed in the lowest energy LL0, whose degeneracy is however not lifted by breaking the (defect-induced) sublattice symmetry. Similar to the divacancy case in Fig. 4.2, the conductivity scaling in Fig. 5.24(b) at the two peaks (E_2 and E_4) from Fig. 5.24(a) remains length-independent, whereas the decay of σ at energies E_1, E_3 and E_5 (where the DOS remains finite) clearly evidences the localized nature of corresponding states and formation of insulating regime. Such a feature has been linked in the divacancy case to the existence of some MIT and the formation of critical states in between which a zero-energy Hall conductivity plateau should develop [75, 143]. This is entirely different from the LL-1 discussed above.

Figure 5.25 gives the further evolution of the double-peaked conductivity $\sigma(E)$ with increasing magnetic field for 0.5% epoxy defect concentration. Figure 5.26 shows that the magnetic field dependence of the peak separation $\Delta E(B) = E_4(B) - E_2(B)$ scales almost linearly and exhibits a steeper slope for higher epoxy density. The enhancement of impurity density (to 0.95% and 1.77%) eventually drives the growth of $\Delta E(B)$ to a sublinear regime, thus offering an experimental test when measuring QHE in weakly oxidized and disordered graphene. The increase of the splitting with the magnetic field and the concentration was already rationalized in Section 4.2.4. Similar to the divacancy case, such a surprising behavior cannot be explained in terms of sublattice-symmetry breaking arguments (see Appendix D for the flawed attempt using such arguments) and demands for an alternative interpretation.

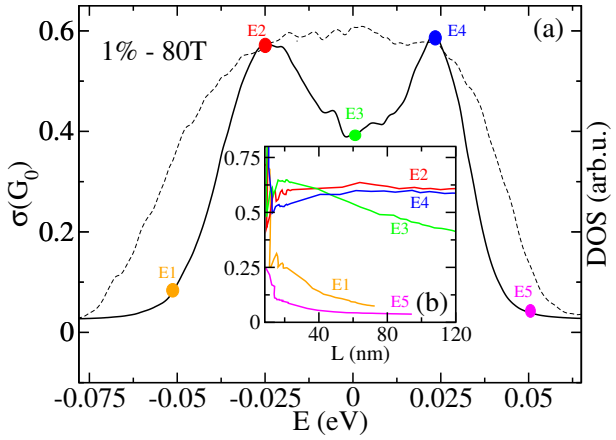

Figure 5.24: (a) Structure of the double peaked $\sigma(E)$ in units of the conductance quantum for 1% epoxy defect density (solid lines). Superimposed rescaled DOS in dotted lines. (b) Length dependent $\sigma(L)$ at the five selected energies indicated by colored points in (a).

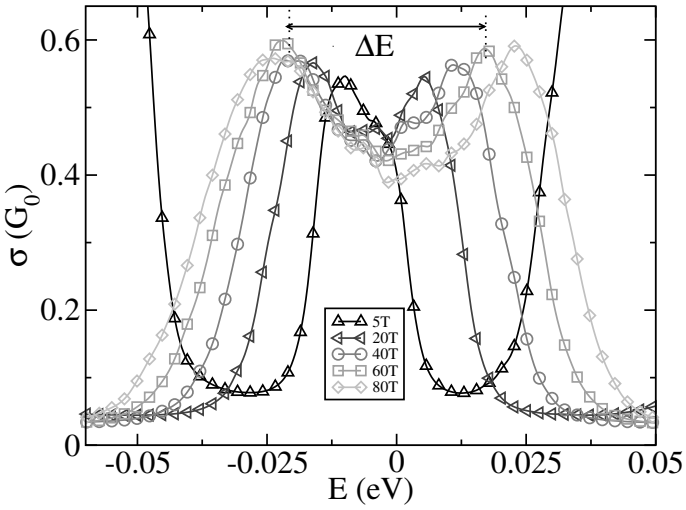

Figure 5.25: $\sigma(E)$ for 1% epoxy defects and varying the field from 5 to 80 Tesla. ΔE gives the energy separation between the maxima of delocalized peaks.

5.3.3 Origin of the Double-Peak Conductivity Structure

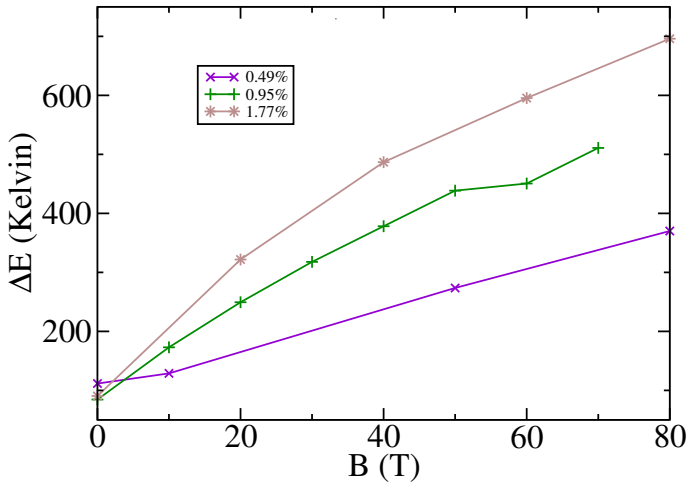

Figure 5.26: Peak separation $\Delta E(B) = E_4(B) - E_2(B)$ for different defect concentrations. Magnetic fields are increased from 0 to 80 Tesla. The non-zero value at 0 field corresponds to the dip in conductivity predicted for double impurities [144] (not visible in Fig. 5.16 because of too large energy smearing, but recalculated with smaller value here.).

Under magnetic field, the electronic structure of pristine graphene consists of well-separated degenerate flat LLs. The DOS of the lowest LL is peaked at zero energy, while the corresponding local DOS (LDOS) is spatially uniform over the system. When a single epoxy impurity is introduced, two peaks (one at negative energy and a smaller one at positive energy) appear in the LDOS close to the oxygen atom, as shown in Fig. 5.27 for different magnetic fields. This indicates the formation of two impurity-bound states. The energy separation between these two states in Fig. 5.27 increases roughly linearly with B, as observed for the two conductivity peaks of Fig. 5.25. The similar magnetic field scaling is a first indication of the importance of these single-impurity-pinned states, which are investigated in more detail below.

First, the locality of such states is analyzed. In Fig. 5.28(a), the LDOS is plotted for the carbon atoms along a line passing through one of the bridging carbon atoms at B=80 T for the two energies E_6 and E_7

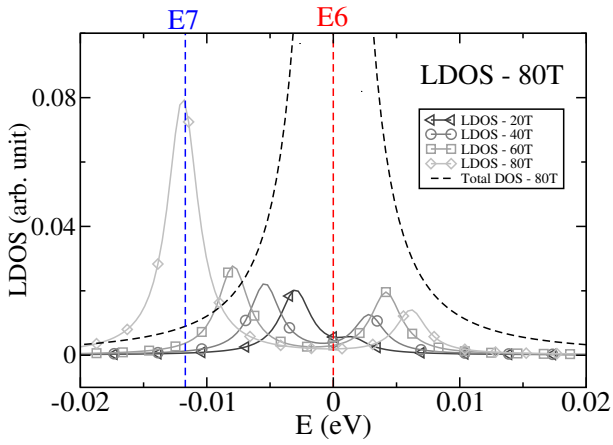

Figure 5.27: A single oxygen atom on pristine graphene sheet: total DOS and LDOS for a bridging carbon atom. Magnetic fields from 20 to 80 Tesla.

indicated in Fig. 5.27. At $E_6 = 0$, in between the two peaks, the LDOS corresponding to LL0 turns out to be suppressed over a region with a radius of about 5 nm around the defect. At the energy of the peak E_7 and in the same spatial region, the LDOS is high and decays rapidly with distance from the epoxy. This observation confirms the bound nature of the corresponding state. Additionally, the spatial extension of the bound state is driven by the magnetic field intensity and it is actually of the same order as the magnetic length ($\lambda \sim 25.7/\sqrt{B}$ nm).

The connection between the quasi-localized nature of bound states as seen in the LDOS in Fig. 5.28(a) with the formation of extended (critical) states conveying length-independent conductivity is not straightforward and even counterintuitive. To shed light on this point, it should be considered that these bound states couple to each other, even at relatively low defect density. In fact, the overlap between different bound states gives rise to new states, which spread over a certain energy window [the broad DOS feature of LL0 in Fig. 5.23(a)]. The width of this window depends on the coupling strength, which increases for higher oxygen concentration and is at the origin of the concentration dependence of the peak separation in Fig. 5.26. Together with the blue shift of the split-

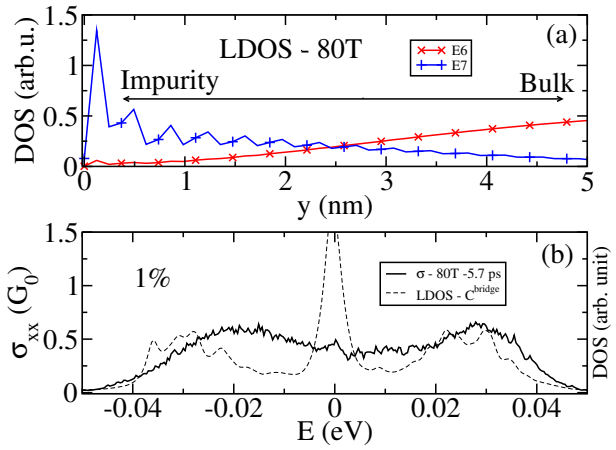

Figure 5.28: (a) Spatial dependency of LDOS by distance from the oxygen atom at $y = 0$. (b) 1% of impurities: conductivity (solid line) and rescaled LDOS calculated on one of the randomly chosen bridging carbon atoms in the sample (dashed line).

ting of states for higher magnetic fields (as seen for the isolated epoxy in Fig. 5.27), this explains the trends observed in Fig. 5.26. The apparent LL0 contribution in Fig. 5.28(b) comes from the hybrid case combining impurity contributions and pristine physics contributions (as discussed in the previous Chapter on divacancies). Taking a different randomly chosen bridging carbon atom in the 1% case could give rise to a different LDOS.

Finally the fact that, in Fig. 5.23, the conductivity of the original LL0 splits while the DOS does not, needs to be addressed beyond the mere existence of coupled bound states by discussing their conductive properties (spatial extend). This was achieved in the previous Chapter using the simplified divacancy model where an analogous linear increase of resonant-energy splitting with magnetic field was observed, possibly related to local edge states [115].

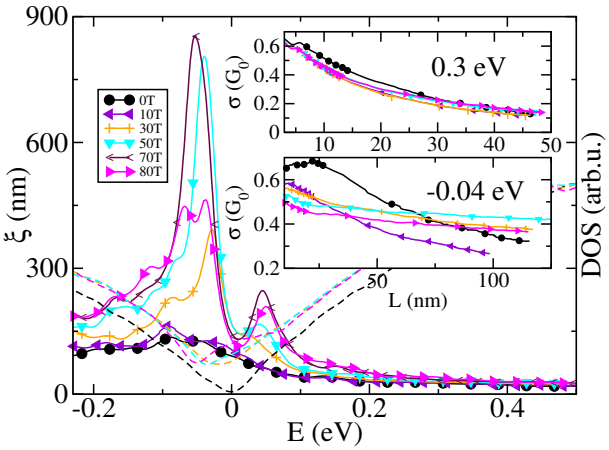

Figure 5.29: Main frame: estimated localization lengths (solid lines) at 4.4% with superimposed rescaled DOS for chosen fields (dashed lines). Inset: length-dependent conductivity scalings at chosen energies.

5.3.4 Strong Disorder Regime

Finally, the strong disorder limit for epoxy disorder is explored. In Fig. 5.29 the localization length ξ is estimated for 4.4% of disorder by fitting $\sigma(L)$ with an exponential law [79]. The scaling behaviors of $\sigma(L)$ are shown in the inset. The DOS is superimposed for 0, 30, 50 and 80 Tesla for reference. Surprisingly, for this high disorder case where the formation of a clear LL spectrum is jeopardized in the DOS [see also Fig. 5.22(c)], states are not equally (de)localized over the energy spectrum. At zero energy, localized states are located between two regions of more extended states. This is consistent with the previous analysis based on percolation of local impurity states. High magnetic fields are necessary to compensate the conventional disorder induced localization effects (lower inset), which is confirmed by the smaller localization lengths on the electronic side where disorder is stronger (main frame). Similarly, a high-B value is required to resolve the peaks of delocalized states in the spectrum. The localized states seem to be less sensitive to the effect of the magnetic field, which tunes the localization length by up to one order of magnitude in the low energy region (about 200 meV away from the zero-energy reference).

These simulations indicating robust QHE features for strong disorder might be related to the experimental observation of some QHE signatures for strong hydrogen disorder [76].

5.4 Transverse Conductivity

5.4.1 Introduction

This Section is an extension to the results obtained in previous Section 5.3 where the discussion is limited to the longitudinal conductivity. Based on the discussions and preliminary studies conducted in Section 4.3 on the transverse conductivity for divancancies, the following results on σ_{xy} for epoxy oxygen can be appreciated better. Sections 5.4.3 and 5.4.2 first focus on the physical results obtained, while Section 5.4.4 gives an indication of future calculations which might shed light on the presently very speculative interpretation of the obtained results. The convergence study on the system size is presented in Appendix G.

This Section is thus considered as a work in progress. Due to time constraints related to the computational costs of such calculations, no significant results concerning a possible zero energy Hall plateau have been obtained yet. The difficulty of developing such plateau for epoxy impurities seems twofold in comparison with the divacancy case. First, larger system sizes are required, which in present case doubles required computation times. Second, because of apparent larger coupling between impurity related delocalized states, larger magnetic fields are required to (i) either spatially better localize states around the impurity center (facilitating the appearance of mobility edges) (ii) either increase the energy splitting between delocalized states. Such increase of magnetic field in turn requires smaller time steps to correctly capture the magnetic field dependent oscillations with time of σ_{xy}. This increase of magnetic field finally might also imply the requirement of longer computational times because the smaller overlap between scattering centers reduces the effect of impurity related delocalization and increases the effect of the LL0 related to defect free zones producing the conventional QHE.

As such, this Section focuses on the comparison between the energy splitting discussed in Section 5.3 for σ_{xx} and the energy difference between the onset of conventional plateaus LL-1/LL0 and LL0/LL1 for σ_{xy}. The dip amplitude at $E = 0$ is probably related to the coupling of delocalized states, which complicates the simple interpretation in terms of impurity related LLs from the σ_{xx} study. The impurity concentration dependency of the step height between the two plateaus on the left and right of the dip is also discussed. Presently, no conclusive interpretation of this peculiar step height scaling is available.

5.4.2 Concentration Dependency

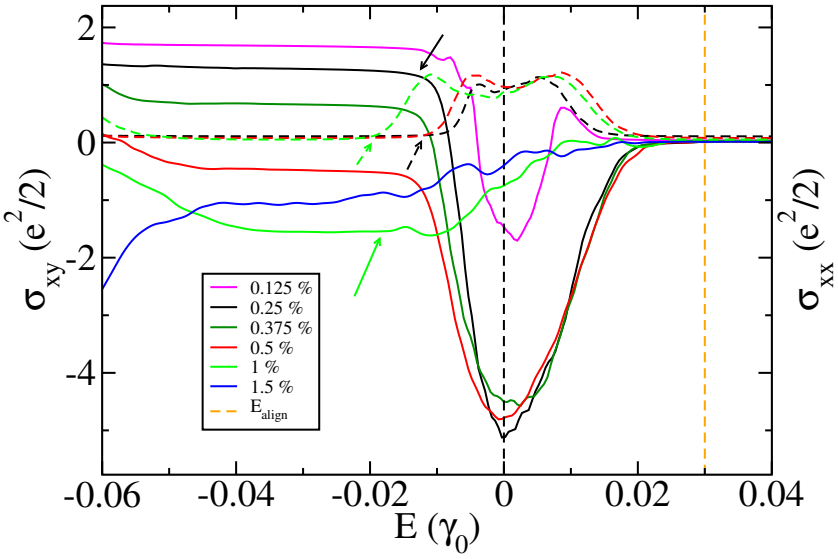

Figure 5.30: Superposition of σ_{xy} (solid lines) and σ_{xx} (dashed lines). σ_{xx} is taken at $15400\frac{\hbar}{\gamma_0}$ and σ_{xy} at $600\frac{\hbar}{\gamma_0}$. Damping factor equals 0.001. Arrows indicate onset of low energy physics for chosen concentrations. All σ_{xy} curves are shifted to have the plateau between LL0 and LL1 ($E_{\text{align}} = 0.3\gamma_0$) aligned at $0\frac{e^2}{h}$, to ease comparison.

In Fig. 5.30, the σ_{xy} and σ_{xx} are superimposed for comparison. The onset of low energy physics denoted by the colored arrows happens at the same energies for both types of conductivity. Consequently, the

energy difference between the two sets of delocalized states discussed in Section 5 is of the same order of magnitude, as expected.

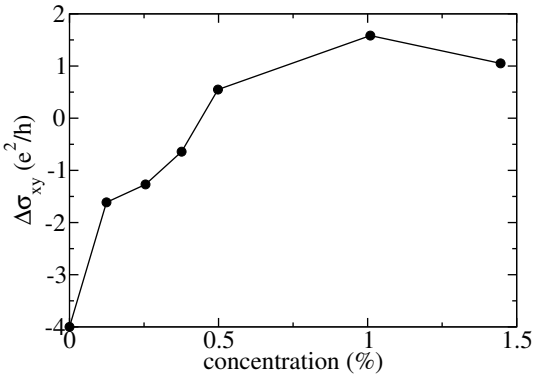

Figure 5.31: Step heights between plateau LL-1/LL0 and LL0/LL1, extracted from Fig. 5.30 (difference between σ_{xy} at -0.03 and $0.03\gamma_0$.) Quantitative step height for small impurity concentrations is less accurate because long computation times are required to correctly damp the time oscillations.

In Fig. 5.31, the step heights between plateaus LL-1/LL0 and LL0/LL1 are depicted. Practically, the difference between the transverse conductivity at -0.03 and 0.03 γ_0 is calculated. Conventional QHE theory predicts quantized values of σ_{xy} in terms of integer units of e^2/h (up to 4 if 4-fold degenerate). This was confirmed by the first calculations using the formalism on divacancies (Chapter 4) and Anderson disorder (Appendix F). Surprisingly, this is not the case here for epoxy oxygen. The value of $-4e^2/h$ for pristine graphene increases to reach a maximum around $2e^2/h$ for 1% of impurities. This increase does not happen in integer units of e^2/h. Somehow, this specific disorder causes graphene to loose its ability to fully compensate the current not carried by the localized states through fully developed delocalized states (see Section 2.2.1 for a reminder of the specific impact of disorder in the QHE). One might speculate that, because the impurity related delocalized states are not completely of the same type as conventional LL states, the coupling between states at E_+^c and E_-^c has a destructive impact on the perfect quantization of states. This absence of coupling in the divacancy case

might be explained by the simpler TB model which induces a smaller broadening of LLs. Nevertheless, at higher energy LLs, dips of conductance similar to the epoxy case are observed for the divacancy case. Such dips seem to be absent for Anderson disorder (not conclusively though). For the highest disorder concentrations, the sign of the quantization has changed altogether in comparison with pristine graphene. This suggests that the transverse conductivity sign of delocalized impurity states is opposite to the sign of the conventional QHE.

The fact plateaus are still present away from the usual LL energies might indicate the real *absence* of states instead of the *presence* of (truly) localized states. Otherwise, disorder might also destroy the perfectly flat plateaus away from the LL energies.

5.4.3 Magnetic Field Dependency

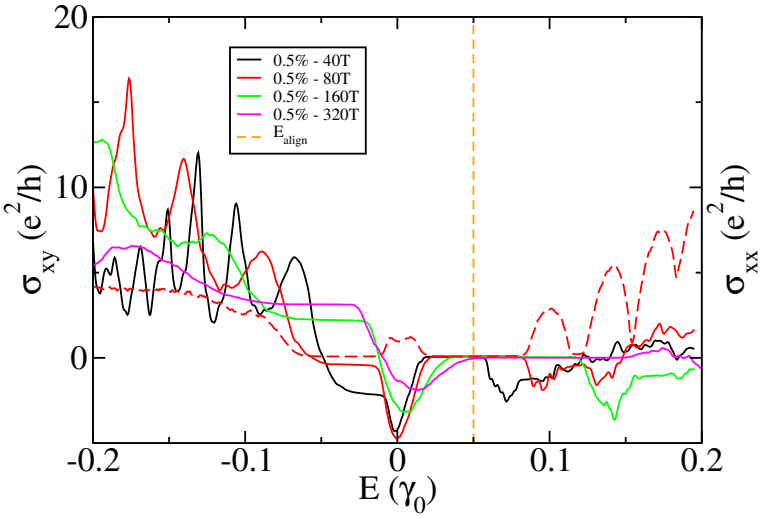

Figure 5.32: Superposition of σ_{xy} (solid lines) and σ_{xx} (dashed line). σ_{xx} is taken at $15400\frac{\hbar}{\gamma_0}$ and σ_{xy} at $600\frac{\hbar}{\gamma_0}$. Damping factor equals 0.001. All σ_{xy} curves are shifted to have the plateau between LL0 and LL1 ($E_{\text{align}} = 0.3\gamma_0$) aligned at $0\frac{e^2}{h}$, to ease comparison.

Based on the observations in the previous Section which analyzes the effect of disorder, further analysis on the effect of the magnetic field

strength might be of interest. Indeed, in Fig. 5.32, both the 160 and 320 Tesla cases seem to confirm the interpretation in terms of coupling of states. A larger magnetic field induces both a shorter magnetic length l_B and a decrase of the energy broadening around the delocalized states and thus, decreases the amplitude of the dip at $E = 0$. This is apparent from the diminishing amplitude of the dip at $E = 0$ with magnetic field for positive energies (in units of γ_0.

For higher negative energies, huge dips are observed as well, similar to the dip observed $E = 0$. Coupling between similar impurity states might be the reason for this analog behavior, as LDOS curves (not shown here) depict impurity-pinned states for *all* LLs.

5.4.4 Future Work

Further analysis on both epoxy disorder and other kinds of disorder migth help to decide whether the coupling between delocalized impurity states and associated non-integer plateau quantization is related to the specific epoxy TB Hamiltonian or to a broader class of so-called antidot scattering centers which carry currents around their inner edges in the opposite direction to usual outer edge states [113, 114, 115].

Also, by looking at the interesting hybrid case for low impurity concentrations where both the conventional LL0 and the impurity delocalized states are allowed to develop (see Section 4.3 for 0.25% and 0.5% of divacancies), a better understanding of these opposite sign physics might be acquired. Increasing the magnetic field should also help develop such hybrid case.

5.5 Conclusion

In this Chapter, a realistic disorder model is considered. The validity (including the limitations) of the TB model is discussed in detail by comparison with corresponding DFT calculations. These parameters should remain valid for a random distribution of oxygen atoms, as long as the distance between impurities exceeds a few interatomic lengths. The zero field analysis confirmed the existence of weak and even strong

localization in graphene, by inducing intervalley mixing by this type of short-range disorder. The results from Chapter 4 at finite magnetic field are extended to this more realistic model. The σ_{xx} curves also hint towards a possible observation of extended states induced by the impurities under magnetic field. Nevertheless, the σ_{xy} curves require more analysis and work to conclude about a possible existence of a new zero energy Hall plateau for this specific disorder. These last two Chapters prove that the effect of disorder on the QHE is not trivial, even for these two cases where the sublattice symmetry is preserved. In the following Chapter, the case of hydrogenation will be analyzed, which under certain conditions can break this symmetry. Only zero field calculations are considered now, but in a near future, Hall conductivity calculations might deepen the present knowledge acquired in the last two Chapters.

Chapter 6

Hydrogen

6.1 Introduction

In the previous Chapters, both the divacancy model and the epoxy oxygen model are preserving the sublattice symmetry, in the sense that both sublattices are affected equally by the impurity potential. In this Chapter, another type of impurity is considered. Hydrogen, which preferentially attaches on top of a carbon atom, adds an extra degree of freedom to the problem. Indeed, by considering different groundstates of hydrogenated graphene, the sublattices can be affected asymmetrically by the disorder. The effect of this inequivalence is not only interesting from a theoretical point of view, but the choice for hydrogen makes it also of interest because of possible intrinsic magnetismin graphene induced by these impurities.

The results discussed in this Chapter on hydrogenated graphene cover two different domains of disorder-induced transport phenomena. These domains are related to possible magneto-resistive (MR) fingerprints induced by tentative coupling of spin between hydrogen atoms (Section 6.3) and sublattice dependent conductivities related to possible magnetic ground states (Section 6.4). Calculating the theoretical MR could help clarify the controversial existence of local or coupled magnetic moments because it is an experimentally quite trivially accessible tool.

While ideal bidimensional graphene is nonmagnetic, its unidimensional derivatives (graphene nanoribbons) could exhibit magnetic ordered states due to the presence of edges [145]. Additionally, monovacancies or sp^3-type defects (such as those created by adsorbed atomic H) can introduce local sublattice imbalances in graphene, thus inducing magnetic moments [146, 147] according to Lieb's theorem [148]. Experimentally, the existence of intrinsic magnetism in graphene and graphite-based materials is strongly debated [149]. Some experimental works assume that the observed magnetic ordering is coming from graphene edges or grain boundaries, a scenario that has been recently questioned by Sepioni and coworkers who found no magnetism even for high concentration of edge defects [150]. Differently, in several recent experiments [151], signatures of room temperature ferromagnetism in graphene were tentatively related to the presence of hydrogen impurities. In all those experiments, the nature and quantity of defects remain poorly characterized and mostly uncontrolled. It would be consequently highly desirable to clarify the conditions for observing spin-dependent transport fingerprints in hydrogenated graphene.

Spin-dependent transport properties of hydrogenated graphene-based systems with realistic sizes are explored theoretically. Firstly, a spin-dependent one-orbital Hubbard Hamiltonian, describing adsorbed hydrogen impurities on a graphene sheet, is derived using first-principles calculations and solved at a mean-field level. The local spin texture around hydrogen adatoms is found to be strongly dependent on both the concentration and the specific adsorption sublattice of neighboring adatoms as previously reported [147, 152]. The self-consistent Hubbard Hamiltonian is then implemented into the transport method. The theoretical results reveal the suitable hydrogenation coverage of graphene to maximize spin-dependent conductivities, which translate into measurable magnetoresistance signals in the diffusive regime (Section 6.3).

In general, the connection between possible underlying defect-induced magnetic order in graphene and its transport signature is largely unexplored. In Section 6.4, different transport properties are found to directly depend on the nature of the underlying magnetic state of hydrogenated

graphene. Disordered anti-ferromagnetic and non-magnetic states are demonstrated to be sensitive to localization effects in the low temperature regime and high defect density, whereas a complete suppression of quantum interferences is observed in the ferromagnetic state for similar hydrogen concentrations.

Before discussing the actual physical results in Sections 6.3 and 6.4, Section 6.2 first outlines the results accompanying the extraction of the TB parameters from the Hubbard model. The Hubbard Hamiltonian in itself was obtained by Dr. D. Soriano, consequently, the methodology on that part of the work is not discussed in this Thesis.

6.2 From Hubbard to Randomly Distributed Disorder

6.2.1 Single-Orbital Mean-Field Hubbard Approximation

The single-orbital tight-binding description of graphene restricts to p_z orbitals centered on each carbon atom. The spin-related physics induced by Coulomb interaction is introduced by means of the Hubbard model in its mean-field approximation

$$\mathcal{H} = t \sum_{<\mathrm{i,j}>,\sigma} c^{\dagger}_{\mathrm{i},\sigma} c_{\mathrm{j},\sigma} + U \sum_{\mathrm{i}} n_{\mathrm{i},\uparrow}\langle n_{\mathrm{i},\downarrow}\rangle + n_{\mathrm{i},\downarrow}\langle n_{\mathrm{i},\uparrow}\rangle, \tag{6.1}$$

where t is the first-neighbors hopping term, $c^{\dagger}_{\mathrm{i},\sigma}$ ($c_{\mathrm{j},\sigma}$) is the creation (annihilation) operator in the lattice site i (j) with spin σ, U is the on-site Coulomb repulsion, and $n_{\mathrm{i},\downarrow}$, $n_{\mathrm{i},\uparrow}$ are the self-consistent occupation numbers for spin-down and spin-up electrons, respectively.

When a hydrogen (H) atom is adsorbed on top of a carbon (C) atom, the sp^2-symmetry is locally broken, and the electron from the C p_z orbital is removed from the π bands to form a σ bond with the H atom. Consequently, within the *tight-binding* approximation, such an adsorption is modeled by removing the corresponding electron and lattice site [as illustrated in Fig. 6.1 (a)]. Figure 6.1(b) and (c) present two types of the supercells ($N = 790$ atomic sites) used in periodic

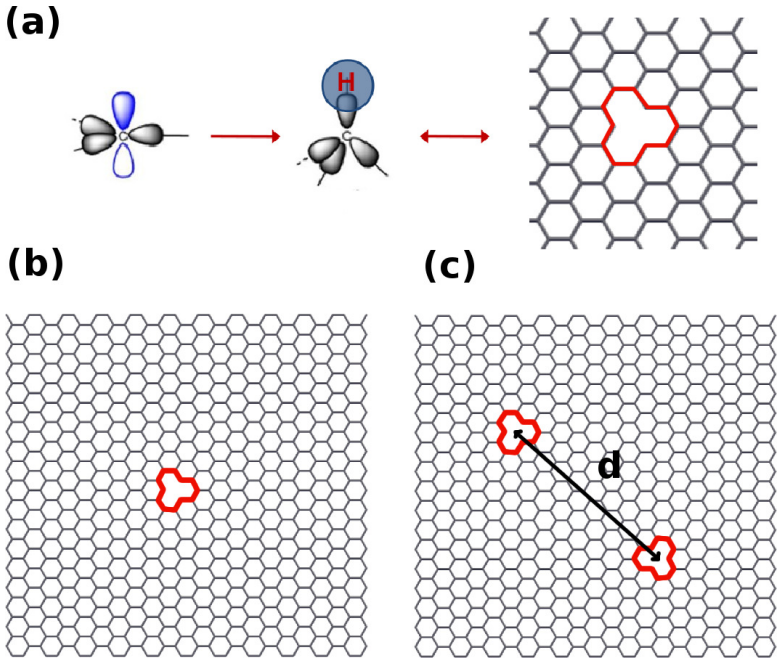

Figure 6.1: (a) Schematic representation of the sp^2 hybridization breakdown upon hydrogen adsorption. In the tight-binding model, such a defect can be mimicked by a monovacancy. (b) Single-vacancy supercell used in the mean-field Hubbard model calculations with periodic boundary conditions. (c) Supercell with two vacancies. The distance between two hydrogen defects is labeled by d.

boundary conditions calculations. In Fig. 6.2, a schematic view of the repetition of the supercells for the TB calculations is given.

6.2.2 Magnetic States

In this Section, the different possible magnetic configurations are discussed. Hydrogen defects induce zero-energy electronic states which are mainly localized around the impurity [66, 149]. When the Coulomb repulsion is switched on in the calculation, these zero-energy states spin-polarize, leading to semi-local $S = 1/2$ magnetic moments with a staggered spin density mostly located on one sublattice [146, 147, 152] [see Fig. 6.3 (a,d)]. When a finite concentration of defects is present, the

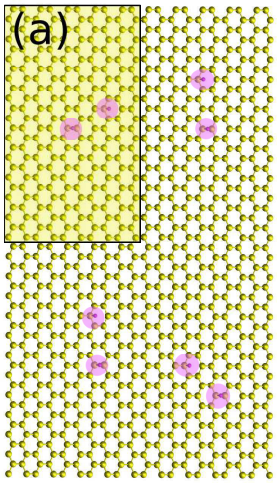

Figure 6.2: Schematic (and reduced) view of an hydrogenated magnetic graphene (the size of an original Hubbard model supercell is shaded by a yellow rectangle).

magnetic ordering between these magnetic moments is dictated by the sublattices where they are located, being co-polarized or ferromagnetic (FM) for the same sublattice and counter-polarized or antiferromagnetic (AF) otherwise [Fig. 6.3(b,e)].

The total spin S of the macroscopic ground state is given by the excess of magnetic moments on one specific sublattice, although $S = 0$ is the most likely value on simple statistical grounds (equal H occupation of both sublattices). S is obtained by the straightforward application of Lieb's theorem [148] which relates the total spin of a bipartite lattice to the difference between sublattice sites ($2S = N_A - N_B$). As $N_A - N_B = 0$ for the AB case, Lieb's theorem predicts either a non-magnetic (NM) or an antiferromagnetic ground state ($AF - AB$ from hereon), both with $S = 0$. To explore the effect of varying the hydrogen concentration, different supercell sizes are investigated (see insets in Fig. 6.3 and Fig. 6.4). The distance between hydrogen atoms was decreased while reducing the supercell size. In the following two sections, different systems are considered to calculate either an MR signal either sublattice dependent transport phenomena.

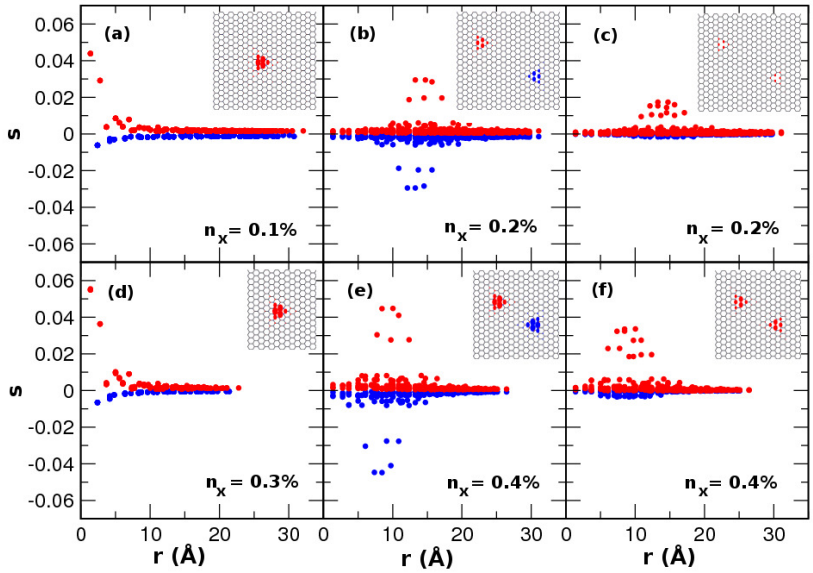

Figure 6.3: Local (site) spin (s) versus r (the distance to the center of the supercell) for various vacancy concentrations: (a,d) $n_x = 0.1\%$ and 0.3% in the paramagnetic case, (b,e) $n_x = 0.2\%$ ($d = 27.7$ Å) and 0.4% ($d = 18.1$ Å) in an antiferromagnetic state, and (c,f) in a ferromagnetic excited state within the mean-field Hubbard approximation [$\uparrow$ (red) and $\downarrow$ (blue) electrons]. In all cases, the center of mass of the vacancies is at $r = 0$.

Systems for MR Signal Calculation

To calculate a possible MR signal, two assumptions related to the macroscopic magnetic states are considered. The first one is the simplest: a *paramagnetic* (PM) state, which is a good approximation for sufficiently low H concentrations, or at sufficiently high temperatures, in which there is no correlation between the semi-local moments. This state is thus constructed from independent large supercells containing a single vacancy as shown in Fig. 6.1 (b). The corresponding spin densities on each cell site are represented in Fig. 6.3(a,d) as a function of the distance to the center of the supercell for two different concentrations of defects. The result favorably compares with first principles calculations when $U/t = 1$ [153].

The second assumption is more complex since pairwise magnetic ordered states are investigated. The latter are constructed using supercells containing two vacancies on different sublattices [see Fig. 6.1 (c)] far from the edges. When selecting one site on each sublattice [see Fig. 6.1(b,e)], the magnetic moments couple antiferromagnetically and the macroscopic state generated by merging several supercells is an antiferromagnet (AF) with zero total spin ($S = 0$). The effect of the distance (d) between vacancies while varying accordingly the supercell size is explored. By changing simultaneously the distance and size, a meaningful definition for the concentration n_x based on only two vacancies per cell is allowed. For $n_x = 0.6\%$ ($d = 8.5$ Å) the vacancies become very close to each other, thus allowing overlapping between magnetic moments and suppression of the local antiferromagnetic state [147]. When the vacancies are in the same sublattice, the ground state is ferromagnetic (FM).

The AF ordering can be further tuned by applying a sufficiently large external magnetic field, parallel to the graphene sample. A perpendicular field would induce Landau quantization. First-principles calculations performed with the SIESTA code [154], for the unit cell shown in Fig. 6.3(b), reveal that the energy difference between the antiferromagnetic and ferromagnetic configurations is about 1 meV, yielding a rough value of ten Tesla for the corresponding switching magnetic field (smaller values are expected for smaller H concentrations). Such measurement would have to be performed at temperatures below 12 K, to avoid temperature-triggered switching of states. Similar values were predicted for hydrogenated graphene nanoribbons although with larger interdistance between H adatoms [152] and also for mono-vacancies in carbon nanotubes [155]. When applying the magnetic field, the local magnetic moments become co-polarized giving rise to a FM state. The difference in the magnetic ordering can affect the conductivity and induce a MR response as discussed for graphene nanoribbons in Ref. [152]. To study the possible magnetoresistance signals in hydrogenated graphene samples, the spin density and related spin-dependent on-site energies are computed for this specific case [Fig. 6.3(c,f)].

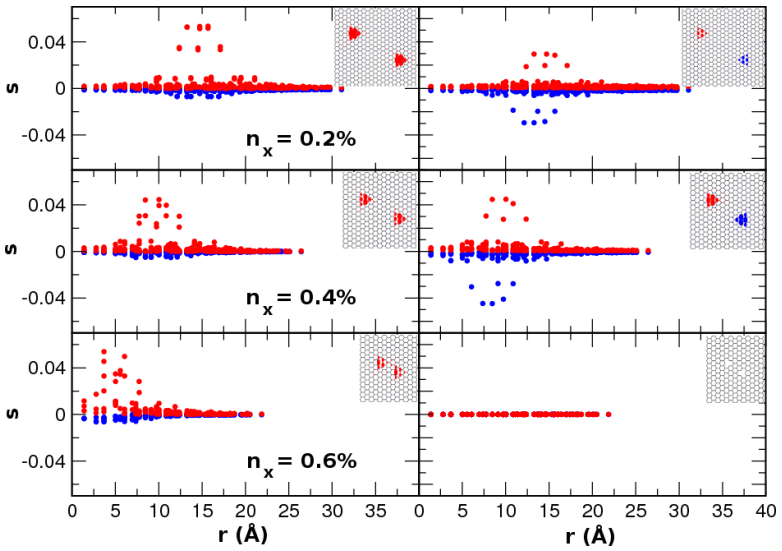

Figure 6.4: Local spin (s) versus the distance to the center of the supercell (r) for vacancy (or hydrogen) concentrations $n_x = 0.2, 0.4\%$ and 0.6% in the ferromagnetic (left panel) and antiferromagnetic (right panel) cases. Red (blue) dots correspond to spin up (down) electrons. Insets: Top-view projections of the local spin densities.

Systems for Sublattice Dependent Transport

In addition to the AF case presented in Section 6.2.2, the *groundstate* ferromagnetic case (F-AA) is considered as well [different from the F case (F-AB) induced from the AF-AB case by an external magnetic field].

This ferromagnetic ground state is induced by Lieb's theorem which predicts $S \neq 0$ when the two sublattices present an uncompensated hydrogenation. Zhou *et al.* [156] suggested a semiconducting graphene with one sublattice fully hydrogenated (also known as *graphone*). Although the selective hydrogenation of the A (or B) sublattice of a graphene sample is a challenging task, disorder-driven hydrogenation such as ripples in suspended graphene or surface effects in deposited samples could give rise to slightly uncompensated lattices, favoring a ferromagnetic ground state. Sublattice dependent doping of graphene has been observed in the case of nitrogen [157] which was studied later on from a theoretical point of view [158]. This latter theoretical study confirms several of the sublat-

tice dependent transport phenomena discussed in Section 6.4. To explore possible intrinsic ferromagnetic transport responses, the case of totally uncompensated functionalization (AA or BB) is therefore investigated theoretically, where both chemisorbed hydrogen atoms lie on the same sublattice in the supercell (referred as $F-AA$ hereon). Figure 6.4 illustrates the local spin density for the situation of antiferromagnetic (right panel) and ferromagnetic (left panel) couplings with various hydrogen concentrations. An important observation is the disappearance of the spin density for the $AF-AB$ case for hydrogen densities $n_x \geq 0.6\%$ which contrasts to the robustness of the intrinsic ferromagnetic case.

6.2.3 Kubo Conductivity Methodology

Using the self-consistent Hubbard Hamiltonian calculations, spin-dependent on-site energies are estimated for each supercell. The graphene samples are constructed by attaching a large number of these supercells following different random arrangements (see Fig. 6.2). Using the spin-dependent onsite energies, the same Kubo formalism from Section 3.2 is then used to extract meaningful conductivities and transport length scales such as the mean free path.

The spin-dependent Kubo conductivity (at zero temperature and zero frequency) reads

$$\sigma_{\uparrow,\downarrow}(E,t) = (e^2/2)\mathrm{Tr}[\delta_{\uparrow,\downarrow}(E-\hat{H})]D_{\uparrow,\downarrow}(E,t) \tag{6.2}$$

with

$$\mathrm{Tr}[\delta_{\uparrow,\downarrow}(E-\hat{H})/S] \tag{6.3}$$

the spin-dependent densities of states per surface unit at Fermi energy E. At a fixed energy, $\sigma_{\uparrow,\downarrow}(E,t)$ reach their maximal values at the same time as $D_{\uparrow,\downarrow}(E,t)$ ($D^{\max}_{\uparrow,\downarrow}$) allowing the estimation of the spin-dependent Kubo conductivities

$$\sigma_{\uparrow,\downarrow}(E) = (e^2/2)\mathrm{Tr}[\delta_{\uparrow,\downarrow}(E-\hat{H})]D^{\max}_{\uparrow,\downarrow}(E), \tag{6.4}$$

that account for the disorder effects on the density of states. The maximum value $D^{\max}_{\uparrow,\downarrow}(E)$ of the diffusion coefficient also gives a numerical value to the elastic mean free path, since $\ell_e = D^{\max}/v_F$ (where $v_F = 10^6 \mathrm{ms}^{-1}$).

6.3 Magneto-Resistive Fingerprints

6.3.1 Introduction

As long as $n_x \leq 0.5\%$ the diffusion coefficients are found to reach a saturation regime after a few thousands of femtoseconds, and then remain roughly constant up to very long times, indicating a diffusive regime and a negligible contribution of quantum interferences within the computational reach. The maximum value allows the evaluation of $\ell_e = D^{\max}/v_F$, with $v_F = 10^6 \mathrm{ms}^{-1}$. Note that the transport properties are calculated in the zero temperature limit, which should however be robust to higher temperatures given the weak electron-phonon coupling in graphene.

6.3.2 Spin-Dependent Transport Features

Figure 6.5 presents the Kubo conductivities for the AF (left panel), FM cases (right panel) and the PM case (inset in right panel) for H concentrations varying from 0.1% up to 0.5%. As expected, both in the AF and the PM case, no spin-dependent transport features are observed in the results, with the conductivities for up and down spins being equal within the statistical error. Some differences in the shape of the conductivity curves versus energy close to the Dirac point between the PM and AF cases are observed. In sharp contrast, in the FM case, the spin-dependent conductivities significantly differ away from the charge neutrality point. $\sigma_{\uparrow,\downarrow}(E)$ decays roughly linearly with n_x for the lowest H density (which is a trend general for resonant scattering [159]), but one clearly observes a tendency towards saturation at higher concentration. It is worth mentioning that, in all cases, the total Kubo conductivities ($\sigma_\uparrow(E) + \sigma_\downarrow(E)$) remain larger than $2G_0/\pi = 4e^2/\pi h$, which is

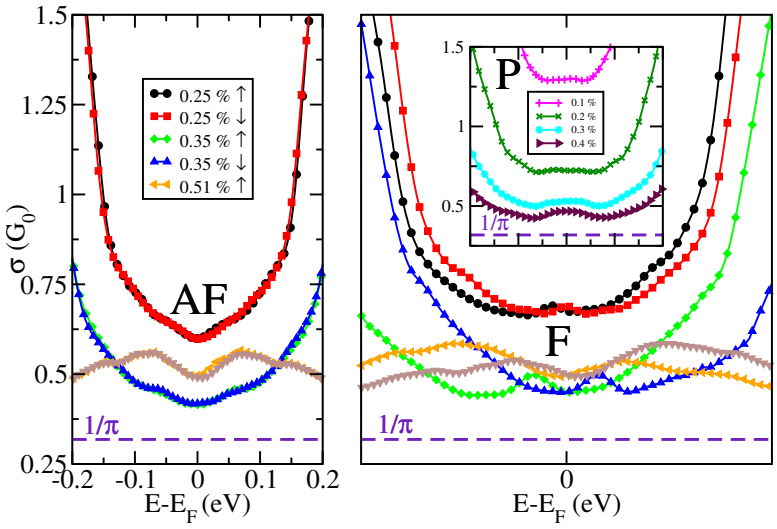

Figure 6.5: Left panel : Conductivities of hydrogenated graphene samples with various concentrations for the antiferromagnetic case (left panel), paramagnetic case (right panel inset) and ferromagnetic case (right panel main frame). Horizontal dashed lines give $2e^2/\pi h$.

the theoretical minimum value estimated within the self-consistent Born approximation [160].

6.3.3 MR Signature

From the computed conductivities in the AF and FM cases, one extracts (for AB-sublattice preserved symmetry), the magnetoresistance

$$\mathrm{MR} = (\sigma^F - \sigma^{AF})/(\sigma^F + \sigma^{AF}) \tag{6.5}$$

with $\sigma^F = \sigma^F_\uparrow + \sigma^F_\downarrow$ and $\sigma^{AF} = \sigma^{AF}_\uparrow + \sigma^{AF}_\downarrow$. Figure 6.6 shows MR for three different H concentrations. The maximum signal is observed for the lowest density $n_x = 0.25\%$ and reaches about 7% for a switch from the antiferromagnetic to the excited ferromagnetic case. The signal is reduced with increasing n_x and tends to disappear at higher concentrations, along with the spin density. One also notes that, since the macroscopic states are built out of supercells carrying only two vacancies, the

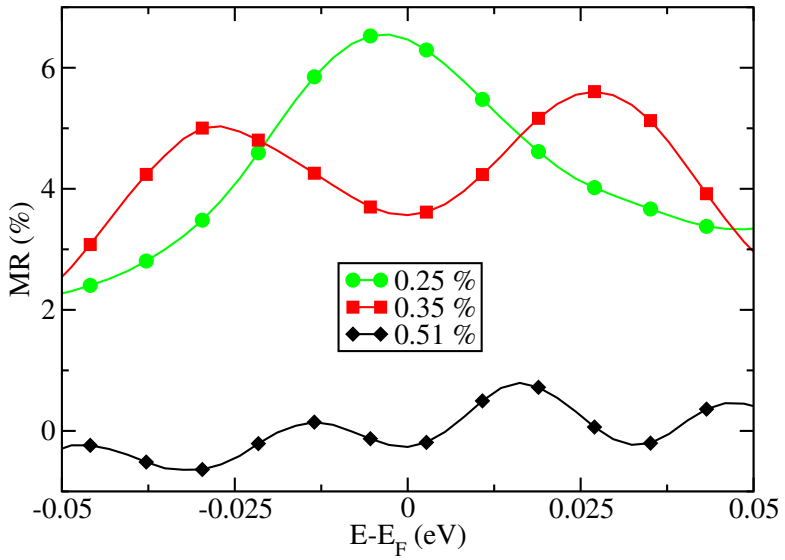

Figure 6.6: Magnetoresistance of hydrogenated graphene samples with concentrations of $n_x = 0.25, 0.35, 0.5\%$ as a function of charge energy.

number of magnetic correlations is likely underestimated. Hence, experimental observations of larger MR values would not be a surprise. Some asymmetry in the MR profiles (Fig. 6.6) is observed, which roots in small numerical inaccuracies stemming from both, the approximated parameters taken from the Hubbard Hamiltonian and the use of a random phase approximation for the Kubo methodology.

6.4 Sublattice Dependent Conductivity

6.4.1 Introduction

Focusing now on the typical transport signatures for the two different magnetic ground states, Section 6.4.2 covers the $AF - AB$ case and Section 6.4.3 covers the $F - AA$ case.

6.4.2 Sublattice Independent Distribution

For low hydrogen concentrations ($n_x < 0.6\%$), where local spin densities survive even for the $AF - AB$, no significant spin-dependent transport

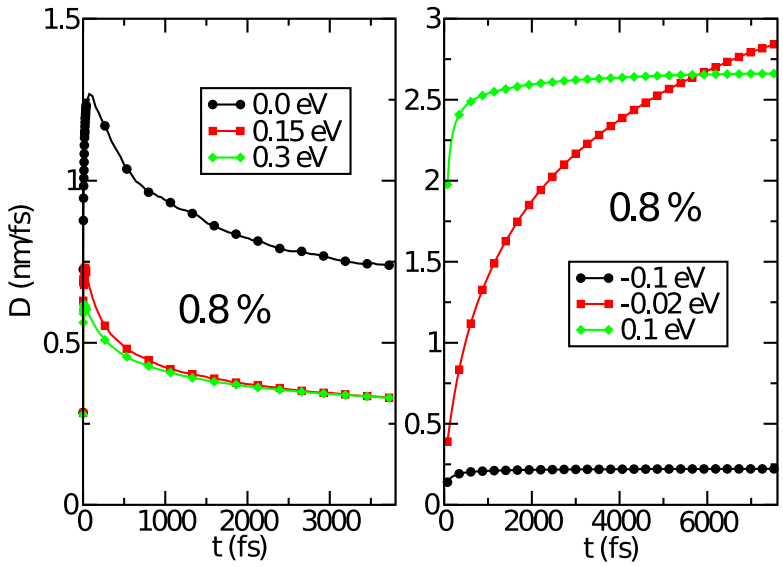

Figure 6.7: Time-dependent diffusion coefficients for three selected energies (see legends) for a $n_x = 0.8\%$ hydrogen impurity concentration, in the NM (left panel) and $F - AA$ (right panel) configurations.

features are observed. Focus is shifted towards the higher concentration limit ($n_x = 0.8\%$) in which the local spin has been supressed yielding a global non-magnetic state. Figure 6.7 (left frame) presents $D_\uparrow(E,t)$ for $n_x = 0.8\%$ at three selected energies. These diffusion coefficients are clearly reaching a saturation regime after a few hundreds of femtoseconds. Then, they exhibit a strong logarithmic decay which is an unambiguous fingerprint of weak localization effects. The behavior of the corresponding elastic mean free path ℓ_e is illustrated in Fig. 6.8 (inset). Away from the Dirac point, $\ell_e \sim 1/n_x$ as expected from a simple Fermi Golden rule. At lower energies, ℓ_e fluctuates within $1 - 2$nm, presenting a weak hydrogen-concentration dependence.

Figure 6.8 (main frame) displays Kubo conductivities at different times. The latter are evaluated at larger elapsed times when quantum interferences cannot be neglected. Note that the total semiclassical conductivity always remains higher than $2G_0/\pi = 4e^2/\pi h$ (G_0 the conductance quantum) in full agreement with the analytical results derived from the self-consistent Born approximation [160]. The exper-

imental increase of the conductivity at the Dirac point with respect to the clean limit value $2G_0/\pi$ has also been theoretically established for Dirac (single-valley) electrons and many types of disorder, being actually observed in most graphene samples [161]. This can be explained by intra-valley scattering (dominant over inter-valley one) which is induced either by intrinsic (ripples) or extrinsic disorder (charged impurities) always accidentally present in most samples [162]. On the contrary, as soon as quantum interferences come into play in the intentionally disordered systems, $\sigma_{\uparrow,\downarrow}(E,t)$ becomes lower than its semi-classical limit, pinpointing the transition to a weak localization regime, as illustrated in Fig. 6.8 (main frame) for two elapsed times $t = 250$fs and $t = 2000$fs. From the computed electronic mean free path ℓ_e, the corresponding localization length can be estimated using the relationship $\xi(E) = \ell_e \exp(\pi\sigma/2G_0)$ [139]. Close to the charge neutrality point, localization lengths are predicted to be in the range of $\sim 8 - 15$nm for defect densities between 0.25% and 0.8%. Note that this transition to a weak localization regime has been overlooked in recent works where similar models predict conductivity values well above $4e^2/\pi h$ [159] at the Dirac point. This result is, in addition, consistent with experimental findings.

6.4.3 Sublattice Dependent Distribution

Fig. 6.7 (right frame) presents $D_\uparrow(E,t)$ for the $F - AA$ case. Conversely to the NM case, for identical defect densities, the establishment of a diffusive regime at much longer times pinpoints a much weaker effect from backscattering. Additionally, the saturation of $D_\uparrow(E,t)$ to its maximum value is not observed to be followed by a logarithmic decay as expected in presence of weak localization effects. Fig. 6.9 presents the Kubo conductivities for the intrinsic ferromagnetic situation $F - AA$ computed at $t = 7600$fs. First, in sharp contrast to the non-magnetic case, a strong spin-splitting is observed around the charge neutrality point (right inset), as manifested by the two separated (resonant) peaks for up $[\sigma_\uparrow(E)]$ and down spin $[\sigma_\downarrow(E)]$ populations, occurring respectively at energies $\varepsilon^r_\uparrow \simeq -15$meV ($\varepsilon^r_\downarrow \simeq +15$meV). The spin gap $\Delta_{sg} = |\varepsilon^r_\uparrow - \varepsilon^r_\downarrow|$

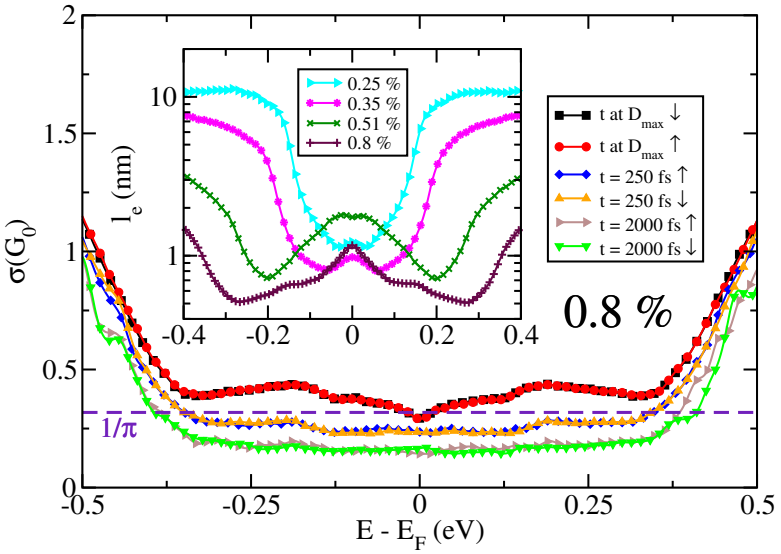

Figure 6.8: Main frame: Kubo conductivities for the NM magnetic state with $n_x = 0.8\%$ hydrogen impurities. The values at $D^{\max}$ (extracted at $t \sim 50$fs) gives access to the Kubo conductivity, whereas values at longer elapsed times clearly encompass localization effects. The theoretical limit for Kubo conductivity per spin channel ($2e^2/h\pi$) is represented by the horizontal dashed line. Inset: Spin-degenerate elastic mean free path for various hydrogen concentrations.

ranges within $[25, 30]$meV for $n_x = 0.25 - 0.8\%$ (see Fig. 6.9-right inset) and originates from the strong local Coulomb interaction between the two spin-polarized states near the impurities. On the other hand, the total conductivity is found to decay with hydrogen concentration but saturates at $4e^2/\pi h$ for energies away from the resonant peaks. Such a saturation is concomitant to the robust diffusive regime established after an initial ballistic extension of the wavepackets, but unaffected by further quantum interferences (as calculated for three energies in Fig. 6.7). In Fig. 6.9-left inset, $\sigma_\uparrow(E,t)$ for $n_x \simeq 0.5\%$ is depicted for increasing elapsed times (similar trend is found for $n_x \simeq 0.8\%$). Surprisingly, in the vicinity of $\varepsilon^r_{\downarrow,\uparrow}$, the conductivities are seen to increase with time without saturation (up to the computational limits). This behavior is not a numerical artifact, but rather illustrates the absence of backscattering, manifesting a robust quasi-ballistic regime.

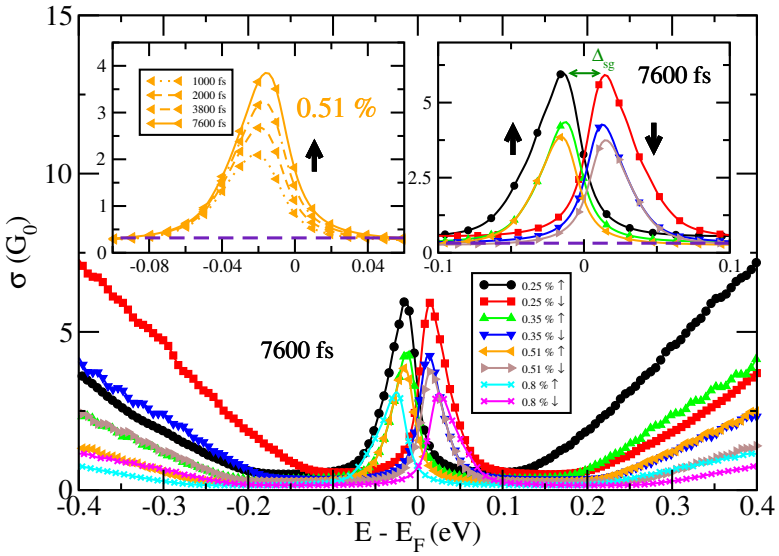

Figure 6.9: Main frame: Kubo conductivities for the $F-AA$ magnetic state for up and down spin configurations, for an elapsed time of $t = 7600$fs. Left inset: time-dependent evolution of $\sigma_{\uparrow}(E)$ close to the resonance energy $\varepsilon^{r}_{\uparrow} \sim -15$meV. Right inset: zoom in on the spin-split gap Δ_{sg}. Horizontal dashed lines give $2e^2/\pi h$.

The comparison between the NM and $F-AA$ cases for the same hydrogen concentration is therefore particularly striking. The considerable reduction of backscattering and of quantum interferences for the $F-AA$ case obviously stems from the particular symmetry of the functionalized system (exclusive chemisorption of hydrogen on A lattice sites). The robustness of transport in such a situation is also likely related to pseudospin effects which trigger Klein tunneling and weak antilocalization phenomena [40, 163]. Additionally, this specific asymmetry resulting in full imbalance between functionalized A sites and defect free B sites, also roots the establishment of strong ferromagnetism. In brief, one of the most interesting findings is thus the connection between ferromagnetic order and absence of localization effects.

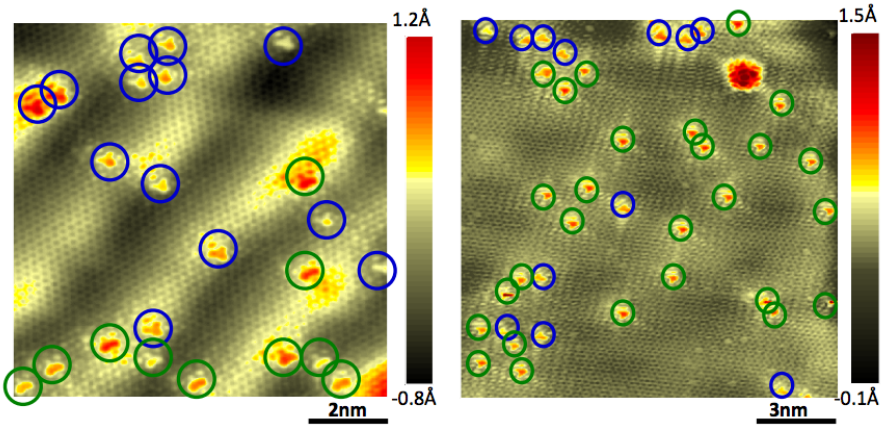

Figure 6.10: Sublattice dependent doping of graphene by nitrogen. Circles indicate zones of preferential sublattice doping. Figure taken from the supplemental material of [16].

6.4.4 Experiment

Recently, reseachers at Columbia University showed that sublattice dependent doping is feasible. As illustration, a figure from their paper is presented here (see Fig. 6.10). Additional work is still required to explain the chemical mechanism leading to this result.

6.5 Conclusion

In conclusion, in addition to the model of extrinsic activation of the magnetic coupling through a magnetic field, yielding MR fingerprints (a few percent should already be accessible by experiment), intrinsic ordered magnetic states are demonstrated to exhibit a very specific transport signature in large-size hydrogenated graphene in the low temperature limit. An intrinsic ferromagnetic state will take place in case of exclusive functionalization of one out of the two sublattices. In this situation, the material would be strongly (anomalously) robust to localization phenomena (up to hydrogen densities $n_x \leq 1\%$), either presenting a saturation of the low-temperature conductivity to its Kubo value, or a quasiballistic motion at some resonant energies. In striking contrast, for similar

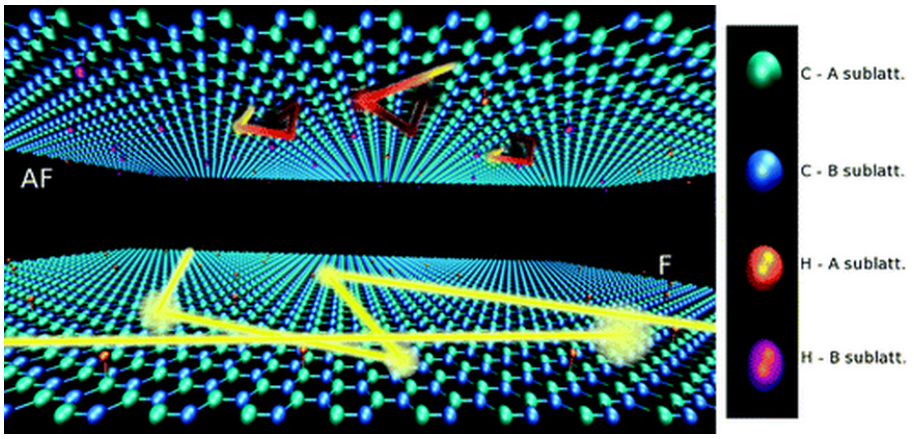

Figure 6.11: Artistic view of localized (up) and quasi-balistic states (bottow) in hydrogenated graphene

defect densities, a disorder antiferromagnetic and a non-magnetic state will suffer from quantum interferences (beyond the diffusive regime) and localization effects will manifest in the low temperature regime, for instance through a variable range hopping behavior (as also observed in other types of damaged graphene). These theoretical predictions provide a possible guidance for further experimental transport measurements and scrutiny of magnetism in hydrogenated graphene. One finally remarks that other types of functionnalization (such as adsorbed NO_2 gases or fluorination) could provide alternative routes to induce strong spin-polarized impurity states and high temperature magnetic order in graphene [78, 164].

From a more general point of view, this Chapter shows that the sublattice symmetry plays an important role in the transport properties of graphene. Breaking this symmetry locally and/or globally is shown to activate new physics unobserved for epoxy disorder. In the following Chapter, an overview of the different types of functionalization physics is put into perspective using the framework of short and long range disorder.

Chapter 7

Long range *vs* short range disorder

7.1 Introduction

This Chapter present an overview of the different disorder induced phenomena encountered in the previous Chapters. They are put into perspective of what is already known from litterature regarding the convenient separation between long and short range scatterers.

The nature and impact of disorder in graphene has been a long debated issue. Firstly, because of the different fabrication techniques to obtain graphene inducing either local or more long range lattice imperfections (defects, impurities, ripples and long range strain deformations,...) and secondly, because of the possibility to observe unique transport features such as Klein tunneling, electron collimation or weak antilocalization phenomena.

Klein tunneling in graphene [40] is a spectacular manifestation of the Dirac fermions physics where backward reflection is partially or totally suppressed (depending on the incident angle of the incoming wavepacket and the heigth and width of the barrier) when charge crosses a tunneling barrier. This result contrasts with usual behavior in Schrödinger physics for which the quantum wavepackets are exponentially damped when crossing a barrier of increasing width. Klein tunneling is thus

an efficient mechanism to suppress localization effects provided the impurity potential is sufficiently long range to prohibit intervalley scattering between the two inequivalent Dirac cones, and therefore allows only intravalley-mediated scattering trajectories. It roots in the approximately symmetric electron-hole electronic band structure and the pseudospin degree of freedom associated to the AB sublattice degeneracy. Note that a similar mechanism has been previously well documented in metallic carbon nanotubes [160, 165, 166, 167] where total suppression of backscattering appears in this one-dimensional case.

Pseudospin shares similar symmetries with the spin degree of freedom, and as such, the corresponding wavefunctions acquires an extra phase factor (Berry phase) which can provoke destructive interferences under certain circumstances. The observation of the weak antilocalization (WAL) in graphene [168, 169] is such a manifestation of pseudospin effects on phase interferences. WAL in graphene has been rigorously worked out by McCann and coworkers [170], who provide a solid theoretical foundation of a constructive interferences effect between diffusive states propagating clockwise and anticlockwise along a trajectory back to some origin, and monitored by pseudospin-related phase factors. Again, the nature of disorder and contribution of intravalley versus intervalley scattering events is key in understanding crossover regimes between WL and WAL regimes. The possibility of strong (Anderson) localization is also inherent to the nature of disorder, and is expected to follow continuously the weak localization corrections, as dictated by the scaling theory of localization [139].

It is therefore important to clarify the contribution of different possible sources of disorder in graphene and their impact on transport properties. Hereafter, various cases from more academic (but generic) scattering potential such as the Anderson disorder, to long range scatterers (mimicking charged impurities), and to more invasive chemical defects such as adsorbed oxygen and hydrogen atoms (as introduced in Chapter 6 and Chapter 5) are considered. The Anderson and long range scattering calculations are not an actual part of this Thesis, but by

including them here, a more complete and comprehensive picture of transport phenomena in disordered graphene emerges.

7.2 Short range scattering

The case of a generic model for short range scattering potential, namely the Anderson disorder, is firstly considered. This white noise uncorrelated disorder is introduced through modulations of the onsite energies of a π-orbital tight-binding Hamiltonian ($\varepsilon_\pi = \varepsilon_\pi + \delta\varepsilon_\pi$). The disorder strength is tuned by choosing randomly $\delta_{\varepsilon_\pi} \in [-W/2, W/2]\gamma_0$ energy perturbations with $\gamma_0 = -2.7eV$ the hopping term between nearest neighbor π-orbitals. This disorder could in principle mimic neutral impurities such as structural defects, dislocation lines, or ad-atoms, although the local geometry and chemical reactivity of defects and impurities actually demand for more sophisticated *ab initio* calculations if aiming at quantitative predictions (see Refs .[98, 123, 129, 171] as illustrations). An interesting aspect of this model is however that numerical simulations can be contrasted to analytical results derived in the Self-Consistent Born Approximation (SCBA) [132, 133]. Indeed, within SCBA, the semiclassical part of the conductivity (that is neglecting all interferences effects driven by Cooperon contributions) due to short range disorder is derived as [133]

$$\sigma_{sc}(E) = \frac{1}{2}\frac{e^2}{\pi^2\hbar}\left[\left(\frac{E-\Delta(E)}{\Gamma(E)} + \frac{\Gamma(E)}{E-\Delta(E)}\right)\arctan\frac{E-\Delta(E)}{\Gamma(E)} + 1\right]$$

with $\Delta(E) = \mathrm{Re}\Sigma(E)$ and $\Gamma(E) = \mathrm{Im}\Sigma(E)$ derived from the self energy which satisfies the self-consistent energy equation

$$\Sigma(E+i\eta) = \frac{n_i u^2}{2\pi}(E - \Sigma(E+i\eta))\int_0^{k_c}\frac{kdk}{(E-\Sigma(E+i\eta))^2 - (\gamma k)^2}$$

with n_i the defect density, u^2 the average squared disorder strength (a mapping of this model to the Anderson disorder is possible by adjusting

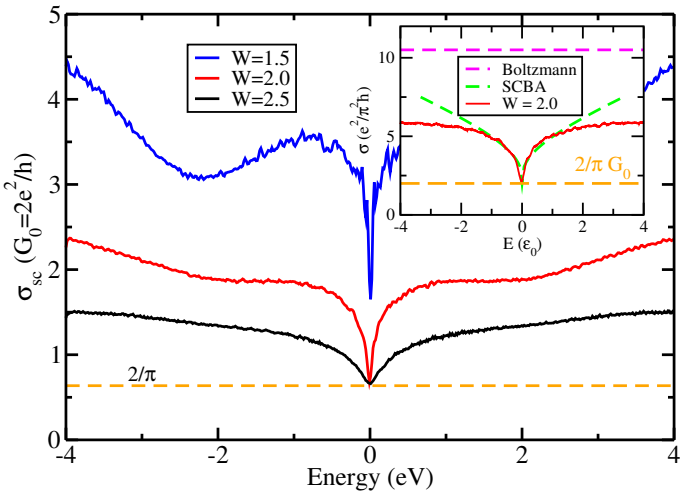

Figure 7.1: (color online) Main Frame: Energy-dependent semiclassical conductivity for Anderson disorder strengths of $W = 1.5$, 2.0, and 2.5. The dashed line denotes the minimum value of $\sigma_{sc} = 4e^2/\pi h$. Inset: Comparison with Self-Consistent Born Approximation with fitting factor A=21 for W=2.

parameters to obtain same average values and variances, i.e. $n_i(1 - n_i)|u| = W/\sqrt{12}$) and $k_c = \gamma_0/\epsilon_0$ the cut-off where $\epsilon_c = 50\epsilon_0$ in the simulations [160, 165, 166, 167]. ϵ_0 is an arbitrary energy scale which is assumed to have the same order of magnitude as relevant energies such as E, Δ and Γ in the SCBA [133].

In addition to a specific energy dependence of $\sigma_{sc}(E)$, the value at the Dirac point $\sigma_{sc} = 4e^2/\pi h$ appears as a fundamental minimum limit. Using the Kubo method, σ_{sc} for various values of W are obtained as shown in Fig. 7.1. The agreement with SCBA results is highly convincing. For W=2, the dimensionless parameter $A = \frac{4\pi\gamma_0}{n_i u^2}$, characterizing the scattering strength, is set to 21 to obtain a convincing fit for energies up to $2\epsilon_0$ with $\epsilon_0 = 0.3$ eV. For higher energies, the agreement with SCBA falls short due to higher order deviations. Also, for such disorder the SCBA is not sufficient as all symmetries are broken and the system is driven from a weak to strong localization regime as dictated by the scaling theory of localization in two-dimensional systems [139, 172].

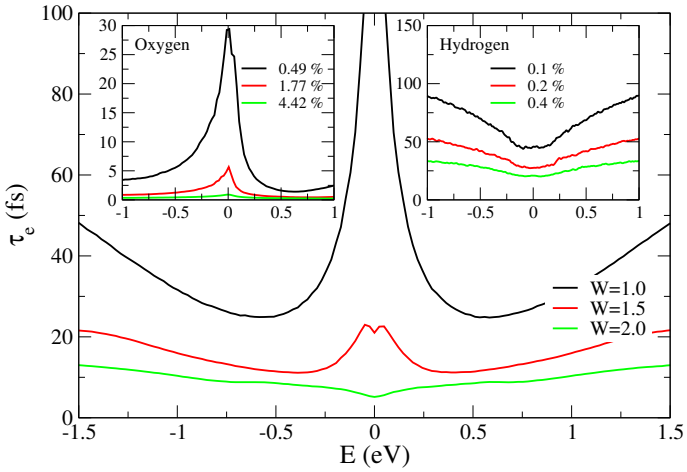

Figure 7.2: (color online) Elastic scattering time versus energy (τ_e) for three different strengths of W for the disorder potential ($W = 1.0$, 1.5, and 2.0). Left inset: τ_e for various densities of epoxide defects (adsorbed oxygen). Right inset: τ_e for various densities of hydrogen defects (sp^3 defects).

7.3 Long range scattering

To explore the possibility of crossovers between a weak localization to a weak antilocalization regime, a different disorder model is adopted, which describes a certain density of Coulomb impurities defined by a long range scattering potential [173, 174]. The contributions from N_I impurities randomly distributed at position $\mathbf{r}_i$ (among N sites of the system) is given by renormalized onsite energies at orbital α with $\varepsilon_\alpha = \sum_{i=1}^{N_I} \varepsilon_i \exp(-|\mathbf{r}_\alpha - \mathbf{r}_i|^2/(2\xi^2))$, where ξ defines the effective range, and ε_i are chosen at random within $[-W/2, W/2]$ γ_0, where W gives the strength of the local potential profile. Different random configurations of graphene samples with same size, ξ, W, and $n_i = N_i/N$ provide a statistical ensemble for a given disorder strength. The impurity effective range $\xi = 3a = 0.426$ nm is fixed as a typical value for a long-range potential (a being the carbon-carbon distance), but W is varied to describe different screening situations [161, 173, 174].

The impact of such type of disorder is actually strongly related to the value of W. In Fig. 7.2 (main frame), one shows the total elastic scattering time for three values of $W = 1.0, 1.5$ and 2.0 in γ_0 unit. Strinkingly the behavior of $\tau_e(E)$ in the vicinity of the Dirac point is totally different. For $W = 2.0$, its value saturates at $\tau_e(E = 0) \approx 5$ fs, while it increases roughly linearly at higher energies. In sharp contrast, for $W = 1.5$ and $W = 1.0$ an upturn of τ_e is obtained close to the Dirac point followed by a saturation value of $\tau_e(E = 0)$ (about 4 times larger for $W = 1.5$) due to finite density of states. For the weakest disorder ($W = 1$),$\tau_e(E) \sim 1/E$ for low E and $\tau_e(E) \sim E$ for larger E.

This can be rationalized by a Fermi's golden rule calculation of the relaxation time taking the potential as a small perturbation. Besides the energy dependence of the density of states, first assumed to be proportional to E, an additional energy dependent contribution for τ_e by Fourier transforming the long-range potential. For weak disorder the relaxation time for small energies can thus be approximated by $\tau_e \propto \frac{1}{E(1-cE^2)} \approx 1/E + cE$ (focusing the discussion on the positive energy axis). Accordingly one would expect a low-energy peak and a linear slope at higher energies separated by a minimum τ_e at finite E (well away from the Dirac point). In the simulations such a weak disorder limit is nearly realized for $W = 1.0$ as seen in Fig. 2, while for larger disorder the above estimation has to be modified to explain the results. Already for $W = 1.5$ the DOS at the Dirac point is finite and the leading term for $\tau(E)$ at low-energy $1/E$, stemming from the DOS, is strongly reduced and regularized. As a result, the minimum for $\tau(E)$ still exists but is relocated to smaller energies ($E \approx 400meV$). For stronger disorder ($W = 2.0$) the DOS at the Dirac point is large enough that the minimum at finite E vanishes completely. In this case the zero-energy states relax fastest.

Next, to explore localization phenomena, the Peierls phase is introduced (see Appendix H). The Landau levels obtained for clean graphene at $B = 10$ Tesla follow the expected magnetic field dependent $\sqrt{nB}$ scaling (not shown here) [175].

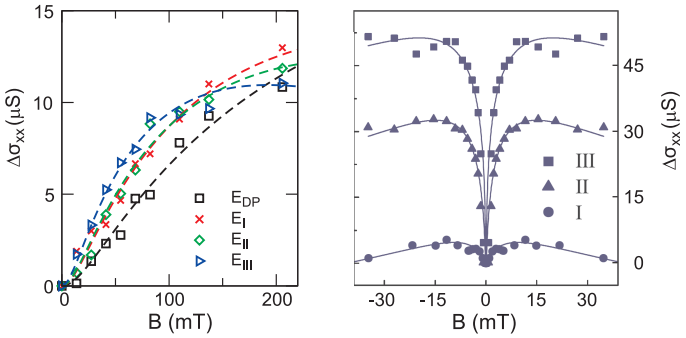

Figure 7.3: (color online) $W = 2.0$. Left panel: $\Delta\sigma(B)$ ($n_i = 0.125\%$, $\xi = 0.426$ nm) for four different Fermi level positions ($E_{\rm DP} = 0, E_{\rm I} = 0.049$ eV, $E_{\rm II} = 0.097$ eV and $E_{\rm III} = 0.146$ eV). Averages over 32 different configurations are performed. Dashed lines are fits from analytical curves (see text). Right panel: experimental data extracted from [168, 169].

The magnetoconductance $\Delta\sigma(B) = \sigma(B) - \sigma(B = 0)$ is shown in the left panels of Fig. 7.3 and Fig. 7.4 for two different disorder strengths. For $W = 2$ (Fig. 7.3), the sign of $\Delta\sigma(B)$ (positive magnetoconductance) evidences a weak-localization behavior, valid for various selected energies. In contrast, the case $W = 1.5$ (Fig. 7.4) shows a clearly different behavior since a change in the sign of $\Delta\sigma(B)$ is observed, suggesting a crossover from weak localization to weak antilocalization, which depends not only on the field strength, but also on the considered energy of charge carriers. An estimation of the elastic mean free path gives $\ell_e \sim 9-20$nm, which is still much smaller than the sample size. Fig. 7.4 (right) gives the experimental results obtained by Tikhonenko and coworkers [168, 169].

In Ref. [174] , using the same long-range disorder potential, it was shown that valley mixing strength was continously enhanced from $W = 1$ to $W = 2$ (with $\xi = 0.426nm$) . The positive magnetoconductance for the case $W = 2$ agrees with the strong contribution of intervalley scattering, since all underlined symmetries have been broken. However by decreasing the disorder strength (from $W = 2$ to $W = 1.5$), WAL is indeed recovered given the reduction of intervalley processes. It is further instructive to relate the simulations with the phenomenologi-

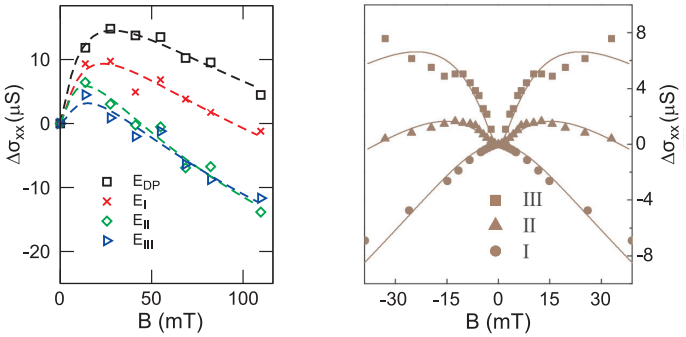

Figure 7.4: (color online) $W = 1.5$. Left panel: $\Delta\sigma(B)$ for four different Fermi level positions ($E_{\rm DP} = 0, E_{\rm I} = 0.049$ eV, $E_{\rm II} = 0.097$ eV and $E_{\rm III} = 0.146$ eV) after Ref. [175]. 64 configurations have been averaged. Dashed lines are fits to analytical cuvers. Right panel: experimental data extracted from [168, 169].

cal law $\Delta\sigma(B) = e^2/\pi h \left\{\mathcal{F}(\tau_B^{-1}/\tau_\varphi^{-1}) - 3\mathcal{F}(\tau_B^{-1}/(\tau_\varphi^{-1} + 2\tau_*^{-1}))\right\}$, where $\mathcal{F}(z) = \ln z + \psi(1/2 + z^{-1})$, $\psi(x)$ is the digamma function and $\tau_B^{-1} = 4eDB/\hbar$ [176]. Good fits can be obtained using a single additional elastic (phenomenological) scattering time τ_* that contains both contributions of intravalley and intervalley scattering [176]. This is sounding since for the considered W values, both scattering processes actually compete and it is not easy to disentangle individual contributions (see Ref. [174]). Least-squares fits (dashed lines) are superimposed to the simulated $\Delta\sigma(B)$ (symbols), taking $\tau_\varphi = 9$ps (the maximum computed time). For $W = 2$ and $W = 1.5$, τ_* ranges within $[1.1 - 2.3]$ps and $[1.5 - 6.3]$ps, respectively (increasing values with increasing energy), thus confirming the weak localization regime for lowest B, which is fully consistent with Ref. [176] ($\tau_i < \tau_\varphi$).

It was thus shown that pseudospin effects can be actually tuned by adjusting a single disorder parameter (W) which denotes the depth of an impurity-driven local Coulomb potential. When $W \geq 1$ (unit of γ_0), local energetics between nearest neighbours A and B sites fluctuate enough to increase intervalley scattering which progressively predominate over the intravalley contribution [174].

7.4 Scattering Times

It is also finally worth to discuss the various behaviors of elastic scattering times, depending on the nature of underlying disorders. In Fig. 7.2, elastic scattering times versus energy (τ_e) are shown for varying oxygen ad-atoms (left inset) and hydrogen ad-atoms (right inset) densities. It is instructive to note that the epoxide defects which actually preserve some local AB symmetry also induce energy-dependent $\tau_e(E)$ ressembling the case of long range Coulomb impurities with onsite potential depth ($W = 1.5$, Fig. 7.2, main frame). Differently, the $\tau_e(E)$ fingerprint of hydrogen defects which break local sp^2 symmetry and local AB degeneracy is more ressembling the case $W = 2$. Such energy-dependence of scattering times are weakly dependent on the defect density but mostly driven by structural re-arrangements and local symmetry breaking, although similar defect density leads to equivalent $\tau_e(E)$ at the Dirac point (in the order of 25-30 fs for $n_i \simeq 0.4\%$, see insets in 7.2)). These features should be of interest to better rationalize the possible origin of defects in different graphene-based materials (see Refs. [177, 178] for some experimental discussion).

7.5 Conclusion

This Chapter has given a brief overview of the different effects disorder can have on the transport properties of graphene. Two degrees of freedom play a very important role in the kind of modifications one can obtain looking at the quantum localization properties of the charge carriers. The first part of the thesis covered mostly differences between sublattice symmetry preserving and symmetry breaking types of disorder. This last Chapter approached the problem from the angle of short and long range disorder. Using simplified models, a transition from long to short range can be achieved, evolving the behavior from weak antilocalization to weak localization. Analogies are drawn with the more realistic disorder models from the first part of the manuscript.

Conclusions and Outlook for the Future

In this Thesis, several results are discussed. An overview of different transport phenoma depending on the kind of graphene functionalization is given. These results range from (by now) widely accepted localization effects in so-called short range disorders which mix the inequivalent Dirac cones, for instance by introduction of oxygen in epoxy position or randomly distributed hydrogen on top of a carbon atom, to possible magnetic fingerprints depending on the underlying magnetic ordering and coupling of hydrogen atoms. The former issue about localization in graphene due to oxygen atoms turns out to be interesting from a phenomelogical point of view, but, *a posteriori*, looks not very interesting for application in industry because the ON/OFF ratio between competing energies is too low. The latter issue of magnetism remains controversial, nevertheless, some progress has been made since our studies in 2010. A brief update on the state of the art is thus in order.

Little doubt exists on possible paramagnetic centers in graphene, induced by edges and defects [150, 179, 180]. Other studies reporting ferromagnetic ordering in reduced graphene oxide systems exist [181, 182, 183], but were often questioned about the exact origin of the magnetism. Residual magnetic impurities which comtaminate intrinsic magnetization of graphene make such studies very tricky. Nevertheless, reproducible results on hydrogenated graphene [184, 185, 186] indicate ferromagnetic coupling might exist after all. All these studies rely on volume and surface-averaged measurements, and so, clear evidence of

local magnetization is still unclear. Recently, Ref. [187] reported STM measurements which indicate the magnetization originates in the unpaired spins from the functionalized carbon sites. The same authors also show that coupling is present, but usually over small fractions of their studied samples [188].

Additionnaly, conclusive prove of a working and new implementation of the transversal conductivity is presented. Analytically predicted step heights are obtained for a simple Anderson disorder model (see Appendix F). Moreover, the prediction of critical states infered by looking at the longitudinal conductivity under magnetic field for epoxy disorder is confirmed and deeper insight is gained by looking at the transverse conductivity. These critical delocalized states carried by disorder at disorder and magnetic field dependent energies require a revised picture going beyond the state of the art. Indeed, the specific role of disorder played in this study is different from literature predicting the QHE to be robust under three kinds of disorder, namely (i) weak potentials V_W (satisfying $V_W < \hbar\omega_c$) [48, 49], (ii) scattering centers defined by potential V_{SC} (satisfying a distance d between centers larger than the magnetic length l_B) [47, 50, 51] and (iii) smooth potentials V_S (satisfying $\Delta V_S = \frac{\hbar\omega_c}{l_B}$) [47, 52, 53, 54, 55, 56, 57, 58, 59].

Epoxy is a scattering center, in the sense that it induces a certain degree of intervalley mixing responsible for quantum localization effects [79]. However, the disorder concentrations in this study do not satisfy the $d \gg l_B$ criterion from (ii). The novelty of this study is thus that it proves the existence of extended states based on the percolation theory [60, 61] in the case of scattering centers, a theory up to now (to the best of our knowledge) only applied to smooth potentials [47, 52, 53, 54, 55, 56, 57, 58, 59] where it was also confirmed experimentally [53]. Differently from smooth potentials where the critical energy E_c (energy at which the extended state is found) is predicted to be at zero energy for electron-hole symmetric potentials , for divacancies, and by extension to epoxy disorder, these critical energies $E_c^{\pm}$ are found at the left and right of $E = 0$ eV. The states at energies away from $E_c^{\pm}$ are localized as expected from the literature, leading in this

case to a zero energy Hall pleateau. To confirm this theory, lower impurity concentrations (0.25% and 0.5%) are at the interface of percolation of states due to the impurities and convential LL0 formation in pristine graphene. Interestingly, three critical energies are thus observed in such samples (E_c and $E_c^{\pm}$).

Some computational limitations of the previous studies are worth mentioning. In the case of oxygen atoms in epoxy position, a small charge transfer occurs (around 0.2 towards the oxygen atom). Albeit negligible at the present energy resolution on such concentrations, such defects might possess small local spins and lead to some new physics, similar to hydrogen atoms. Also a very small dip in conductivity is present as predicted by Ref. [144], but our calculations used less precise energy resolution to properly see this effect. Regarding the studies on hydrogen, the model is limited in the sense than interaction between two impurities only is considered. A more elaborate study of these interactions might alter the predicted MR signal. Also, because now the Kubo implementation includes the effect of the interaction of a magnetic field with the orbital degree of freedom, such study might be approached from a new point of view, extending the present analysis, which only included different Hubbard and DFT ground state calculations to define TB parameters and appreciate the magnitude of required $B-$field.

In a near future, I plan to continue the calculations using the σ_{xy} implementation. New calculations are already running for epoxy disorder to better clarify the peculiar non-integer plateaus at low energy. Other kinds of disorder are planned as well, such as analyzing specific transport fingerprints for polycrystalline graphene. Also, I have started doing calculations during this Thesis on graphene functionalized with Bismuth atoms. Results are too preliminary to include them here, but literature indicates this to be a very promising research area. The Spin Orbit Coupling could thus be introduced within these different conductivity implementations, leading to interesting physics such as the Spin Hall Effect and the Quantum Anomalous Hall Effect.

To actually appreciate the validity of such theoretical simulations, one has to collaborate with experimentalists. The yield of such collabo-

rative studies might be low, because of practical issues such as different timings, but it is still worth the shot. Experiment is nothing without a theory to explain it, and theory is worthless if one cannot appreciate its (in)validity by experiment.

Appendices

Appendix A

Publication List

N. Leconte, J. Moser, P. Ordejon, H.H. Tao, A. Lherbier, A. Bachtold, F. Alsina, C.M. Sotomayor Torres, J.-C. Charlier, and S. Roche. Damaging Graphene with Ozone Treatment: A Chemically Tunable Metal-Insulator Transition. *ACS Nano*, **4** (7), 4033–4038 (2010).

N. Leconte, D. Soriano, S. Roche, P. Ordejon, J.-C. Charlier, and J.J. Palacios. Magnetism-Dependent Transport Phenomena in Hydrogenated Graphene: from Spin-splitting to Localization effects. *ACS Nano*, **5** (5), 3987–3992 (2011).

D. Soriano, N. Leconte, P. Ordejon, J.-C. Charlier, J.J. Palacios, S. Roche. Magnetoresistance and Magnetic Ordering Fingerprints in Hydrogenated Graphene. *Phys. Rev. Lett.*, **107**, 016602 (2011).

N. Leconte, A. Lherbier, F. Varchon, P. Ordejon, S. Roche, and J.-C. Charlier. Quantum Transport in Chemically-modified Two-Dimensional Graphene: From Minimal Conductivity to Anderson Localization. *Phys. Rev. B*, **84**, 235420 (2011). *Editor's Suggestion*

N. Leconte, F. Ortmann, A. Cresti, J.-C. Charlier, and S. Roche. Quantum Hall Effect in Chemically Functionalized Graphene : Defect-Induced Critical States and Breakdown of Electron-Hole Symmetry. Submitted (2013)

S. Roche, N. Leconte, F. Ortmann, A. Lherbier, D. Soriano and J.-C. Charlier. Quantum transport in disordered graphene A theoretical perspective. *Solid State Comm.*, **152**, 1404 (2012)

A. de Jamblinne, N. Leconte, J. C. Charlier. Velocity Anisotropy in Graphene under Local Electrostratic Potentials. In preparation

F. Ortmann, N. Leconte, J. C. Charlier and S. Roche. Transverse Conductivity Implementation in the Kubo-Greenwood-Mahan Formalism. In preparation

Appendix B

Prefactors for Cooperon Correction to Conductivity

The general expression for the cooperon correction to the conductivity for dimension d reads:

$$\frac{-2G_0}{(4\pi)^{d/2}}\left(\frac{D^{\max}}{2d}\right)^{1-d/2}\int_0^\infty dt\frac{1}{t^{d/2}}\left(e^{\frac{-t}{\tau_\phi}}-e^{\frac{-t}{\tau}}\right) \tag{B.1}$$

where $\tau = 2\ell_e^2/D^{\max}$ and $\tau_\phi = L^2/D^{\max}$. The integral is straightforward to solve in $1D$ and $3D$ using Γ functions:

$$\int_0^\infty \frac{1}{t^{d/2}}(e^{-\lambda t}-e^{-\mu t})dt = \Gamma(1-\frac{d}{2})\left[\lambda^{d/2-1}-\mu^{d/2-1}\right] \tag{B.2}$$

In $2D$, the pole at $\Gamma(0)$ requisites another approach. Let

$$G(\lambda,\mu) = \int_0^\infty \frac{(e^{-\lambda t}-e^{-\mu t})}{t}dt, \tag{B.3}$$

for $\lambda, \mu > 0$. There are no problems at $t = 0$ because

$$e^{-\lambda t}-e^{-\mu t} = (\mu-\lambda)t + O(t^2) \tag{B.4}$$

near zero. By substitution

$$G(\lambda,\mu) = G(\lambda/\mu, 1). \tag{B.5}$$

So,

$$F(\lambda) = G(\lambda, 1) = \int_0^\infty \frac{e^{-\lambda t} - e^{-t}}{t} \tag{B.6}$$

needs to be calculated. By integration under the integral sign, we find:

$$F'(\lambda) = -\int_0^\infty e^{-\lambda t} dt = \frac{-1}{\lambda}. \tag{B.7}$$

Since $F(1) = 0$,

$$F(\lambda) = \log \lambda. \tag{B.8}$$

Finally, the integral has the expression:

$$G(\lambda, \mu) = -\log(\lambda/\mu) = \log \mu - \log \lambda. \tag{B.9}$$

In conclusion, the expression for the cooperon given by Akkermans *et al.*[41] has no extra prefactor coming from the integral. Given the definition of L in Eq. (5.14), the prefactors of Eq. (5.12) are obtained using Eq. (B.1). The extra factor $\sqrt{2}$ compared to the correction obtained by Lee *et al.* [139] comes from a different definition of $D(t)$.

Appendix C

Current Operator for Tight-Binding Model

Often, the current operator is expressed as

$$\boldsymbol{j}_i = \frac{2}{mi}\left[\phi^\dagger(\boldsymbol{r})\nabla\phi(\boldsymbol{r}) - \phi(\boldsymbol{r})\nabla\phi^\dagger(\boldsymbol{r})\right]. \tag{C.1}$$

However, in a TB model, it is more convenient to develop an alternate but equivalent expression for the current operator [109]. The derivation starts from the *polarization operator* which is defined, in the TB representation, as

$$\boldsymbol{P} = \sum_i \boldsymbol{R_i} n_i. \tag{C.2}$$

and in a continuous representation as

$$\boldsymbol{P} = \int d^3r \boldsymbol{r}\rho(\boldsymbol{r}) \tag{C.3}$$

in terms of the particle density $\rho(\boldsymbol{r})$. The expression of $\boldsymbol{j}$ using $\boldsymbol{P}$ can be obtained by derivating $\boldsymbol{P}$ in the first line, using the equation of continuity $[\dot{\rho}(\boldsymbol{r},t) = -\nabla\cdot\boldsymbol{j}(\boldsymbol{r},t)]$ in the second line and an integration by parts in

the third line:

$$\begin{aligned}\frac{\partial}{\partial t}\boldsymbol{P} &= \int d^3r \boldsymbol{r}\frac{\partial}{\partial t}\rho(\boldsymbol{r}) \\ &= -\int d^3r \boldsymbol{r}\nabla\cdot\boldsymbol{j}(\boldsymbol{r},t) \\ &= \int d^3r \boldsymbol{j}(\boldsymbol{r},t) \end{aligned} \tag{C.4}$$

where the integral spans the contributions from all particles. In the TB representation, and using the time derivative for an operator, the required expression is finally found:

$$\boldsymbol{j} = \frac{\partial}{\partial t}\boldsymbol{P} = i[H,\boldsymbol{P}]. \tag{C.5}$$

Appendix D

Tentative but flawed interpretation to LL0 splitting

In this Appendix, a tentative interpretation to the apparent zero Landau level splitting is discussed. Conventionally, when observing such splitting in the σ_{xx} curves, the straight-forward explanation requires either spin degeneracy lifting or valley degeneracy lifting (LL0 being 4-fold degenerate). Due to the specific implementation in the Kubo-Greenwood formalism where the spin degree of freedom is not taken into account, Zeeman interaction, Quantum Hall Ferromagnetism, etc can be safely ruled out. The remaining valley degree of freedom is key ingredient in phenomena such as sublattice symmetry breaking physics or Peierls instabilities due to electron-phonon coupling. At some point, an interpretation based on sublattice symmetry breaking due to a gauge field was proposed, but later discarded. Section D.1 argues in favor of this interpretation while Section D.2 proves why this interpretation is incorrect in the considered systems.

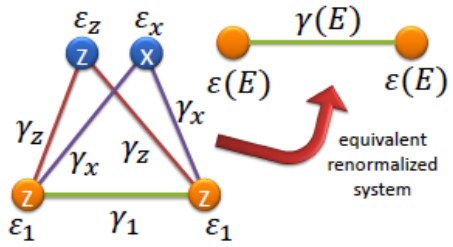

Figure D.1: Definition of the different terms in the equivalent model, based on the work by A. Cresti [30].

D.1 Arguments: pro

In the work by A. Cresti [30], an equivalent model to the TB model used in this Thesis is developed. The physics described in Section 1.2.2 are in line with this equivalent model where only the value of γ_1 is modified, while the other hopping terms γ_2 and γ_3 are kept constant. In addition, the onsite energies of the bridging carbon atoms are modified as well (albeit without inducing inequivalence between the sublattices). The key elements of the equivalent TB Hamiltonian (see Fig. D.1) are:

$$\gamma(E) = \gamma_1 - \frac{\gamma_x^2}{E - \epsilon_x} + \frac{\gamma_z^2}{E - \epsilon_z} \tag{D.1}$$

and

$$\epsilon(E) = \epsilon_1 - \frac{\gamma_x^2}{E - \epsilon_x} + \frac{\gamma_z^2}{E - \epsilon_z}. \tag{D.2}$$

The variations to the hopping terms are depicted in Fig. D.2 with $\delta\gamma_1(\boldsymbol{r}, E) = -\gamma_0 + \gamma(E)$ and $\delta\gamma_2 = \delta\gamma_3 = 0$. The corresponding gauge field is given by

$$A(\boldsymbol{r}, E) = \frac{1}{v_\mathrm{F}} [\delta\gamma_1(\boldsymbol{r}, E), 0, 0] \tag{D.3}$$

which induces the pseudo-magnetic field[1] derived as

$$B_z = \partial_x A_y(\boldsymbol{r}) - \partial_y A_x(\boldsymbol{r}) = -\partial_y \delta\gamma_1(\boldsymbol{r}, E). \tag{D.4}$$

[1] Unlike the real magnetic field, the pseudo-magnetic field does not break time reversal symmetry

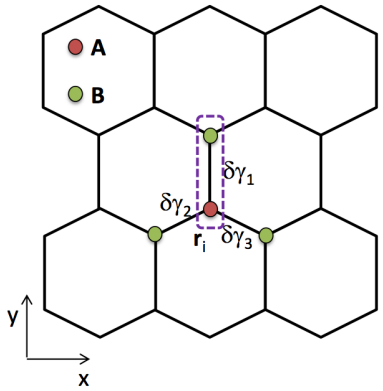

Figure D.2: Variations $\delta\gamma_1$, $\delta\gamma_2$ and $\delta\gamma_3$ to the hopping terms for cell $\boldsymbol{r}_i$. Inequivalent sublattices depicted with red and green disks.

Because $\delta\gamma_1$ is constant in the region between the two carbon atoms and goes to zero outside of it, the only non-zero terms are at the boundaries of these different zones. Consequently, B_z is zero everywhere, except at the position of the bridging carbon atoms, where it has opposite sign (see Fig. D.3).

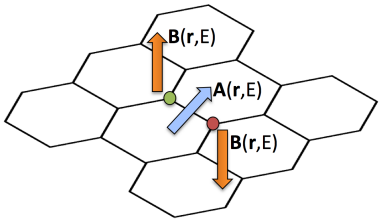

Figure D.3: Behavior of pseudo-magnetic field induced by the disorder induced gauge field. Directions of the pseudo-magnetic field and the vector potential given by orange and blue arrows respectively.

The gauge field approximation is only valid for weak deformations, nevertheless, the direction of the pseudo-magnetic field obtained with this approximation is still valid, only the strength is less reliable [189]. Such pseudo-magnetic field can thus give rise to pseudospin polarization which renders the A and B sublattice inequivalent and may thus, in principle, lift the valley degeneracy of the Landau levels.

The remaining question consists of assessing if this local symmetry breaking is sufficient to explain the existence and position of the extended states presented in Section 5.3 for epoxy oxygen.

D.2 Arguments: contra

In case of smooth, extended pseudo-magnetic fields, the presence of a superposed strong real magnetic field can polarize the valleys because the gauge deformation field changes it sign on the two valleys (to preserve time-reversal symmetry), while the real magnetic field has the same sign in the two valleys (and breaks time-reversal symmetry). Therefore, if the pseudo ($B^\star$) and real (B) magnetic fields are superimposed, this results in an effective field $B + B^\star$ on one valley and $B - B^\star$ on the other valley. Consequentely, the Landau levels have different positions and different degeneracy. However, according to Ref. [189], the LL0 is still at $E = 0$ for both valleys. Also, in the case of a random and dilute distribution of epoxy atoms, the pseudo magnetic field is very local and much higher than the real magnetic field. In Ref. [190], a real magnetic field is shown to have a poor effect on the zigzag edge states (which can be seen as arising from a gauge deformation field) exactly because of the huge difference in their strength. Also, the fact that for the oxygen the position of the two peaks is sensitive to the comparatively weaker magnetic field tends to indicate they are not directly related to the rise of pseudospin localized states. Finally, the onsite energies also have to be considered in this picture. These onsite energies are very high and might be dominant with respect to the off-diagonal matrix elements.

This *potpourri* of inconsistenties drove the interpretation away from the gauge field argument and toward impurity-pinned states which could couple to form extended states separated from the localized states. The further observation of the hybrid situation for low impurity concentrations between a mix of a pristine LL0 at zero energy and impurity related delocalized states at critical energies $E^c_\pm$, leading to three different peaks, serves the letal blow to the gauge field argument.

Appendix E

Convergence Studies for Section 4.3

E.1 Influence of System Size

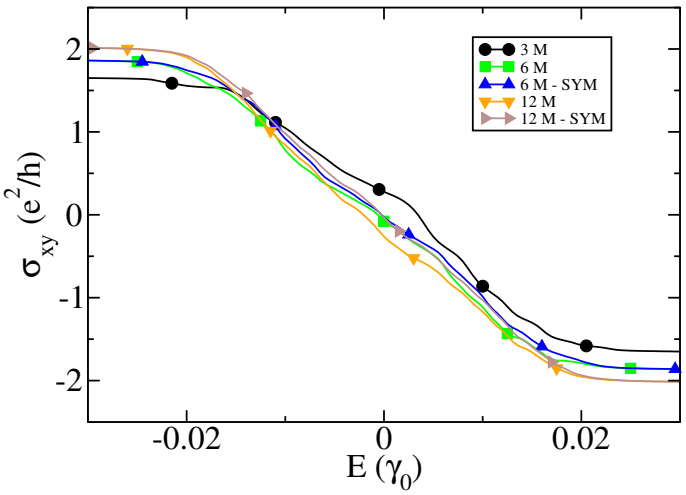

Figure E.1: Convergence study on LL0 for σ_{xy}, increasing the system size. Systems containing 3, 6 and 12 million atoms are considered. 1% of divacancies. Magnetic field of 80 Tesla. $T_{\text{end}} = 500\frac{\hbar}{\gamma_0}$. Damping = 0.01.

To mimic the effect of a perfectly disordered system of experimental size and eliminate sample dependent signatures, increasing the system size can achieve this purpose. Increasing the system size also allows to increase the number of recursion steps to better probe the *eigenstates* of the original Hamiltonian. The scaling of the code being linear for both these approaches, they are considered equivalent. Fig. E.1 indicates that the numerical convergence is qualitatively achieved for systems containing about 6 million atoms. The number of time steps for the convergence runs are smaller than for full production runs, because to observe size dependent physics the largest computation times are not required. Using the energy symmetrization technique (ETS) described in Section E.2, visually perfect step height of LL0 is achieved for 12 million atoms. Nevertheless, because the main goal of this academic model is to confirm the qualitative behavior of (de)localized states round $E = 0$ as predicted from Section 4.2, such precision is not required. For the remaining part of this Section, 6 million atoms are considered. For decreasing disorder, both qualitatively and quantitatively correct behavior is expected.

E.2 Energy Symmetrization Technique

Another useful technique to increase the qualitiy of the curves is by antisymmetrizing the transport data obtained at both positive and negative energies as follows:

$$\sigma_{\mathrm{xy}}(E) = \frac{\sigma_{\mathrm{xy}}(E) - \sigma_{\mathrm{xy}}(-E)}{2} \tag{E.1}$$

Obviously, this can only be applied when the spectrum is supposed to be symmetric around Fermi energy at 0 eV. The effect of energy antysymmetrization is already depicted in Fig. E.1 for different system sizes, using the SYM label in the legends.

E.3 Number of Recursion Steps and Cutoff Value

By increasing the number of recursion steps, a quantitative increase of qualitity is expected. Nevertheless, in Fig. E.2 (lower panel), the

impact of the number of recursion steps is negligible when increasing the value from 4000 to 8000. The upper panel gives the recursion step at which the cutoff value of 10^{-5} is reached. For energies where the step equals 8000, the cutoff is not reached. Only for few energies in the conductivity plateau 8000 steps are sufficient; when disorder is present, a larger number of recursion steps might be required to reach the cutoff value. Note that the choice of cutoff is somehow arbitrary.

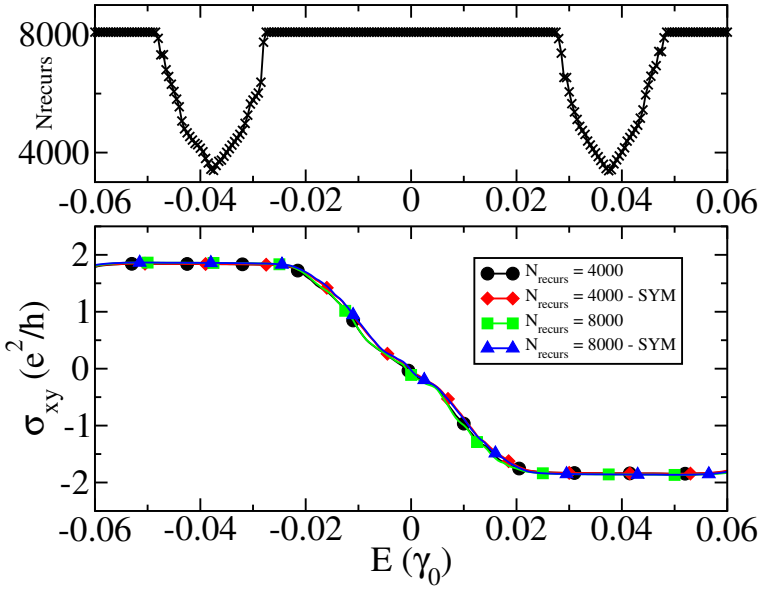

Figure E.2: Convergence on number of recursion steps. Upper panel: recursion step at which the cutoff value of 10^{-5} is reached. For energies where the step equals 8000, the cutoff is not reached. Lower inset: superpostion of curves where 4000 or 8000 is chosen as maximally allowed number of recursion steps. 1% of divacancies. Magnetic field of 80 Tesla.

In Fig. E.3, the evolution of $|\mathrm{Im}(\kappa_j)|\max(|\mathrm{Im}(\kappa_j)|)$ with the number of recursion steps for a set of *unconverged* values from Fig. E.2 indicates that the numerical convergence might be expected but only for a very large number of recursion steps. To be safe, a value of 4000 is chosen for the remainder of this Section.

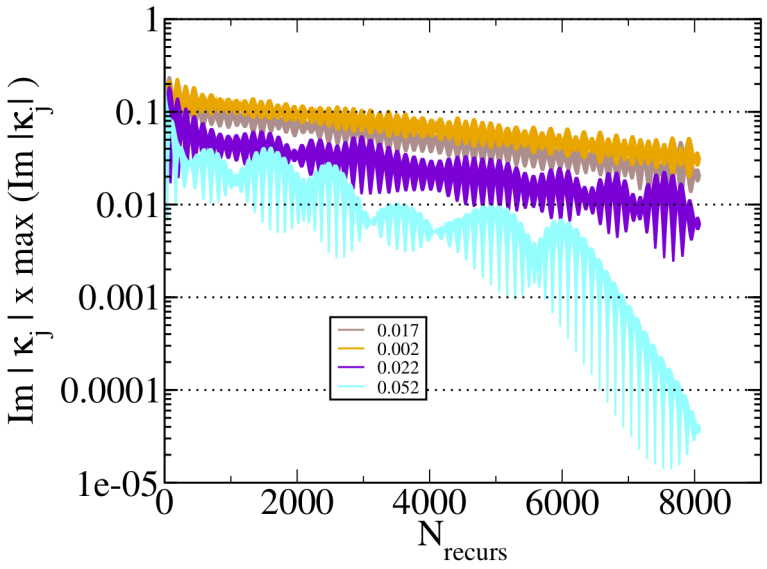

Figure E.3: Evolution of $|\mathrm{Im}(\kappa_j)|\max(|\mathrm{Im}(\kappa_j)|)$. For depicted energies, the cutoff value of 10^{-5} is never reached. 1% of divacancies. Magnetic field of 80 Tesla.

E.4 Energy Broadening

Very briefly, the effect of the energy broadening is discussed. For three different broadening values of $\eta = 0.01$, 0.005 and 0.0005, σ_{xy} is pictured in Fig. E.4. Decreasing the broadening increases the energy resolution, but requires larger values of N_{recurs} to obtain smooth converged curves. The value initially estimated at 0.005 seems reasonable in this sense and is kept as such for remaining studies.

E.5 Time Step

The timestep for the time evolution of the wavepackets is of importance as well. Former calculations showed that the value of σ_{xy} calculated at each time oscillates before saturating to its converged value. Such saturation is easily reached in disordered systems, while for relatively clean samples, an artificial damping factor is used to facilitate this behavior. The oscillations are $B-$field dependent, and thus, a sufficiently fine time

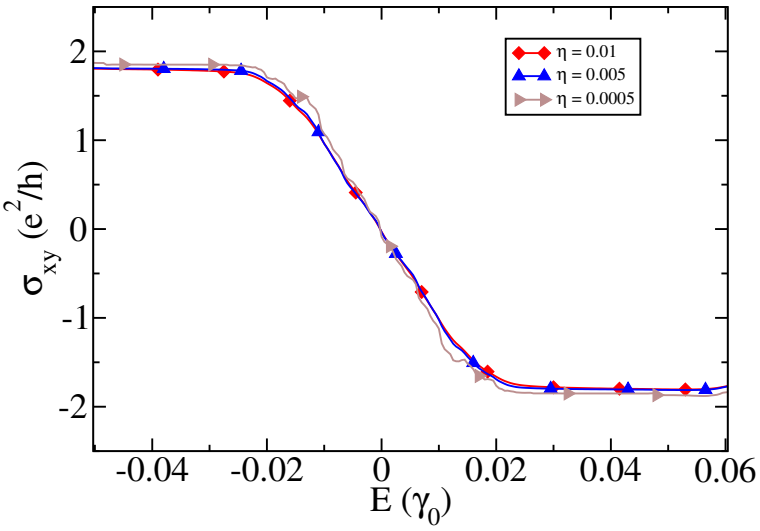

Figure E.4: Effect of three different energy broadening values of η = 0.01, 0.005 and 0.0005 onto LL0. $T_{\text{end}} = 100\frac{\hbar}{\gamma_0}$. 1% of divacancies. Magnetic field of 80 Tesla. Damping = 0.01.

sampling is required to probe the time evolution. Increasing the magnetic field decreases the oscillation period. In Fig. E.5, two different time steps are considered, 0.5 and $5\frac{\hbar}{\gamma_0}$ when picturing the reduced sums RS before conducting the energy and time integration and intoducing the damping factor (see Eq. 3.90). The largest time step, which is used for all calculations, is sufficient to probe the main features. The fine prints of the smaller time step curve (dashed lines), which are related to small disorder effects, average out and do not significantly modify the qualitative behavior of the final σ_{xy} curve. For larger magnetic fields, smaller time steps are required to correctly capture the oscillations which increase their frequency with magnetic field.

E.6 Damping for Time Integration

Some specific features such as disorder induced percolation and localization of states require long calculation times. Such features develop slowly over time, and thus require a smaller damping factor. Neverthe-

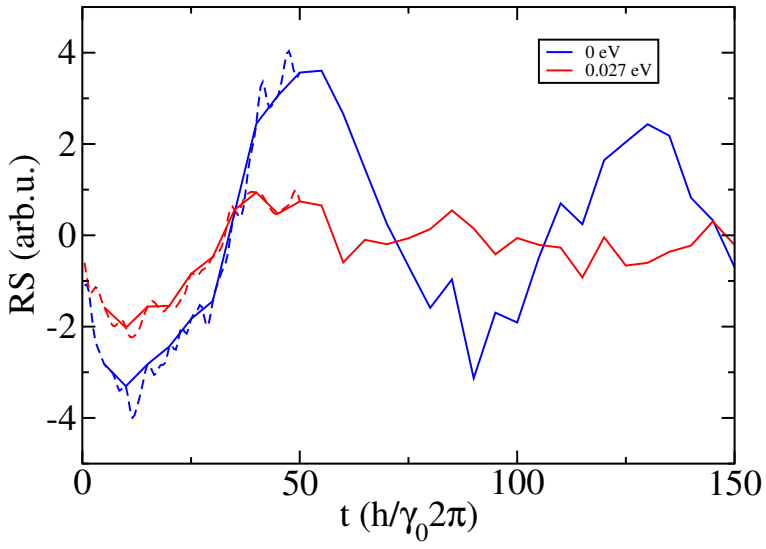

Figure E.5: Reduced sums at each time step before energy and time integration in Eq. 3.90 at energies 0 eV and 0.027 eV. Time steps for wavepacket evolution are equal to 0.5 (dashed) and $5\frac{\hbar}{\gamma_0}$ (solid lines). 1% of divacancies. Magnetic field of 80 Tesla.

less, from an experimental point of view, in the steady state, no difference is expected between a conductivity calculated at any time during the last oscillation period, so practically complete damping has to be ensured at this point. This is exemplified in Fig. E.6 for 1% of divacancies in the sample, varying among three different damping parameters. The damping parameter of 0.01 assures σ_{xy} does not vary anymore at $T_{\mathrm{end}} = 1000\frac{\hbar}{\gamma_0}$. However, the specific localization behavior of localized states at $E = 0$ predicted through the scaling behavior of $\sigma_{\mathrm{xx}}(L)$ is damped out. The smaller values (0.001 and 0.0001) decrease this damping, and nicely features the zero energy plateau. For the other studies, the value of 0.001 is chosen because it allows for an almost steady state while featuring the longtime characteristics. The small residual oscillation still present for the lowest damping value 0.0001 improves the qualitative observation of the new zero energy Hall plateau, but diminishes its qualitative reliability. Even longer computation times would be required to reach a steady state for this latter damping value.

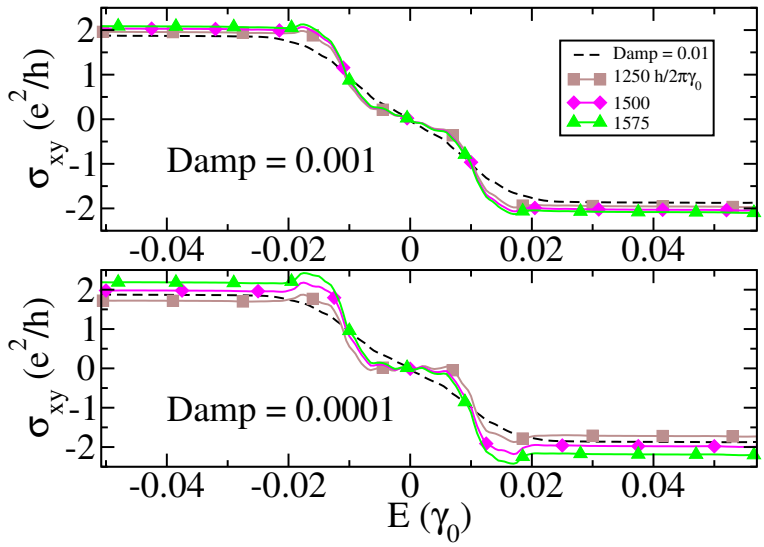

Figure E.6: Effect of damping factor on the longtime characteristics of σ_{xy}. 0.001 reaches a steady state for longest times, while 0.0001 still allows for some residual oscillation between 1250 and 1575$\frac{\hbar}{\gamma_0}$. 1% of divacancies. Magnetic field of 80 Tesla.

Appendix F

Anderson Disorder for Transverse Conductivity

Through the results on these calculations of Anderson disorder at $45T$, for different disorder strenghts W, a better understanding of the methodology is obtained. No surprising physics are observed.

Three different disorder strengths are considered through a random modification of the onsite energies of each atom following $\delta\varepsilon \in [-W/2, W/2]\gamma_0$ with $W = 0.25$, 0.5 or 1. Below $W = 0.7$, disorder is still considered weak, while the last value has significant effect on the transport properties of graphene [191]. The cutoff value to assess the number of required recursion steps is equal to 10^{-5}. This means that at each energy, when $|\mathrm{Im}(\kappa_j)|\max(|\mathrm{Im}(\kappa_j)|)$ goes below the cutoff value, the value of j when this occurs is taken as a maximum.

F.1 Effect of Disorder Strength

In the following, a number of recursion steps equal to 2000 is taken. The damping factor equals 0.01 which reduces the impact of the last calculated time step ($T_{\mathrm{end}} = 500\frac{\hbar}{\gamma_0}$) by 99%.

In Fig. F.1, the impact of the disorder strength is analyzed for LL0. For the weak disorders ($W = 0.25$ and 0.5), the plateau height converges to the expected value of $4\frac{e^2}{h}$ (which includes the $4-$fold degeneracy).

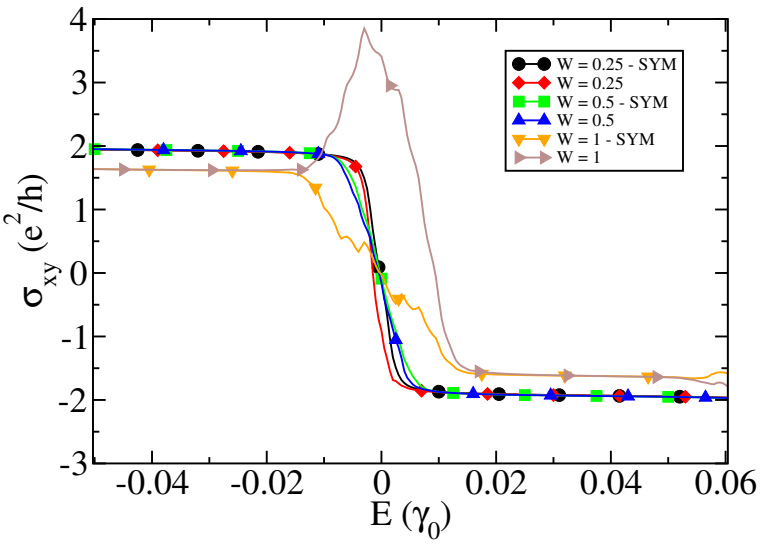

Figure F.1: Effect of disorder strength on LL0 on σ_{xy}. Values of $W = 0.25$, 0.5 or 1, before and after ETS. $T_{\mathrm{end}} = 500\frac{\hbar}{\gamma_0}$. Damping = 0.01. 3 million atoms.

The Energy (anti)-Symmetrization Technique (EST) has almost no effect for these low energies. However, for the high disorder case ($W = 1$), convergence of the plateau height is not achieved, even with the EST. The EST improves a little bit the curves around $E = 0$. High disorder might impede the apparation of perfect quantization, simply based on physical grounds, as was observed on the electron side for epoxy oxygen in Chapter 5 where the Landau levels spectrum could not fully develop, even at highest magnetic fields.

Figure F.2 focuses on the plateau after the first hole LL. Only for weakest disorder is the expected plateau height of $\sigma_{\mathrm{xy}} = 6\frac{e^2}{\hbar}$ almost reached, and this only using the EST. For highest disorder, the situation might maybe be improved a little bit using better converence parameters (see next Sections), but based on physical grounds, a crossover from the Landau level regime to an Anderson insulator might be expected for increasing disorder.

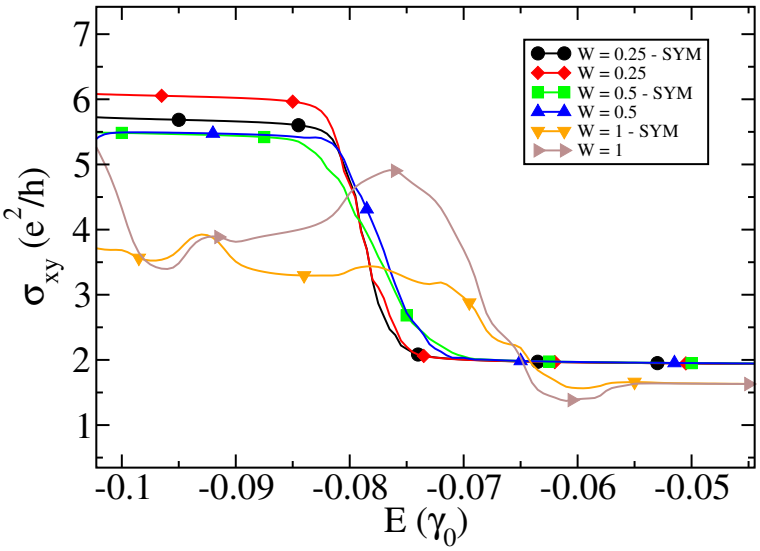

Figure F.2: Effect of disorder strength on LL-1 on σ_{xy}. Values of $W = 0.25$, 0.5 or 1, before and after ETS. $T_{\mathrm{end}} = 500\frac{\hbar}{\gamma_0}$. Damping = 0.01. 3 million atoms.

For higher LLs, the correct quantization is not obtained, even for lowest disorder concentration, in agreement with exact diagonalization calculations [20].

F.2 Effect of System Size

The first technique to improve convergence is by increasing the system size. In Fig. F.3, the Hamiltonian contains respectively about 1, 3, 6 and 12 million atoms. After the EST, the plateau height convergence is almost reached, nevertheless, the number of recursion steps are probably not sufficient to sufficiently probe the full Hamiltonian after reducing it in the Krylov subspace. This is exemplified in the next Section.

F.3 Number of Recursion Steps

In Fig. F.4, the energies are shown for which $|\mathrm{Im}(\kappa_j)|\max(|\mathrm{Im}(\kappa_j)|)$ reached the cutoff value of 10^{-5}. If the data point in the graph is equal

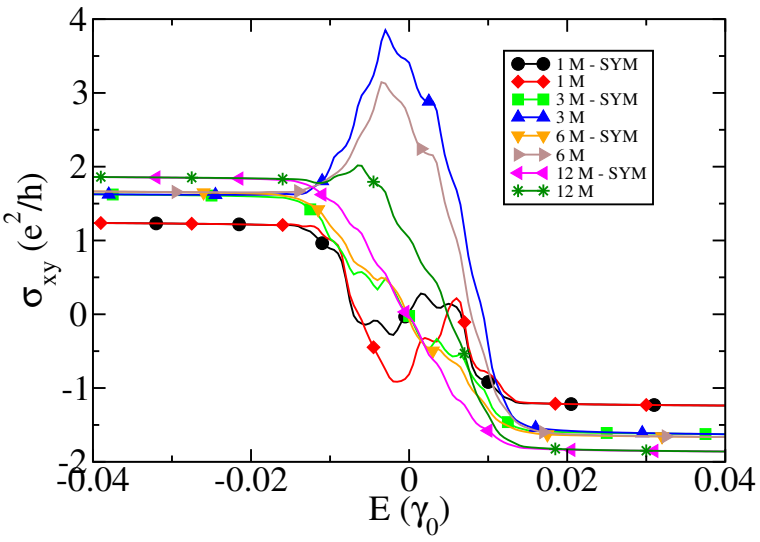

Figure F.3: Effect of system size for $W = 1$ on σ_{xy}, before and after ETS. 3, 6 and 12 million atom systems. $T_{end} = 500\frac{\hbar}{\gamma_0}$. Damping = 0.01.

to $N_{recurs} = 2000$ (8000), it means convergence was not reached for that energy for $W = 0.25$ or $W = 0.5$ ($W = 1$) respectively. For $W = 1$, N_{recurs} was increased from 2000 to 8000 to have a minimum of converged values. Nevertheless, at the energies close to the LLs, even after 8000 steps, the criterion is not satisfied.

For small concentrations, the criterion is not satisfied either, for several energies related to the disorder-induced localized states. However, the convergence on the plateau height is reassuring to assume the cutoff value to be too stringent for the required precision.

In conclusion, when disorder is not too strong, a limited amount of recursion steps is sufficient to achieve convergence.

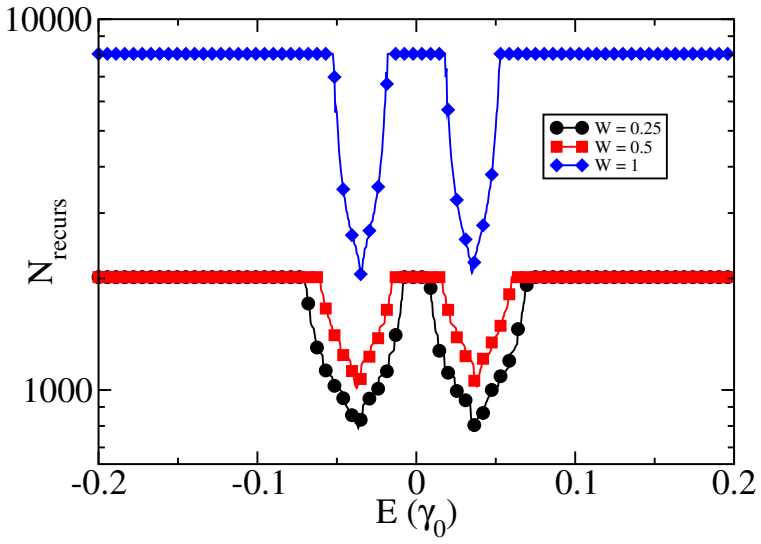

Figure F.4: Convergence value of N_{recurs} for $|\text{Im}(\kappa_j)|\text{max}(|\text{Im}(\kappa_j)|)$ below cutoff value of 10^{-5}. A data point equal to $N_{\text{recurs}} = 2000$ (8000) implies convergence was not reached for that energy for $W = 0.25$ or $W = 0.5$ ($W = 1$) respectively.

F.4 Effect of Increased Number of Recursion Steps

By using the data from the $N_{\text{recurs}} = 8000$ case mentioned above (and another $N_{\text{recurs}} = 4000$ calculation), Fig. F.5 depicts the LL0 step in σ_{xy}. These calculations were performed for $T_{\text{end}} = 100$.

Surprisingly, increasing the number of recursion steps has a very limited impact on the convergence of σ_{xy}.

F.5 Conclusion

The results in the previous Sections indicate the system size might have a larger impact on the convergence than N_{recurs} for highly disordered samples. Nevertheless, observing the quantization in such sample is not common as disorder has the tendency to destroy quantization [20]. Often, only the first plateau might is observed. For samples with small

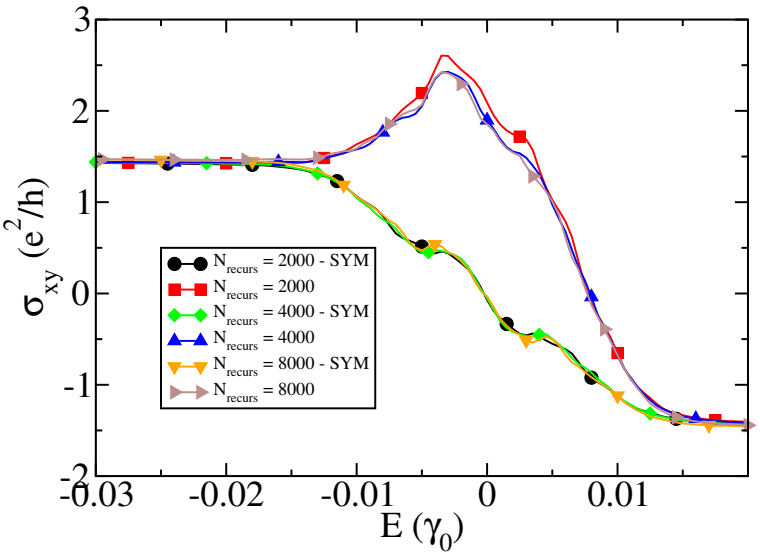

Figure F.5: Effect of increased N_{recurs} on σ_{xy} for $W = 1$. Values of 2000, 4000 and 8000 recursion steps are analyzed, with and without ETS. $T_{\text{end}} = 500\frac{\hbar}{\gamma_0}$. Damping = 0.01.

disorder, even if cutoff is not reached, the system size of 3 million atoms is sufficient with $N_{\text{recurs}} = 2000$.

Appendix G

Convergence on System Size for σ_{xy} on Epoxy Disorder

G.1 Size Effect

Larger system sizes have to be considered because the Energy (anti-)Symmetrization Technique cannot be applied due to the absence of symmetry between electron and holes states in the case of oxygen disorder. Because of the computational cost, the convergence studies on the system size are performed for one of the high disorder distributions (namely 1%) only. Thanks to experience with Anderson disorder (see Appendix F) and double vacancies (see Section 4), lower disorder distributions are certainly converged with the same system size as the one required to achieve convergence for higher disorder. Figure G.1 gives σ_{xy} for systems containing 3, 6, and 12 million atoms. Based on the step height, 6 million atoms might be close to convergence. Nevertheless, because of the lack of symmetry between electrons and holes for epoxy oxygen, systems containing 12 million atoms are used for the remaining of the studies. This system size depicts better electron hole symmetry for the energy range contained by LL0, which is consistent with the symmetry close to zero in the σ_{xx} calculations.

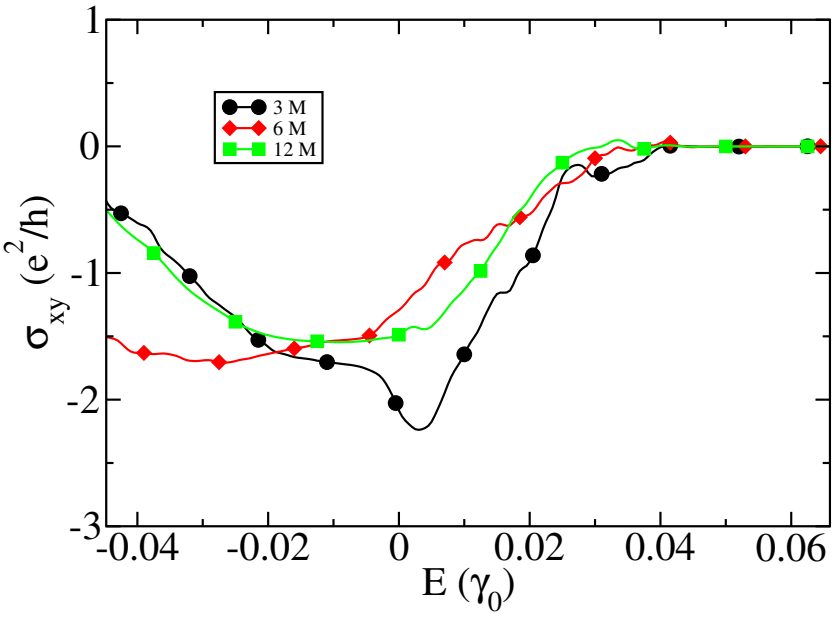

Figure G.1: Effect of size on σ_{xy}. $T_{end} = 700$ (for 3 and 6 million atoms) and $580\frac{\hbar}{\gamma_0}$ (for 12 million atoms). Damping = 0.001.

Appendix H

Peierls Phase

This Appendix presents the trick used for the implementation of the Peierls phase into the TB formalism to allow for arbitrarily weak (perpendicular) fields. This trick is an extension to the work by J. M. Luttinger [192] based on the seminal work by R. Peierls [193].

H.1 Usual Implementation

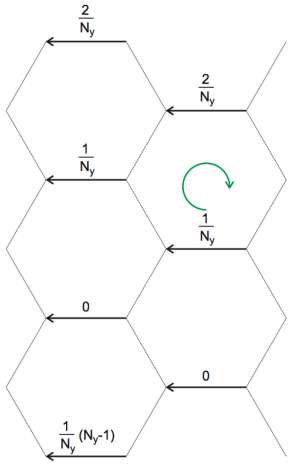

Figure H.1: Layout for definition of Peierls phase using two bonds per hexagon.

The effect of a magnetic field is modeled by a complex phase in the transfer integrals (or hopping terms) between carbon atoms:

$$\gamma_{ab} \to \gamma_{ab} e^{i\phi_{ab}} \tag{H.1}$$

with the phases satisfying $\phi_{ab} = -\phi_{ba}$. This phase has to increase linearly from unit cell to unit cell to allow for a constant B. This is represented in Fig. H.1 where only two bonds per hexagon are used to define the Peierls phase. Because of the periodic boundary conditions, this would be critical, were it not for the freedom of multiples of 2π. Nevertheless, to achieve arbitrarily small magnetic fields, very large graphene sheets are required because of the phase steps

$$\phi = \frac{2\pi}{N_y} \tag{H.2}$$

from hexagon to hexagon. In this case, the total flux

$$\Phi_B = \int_S \boldsymbol{B} \cdot d\boldsymbol{S} \tag{H.3}$$

is given by

$$\Phi_B = \frac{h}{e}\frac{1}{N_y} = B\frac{3}{2}\sqrt{3}a_{\mathrm{cc}}^2. \tag{H.4}$$

To avoid using very large sheets, the following trick is proposed.

H.2 Trick for Small Magnetic Fields

Presently, only two bonds per hexagon are used to define the Peierls phase. Using the phase-neutral bonds, a second similarly strong magnetic field can be defined which points in a different direction and nearly cancels the first one. Figure H.2 represents this using four bonds out of the six. To simplify the notations, $n_2 = N_y$ is introduced as well as $2n_1 = N_x$. The phase steps from Eq. (H.2) are now given by

$$\phi = 2\pi\left(\frac{1}{2n_1} - \frac{1}{n_2}\right) = 2\pi\left(\frac{1}{N_x} - \frac{1}{N_y}\right) \tag{H.5}$$

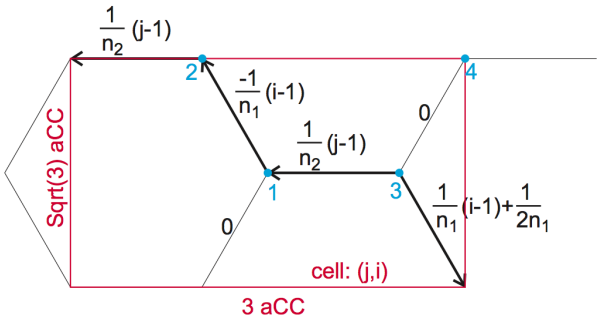

Figure H.2: Layout for definition of Peierls phase using four bonds per hexagon.

For arbitrarily small fields, choosing N_x closest to N_y is most efficient. Consequently

$$N_x = N_y + 1 \tag{H.6}$$

and

$$-\phi = 2\pi \left(\frac{1}{n_2(1+n_2)} \right) = 2\pi \left(\frac{1}{N_y(1+N_y)} \right) \tag{H.7}$$

which scales down much better with the lateral size. The resulting layout is given in more detail in Fig. H.3.

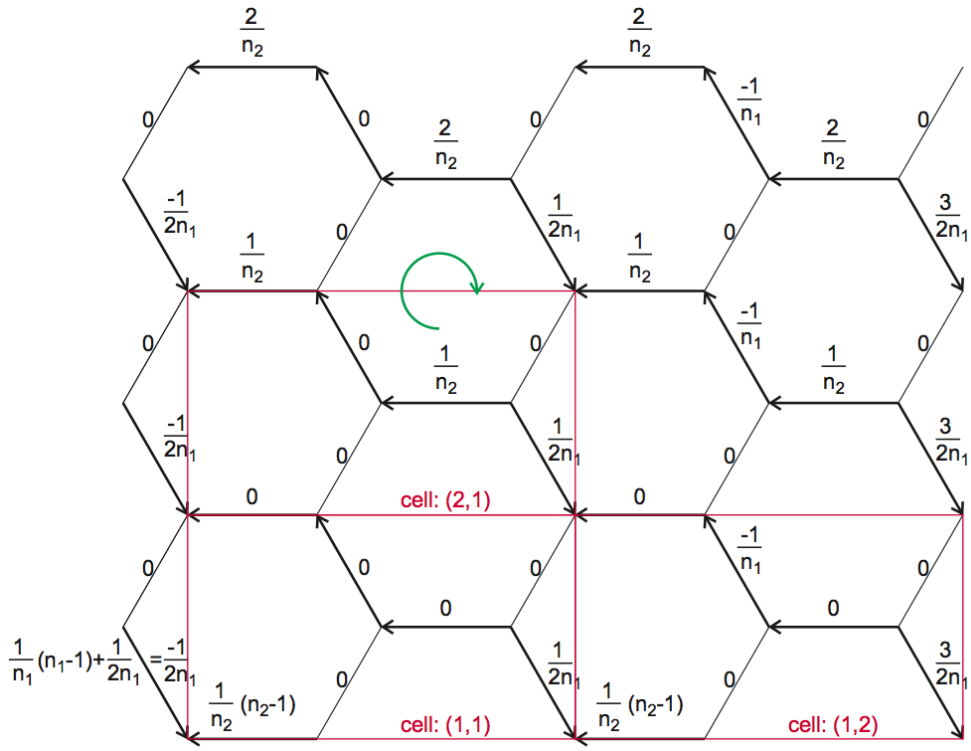

Figure H.3: Layout for definition of Peierls phase using four bonds per hexagon. Extended version.

Bibliography

[1] K.S. Novoselov, A.K. Geim, S.V. Morozov, D. Jiang, Y. Zhang, S.V. Dubonos, I.V. Grigorieva, and A.A. Firsov. *Electric field in atomically thin carbon films.* Science, **306**, 666–669 (2004).

[2] C. Berger, Z. M. Song, T. B. Li, X. B. Li, A. Y. Ogbazghi, R. Feng, Z. T. Dai, A. N. Marchenkov, E. H. Conrad, P. N. First, and W. A. de Heer. *Ultrathin epitaxial graphite: 2D electron gas properties and a route toward graphene-based nanoelectronics.* Journal of Physical Chemistry B, **108**, 19912 (2004).

[3] T. Ohta, A. Bostwick, T. Seyller, K. Horn, and E. Rotenberg. *Controlling the Electronic Structure of Bilayer Graphene.* Science, **313**, 951 (2006).

[4] Xuesong Li, Weiwei Cai, Jinho An, Seyoung Kim, Junghyo Nah, Dongxing Yang, Richard Piner, Aruna Velamakanni, Inhwa Jung, Emanuel Tutuc, Sanjay K. Banerjee, Luigi Colombo, and Rodney S. Ruoff. *Large-Area Synthesis of High-Quality and Uniform Graphene Films on Copper Foils.* Science, **324**, 1312–1314 (2009).

[5] G. D. Ruan, Z. Z. Sun, Z. W. Peng, and J. M. Tour. *Growth of Graphene from Food, Insects and Waste.* ACS Nano, **5**, 7601 (2011).

[6] H. C. Schniepp, J. L. Li, M. J. McAllister, H. Sai, M. Herrera-Alonso, D. H. Adamson, R. K. Prud'homme, R. Car, D. A. Saville, and Aksay I. A. *Functionalized Single Graphene Sheets Derived from Splitting Graphite Oxide.* Journal of Physical Chemistry B, **110**, 1498–1524 (2006).

[7] L. Y. Jiao, Li Zhang, X. R. Wang, G. Diankov, and H. J. Dai. *Narrow graphene nanoribbons from carbon nanotubes.* Nature, **458**, 877 (2009).

[8] D. V. Kosynkin, A. L. Higginbotham, A. Sinitskii, J. R. Lomeda, A. Dimiev, B. K. Price, and J. M. Tour. *Longitudinal unzipping of carbon nanotubes to form graphene nanoribbons.* Nature, **458**, 872 (2009).

[9] J.M. Cai, P. Ruffieux, R. Jaafar, M. Bieri, T. Braun, M. Blankenburg, S. Muoth, A.P. Seitsonen, M. Saleh, X.L. Feng, K. Mullen, and R. Fasel. *Atomically precise bottom-up fabrication of graphene nanoribbons.* Nature, **466**, 470 (2010).

[10] Alexander S. Mayorov, Roman V. Gorbachev, Sergey V. Morozov, Liam Britnell, Rashid Jalil, Leonid A. Ponomarenko, Peter Blake, Kostya S. Novoselov, Kenji Watanabe, Takashi Taniguchi, and A. K. Geim. *Micrometer-Scale Ballistic Transport in Encapsulated Graphene at Room Temperature.* Nano Letters, **11**, 2396–2399 (2011).

[11] Changgu Lee, Xiaoding Wei, Jeffrey W. Kysar, and James Hone. *Measurement of the Elastic Properties and Intrinsic Strength of Monolayer Graphene.* Science, **321**, 385–388 (2008).

[12] A. A. Balandin. *Thermal properties of graphene and nanostructured carbon materials.* Nature, **10**, 569 (2011).

[13] R. R. Nair, P. Blake, A. N. Grigorenko, K. S. Novoselov, T. J. Booth, T. Stauber, N. M. R. Peres, and A. K. Geim. *Fine Structure Constant Defines Visual Transparency of Graphene.* Science, **320**, 1308 (2008).

[14] Graphene Flagship. http://graphene-flagship.eu/.

[15] D Van Tuan, J Kotakoski, T Louvet, F Ortmann, J. C. Meyer, and S. Roche. *Scaling Properties of Charge Transport in Polycrystalline Graphene.* Nano Letters, **13**, 1730 (2013).

[16] L Zhao, R He, K.T. Rim, T Schiros, K S Kim, H Zhou, C Gutierrez, S P Chockalingam, C J Arguello, L Palova, D Nordlund, M.S. Hybertsen, D R Reichman, T.F. Heinz, P. Kim, A Pinczuk, G.W. Flynn, and A N Pasupathy. *Visualizing Individual Nitrogen Dopants in Monolayer Graphene.* Science, **333**, 999–1003 (2011).

[17] R Quhe, J Ma, Z Zeng, K Tang, J Zheng, Y Wang, and Z Ni. *Tunable band gap in few-layer graphene by surface adsorption.* Scientific reports, **3**, 1794 (2013).

[18] Humberto Terrones, Ruitao Lv, Mauricio Terrones, and Mildred S Dresselhaus. *The role of defects and doping in 2D graphene sheets and 1D nanoribbons.* Reports on Progress in Physics, **75**, 062501 (2012).

[19] Hongtao Liu, Yunqi Liu, and Daoben Zhu. *Chemical doping of graphene.* Journal of Materials Chemistry, **21**, 3335–3345 (2011).

[20] DN Sheng, L Sheng, and ZY Weng. *Quantum Hall effect in graphene: Disorder effect and phase diagram.* Physical Review B, **73**, 233406 (2006).

[21] F. Ortmann and S. Roche. *Splitting of the Zero-Energy Landau Level and Universal Dissipative Conductivity at Critical Points in Disordered Graphene.* Physical Review Letters, **110**, 086602 (2013).

[22] J Moser, H Tao, S Roche, F. Alzina, C.M.S. Torres, and A Bachtold. *Magnetotransport in disordered graphene exposed to ozone: From weak to strong localization.* Physical Review B, **81**, 205445 (2010).

[23] A.K. Geim and K.S. Novoselov. *The rise of graphene.* Nature Materials, **6**, 183–191 (2007).

[24] K S Novoselov, A K Geim, S V Morozov, D Jiang, M I Katsnelson, I V Grigorieva, S V Dubonos, and A A Firsov. *Two-dimensional gas of massless Dirac fermions in graphene.* Nature, **438**, 197–200 (2005).

[25] M. I. Katsnelson. *Graphene: carbon in two dimensions.* Materials Today, **10**, 20–27 (2007).

[26] M. Polini, A. Tomadin, R. Asgara, and A. H. Macdonald. *Density functional theory of graphene sheets.* Physical Review B, **78**, 115426 (2008).

[27] J. C. Slater and G. F. Koster. *Simplified LCAO Method for the Periodic Potential Problem.* Physical Review, **94**, 1498–1524 (1955).

[28] P. M. Yu and M. Cardona. *Fundamentals of Semiconductors: Physics and Materials Properties.* Springer, 2010.

[29] C. Kittel. *Introduction to Solid State Physics.* Wiley, 2004.

[30] A. Cresti, A. Lopez-Bezanilla, P. Ordejon, and S. Roche. *Oxygen surface functionalization of graphene nanoribbons for transport gap engineering.* ACS Nano, **5**, 9271–9277 (2011).

[31] David Carpentier, Andrei A Fedorenko, and Edmond Orignac. *Effect of disorder on 2D topological merging transition from a Dirac semi-metal to a normal insulator.* arXiv (2013).

[32] Yasumasa Hasegawa and Keita Kishigi. *Merging Dirac points and topological phase transitions in the tight-binding model on the generalized honeycomb lattice.* Physical Review B, **86**, 165430 (2012).

[33] Hua Tong Yang. *Strain induced shift of Dirac points and the pseudo-magnetic field in graphene.* Journal of Physics: Condensed Matter, **23**, 505502 (2011).

[34] P Delplace and G Montambaux. *Semi-Dirac point in the Hofstadter spectrum.* Physical Review B, **82**, 035438 (2010).

[35] S Banerjee, R Singh, V Pardo, and W Pickett. *Tight-Binding Modeling and Low-Energy Behavior of the Semi-Dirac Point.* Physical Review Letters, **103**, 016402 (2009).

[36] P Dietl, F Piéchon, and G Montambaux. *New magnetic field dependence of Landau levels in a graphenelike structure.* Physical Review Letters, **100**, 236405 (2008).

[37] Matthieu Bellec, Ulrich Kuhl, Gilles Montambaux, and Fabrice Mortessagne. *Topological Transition of Dirac Points in a Microwave Experiment.* Physical Review Letters, **110**, 033902 (2013).

[38] L. Tarruell, D. Greif, T. Uehlinger, G. Jotzu, and T. Esslinger. *Creating, moving and merging Dirac points with a Fermi gas in a tunable honeycomb lattice.* Nature, **483**, 302 (2012).

[39] M.I. Katsnelson and K.S. Novoselov. *Graphene: New bridge between condensed matter physics and quantum electrodynamics.* Solid State Communications, **143**, 3–13 (2007).

[40] M.I. Katsnelson, K.S. Novoselov, and A.K. Geim. *Chiral tunnelling and the Klein paradox in graphene.* Nature Physics, **2**, 620–625 (2006).

[41] E. Akkermans and G. Montambaux. *Mesoscopic Physics of Electrons and Photons.* Cambridge, 2007.

[42] Edward McCann. *Staying or going? Chirality decides!* Physics, **2** (2009).

[43] R. Prange and S. Girvin. *The Quantum Hall Effect.* Springer-Verlag, 1990.

[44] J. Jackson. *Classical Electrodynamics.* Wiley New York, 1975.

[45] R. Prange. *Quantized Hall resistance and the measurement of the fine-structure constant.* Physical Review B, **23**, 4802 (1981).

[46] R. B. Laughlin. *Quantized Hall conductivity in two dimensions.* Physical Review B, **23**, 5632–5633 (1981).

[47] R. Joynt and R. Prange. *Conditions for the quantum Hall effect.* Physical Review B, **29**, 3303 (1984).

[48] D. J. Thouless. *Localisation and the two-dimensional Hall effect.* Journal of Physics C, **14**, 3475 (1981).

[49] B. I. Halperin. *Quantized Hall conductance, current-carrying edge states, and the existence of extended states in a two-dimensional disordered potential.* Physical Review B, **25**, 2185 (1982).

[50] R. Prange. *Conditions for charge fractionalization.* Physical Review B, **26**, 991 (1982).

[51] J. T. Chalker. *Conditions for the quantum Hall effect.* Surface Science, **142**, 182 (1984).

[52] S. V. Iordansky. *On the conductivity of two dimensional electrons in a strong magnetic field.* Solid State Communications, **43**, 1 (1982).

[53] M. Floser, B. A. Piot, C. L. Campbell, D. K. Maude, M. Henini, R. Airey, Z. R. Wasilewski, S. Florens, and T. Champel. *Classical percolation fingerprints in the high temperature regime of the quantum Hall effect.* New Journal of Physics, **15**, 083027 (2013).

[54] R. E. Prange and R. Joynt. *Conduction in a strong field in two dimensions: The quantum Hall effect.* Physical Review B, **25**, 2943 (1982).

[55] Kazarinov R. F. and S. Luryi. *Quantum percolation and quantization of Hall resistance in two-dimensional electron gas.* Physical Review B, **25**, 7626 (1982).

[56] S. Luryi and Kazarinov R. F. *Theory of quantized Hall effect at low temperatures.* Physical Review B, **27**, 1386 (1983).

[57] S. A. Trugman. *Localization, percolation, and the quantum Hall effect.* Physical Review B, **27**, 7539 (1983).

[58] G. F. Giuliani, J. J. Quinn, and S. C. Ying. *Quantization of the Hall conductance in a two-dimensional electron gas.* Physical Review B, **28**, 2969 (1983).

[59] M. Tsukada. *On the Tail States of the Landau Subbands in MOS Structures under Strong Magnetic Field.* Journal of the Physical Society Japan, **41**, 1466 (1976).

[60] D. Stauffer. *Scaling theory of percolation clusters.* Physics Reports, **54**, 1 (1979).

[61] J. W. Essam. *Percolation theory.* Reports on Progress in Physics, **43**, 7 (1980).

[62] K. v. Klitzing, G. Dorda, and M. Pepper. *New Method for High-Accuracy Determination of the Fine-Structure Constant Based on Quantized Hall Resistance.* Physical Review Letters, **45**, 494 (1980).

[63] Yuanbo Zhang, Yan-Wen Tan, Horst L Stormer, and Philip Kim. *Experimental observation of the quantum Hall effect and Berry's phase in graphene.* Nature, **438**, 201–204 (2005).

[64] M Goerbig. *Electronic properties of graphene in a strong magnetic field.* Review of Modern Physics, **83**, 1193–1243 (2011).

[65] J W McClure. *Diamagnetism of graphite.* Physical Review, **104**, 666 (1956).

[66] A H Castro Neto, N M R Peres, K S Novoselov, and A K Geim. *The electronic properties of graphene.* Review of Modern Physics, **81**, 109–162 (2009).

[67] Peter Rickhaus, Markus Weiss, Laurent Marot, and Christian Schönenberger. *Quantum Hall Effect in Graphene with Superconducting Electrodes.* Nano Letters, **12**, 1942–1945 (2012).

[68] Yafis Barlas, Kun Yang, and A H MacDonald. *Quantum Hall effects in graphene-based two-dimensional electron systems.* Nanotechnology, **23**, 052001 (2012).

[69] Y Zhang, Z Jiang, J P Small, M S Purewal, Y-W Tan, M Fazlollahi, J D Chudow, J A Jaszczak, H L Stormer, and P. Kim. *Landau-Level Splitting in Graphene in High Magnetic Fields.* Physical Review Letters, **96**, 136806 (2006).

[70] Kentaro Nomura and Allan H MacDonald. *Quantum Hall Ferromagnetism in Graphene.* Physical Review Letters, **96**, 256602 (2006).

[71] A F Young, C R Dean, L Wang, H Ren, P Cadden-Zimansky, K Watanabe, T Taniguchi, J Hone, K L Shepard, and P. Kim. *Spin and valley quantum Hall ferromagnetism in graphene.* Nature Physics, **8**, 550–556 (2012).

[72] J Jung and A H MacDonald. *Theory of the magnetic-field-induced insulator in neutral graphene sheets.* Physical Review B, **80**, 235417 (2009).

[73] K Bennaceur, P Jacques, F Portier, P Roche, and D C Glattli. *Unveiling quantum Hall transport by Efros-Shklovskii to Mott variable-range hopping transition in graphene.* Physical Review B, **86**, 085433 (2012).

[74] H Aoki. *Quantised Hall effect.* Reports on Progress in Physics, **50**, 655–730 (1987).

[75] P. M. Ostrovsky, I. V. Gornyi, and A. D. Mirlin. *Theory of anomalous quantum Hall effects in graphene.* Physical Review B, **77**, 195430 (2008).

[76] J. Guillemette, S. S. Sabri, Binxin Wu, K. Bennaceur, P. E. Gaskell, M. Savard, P. L. Lévesque, F. Mahvash, A. Guermoune, M. Siaj, R. Martel, T. Szkopek, and G. Gervais. *Quantum Hall Effect in Hydrogenated Graphene.* Physical Review Letters, **110**, 176801 (2013).

[77] Alessandro Cresti, Norbert Nemec, Blanca Biel, Gabriel Niebler, François Triozon, Gianaurelio Cuniberti, and Stephan Roche. *Charge transport in disordered graphene-based low dimensional materials.* Nano Research, **1**, 361–394 (2008).

[78] TO Wehling, MI Katsnelson, and AI Lichtenstein. *Impurities on graphene: Midgap states and migration barriers.* Physical Review B, **80**, 085428 (2009).

[79] N Leconte, A Lherbier, F Varchon, P Ordejón, S Roche, and J-C Charlier. *Quantum transport in chemically modified two-dimensional graphene: From minimal conductivity to Anderson localization.* Physical Review B, **84**, 235420 (2011).

[80] Stephan Roche, Nicolas Leconte, Frank Ortmann, Aurélien Lherbier, David Soriano, and Jean-Christophe Charlier. *Quantum transport in disordered graphene A theoretical perspective.* Solid State Communications, **152**, 1404–1410 (2012).

[81] A Giesbers, L Ponomarenko, K Novoselov, A Geim, M Katsnelson, J Maan, and U Zeitler. *Gap opening in the zeroth Landau level of graphene.* Physical Review B, **80**, 201403 (2009).

[82] E Kurganova, H van Elferen, A McCollam, L Ponomarenko, K Novoselov, A Veligura, B van Wees, J Maan, and U Zeitler. *Spin splitting in graphene studied by means of tilted magnetic-field experiments.* Physical Review B, **84** (2011).

[83] Yue Zhao, Paul Cadden-Zimansky, Fereshte Ghahari, and Philip Kim. *Magnetoresistance Measurements of Graphene at the Charge Neutrality Point.* Physical Review Letters, **108**, 106804 (2012).

[84] D W Boukhvalov and M I Katsnelson. *Chemical Functionalization of Graphene with Defects.* Nano Letters, **8**, 4373–4379 (2008).

[85] Y H Lu, W Chen, Y P Feng, and P M He. *Tuning the Electronic Structure of Graphene by an Organic Molecule.* Journal of Physical Chemistry B, **113**, 2–5 (2009).

[86] Zhengzong Sun, Dustin K James, and James M Tour. *Graphene Chemistry: Synthesis and Manipulation.* Journal of Physical Chemistry Letters, **2**, 2425–2432 (2011).

[87] Paul S Weiss. *A Conversation with Prof. Dr. Klaus von Klitzing: Discoverer of the Quantum Hall Effect.* ACS Nano, **2**, 609–611 (2008).

[88] T J B M Janssen, N E Fletcher, R Goebel, J M Williams, A Tzalenchuk, R Yakimova, S Kubatkin, S Lara-Avila, and V I Fal'ko. *Graphene, universality of the quantum Hall effect and redefinition of the SI system.* New Journal of Physics, **13**, 093026 (2011).

[89] J Guignard, D Leprat, D Glattli, F Schopfer, and W Poirier. *Quantum Hall effect in exfoliated graphene affected by charged impurities: Metrological measurements.* Physical Review B, **85**, 165420 (2012).

[90] P. Hohenberg and W. Kohn. *Inhomogeneous Electron Gas.* Physical Review, **136**, B864–B871 (1964).

[91] M. C. Payne, M. P. Teter, D. C. Allan, T. A. Arias, and J. D. Joannopoulos. *Iterative minimization techniques for ab initio total-energy calculations: molecular dynamics and conjugate gradients.* Review of Moders Physics, **64**, 1045–1097 (1992).

[92] W. Kohn and L. J. Sham. *Self-Consistent Equations Including Exchange and Correlation Effects.* Physical Review, **140**, A1133–A1138 (1965).

[93] D. M. Ceperley and B. J. Alder. *Ground State of the Electron Gas by a Stochastic Method.* Physical Review Letters, **45**, 566–569 (1980).

[94] John P. Perdew and Yue Wang. *Accurate and simple analytic representation of the electron-gas correlation energy.* Physical Review B, **45**, 13244–13249 (1992).

[95] John P. Perdew, Kieron Burke, and Matthias Ernzerhof. *Generalized Gradient Approximation Made Simple.* Physical Review Letters, **77**, 3865–3868 (1996).

[96] R. M. Martin. *Electronic Structure: Basic Theory and Practical Methods.* Cambridge University Press, 2004.

[97] F. Triozon, S. Roche, A. Rubio, and D. Mayou. *Electrical transport in carbon nanotubes: Role of disorder and helical symmetries.* Physical Review B, **69**, 121410 (2004).

[98] A. Lherbier, B. Biel, Y.-M. Niquet, and S. Roche. *Transport length scales in disordered graphene-based materials: Strong localization regimes and dimensionality effects.* Physical Review Letters, **100**, 036803 (2008).

[99] S. Roche and D. Mayou. *Conductivity of quasiperiodic systems: A numerical study.* Physical Review Letters, **79**, 2518–2521 (1997).

[100] S. Roche. *Quantum transport by means of O(N) real-space methods.* Physical Review B, **59**, 2284–2291 (1999).

[101] S. Roche, F. Triozon, A. Rubio, and D. Mayou. *Conduction mechanisms and magnetotransport in multiwalled carbon nanotubes.* Physical Review B, **64**, 121401 (2001).

[102] S. Roche and R. Saito. *Magnetoresistance of carbon nanotubes: From molecular to mesoscopic fingerprints.* Physical Review Letters, **87**, 2468031 (2001).

[103] S. Latil, S. Roche, D. Mayou, and J.-C. Charlier. *Mesoscopic transport in chemically doped carbon nanotubes.* Physical Review Letters, **92**, 256805–1 (2004).

[104] H. Ishii, F. Triozon, N. Kobayashi, K. Hirose, and S. Roche. *Charge transport in carbon nanotubes based materials: a Kubo-Greenwood computational approach.* Comptes Rendus Physique, **10**, 283–296 (2009).

[105] Rémi Avriller, Sylvain Latil, Franois Triozon, X. Blase, and Stephan Roche. *Chemical disorder strength in carbon nanotubes: Magnetic tuning of quantum transport regimes.* Physical Review B, **74**, 121406 (2006).

[106] Shangduan Wu, Lei Jing, Qunxiang Li, Q. W. Shi, Jie Chen, Haibin Su, Xiaoping Wang, and Jinlong Yang. *Average density of states in disordered graphene systems.* Physical Review B, **77**, 195411 (2008).

[107] Hyoung Joon Choi, Jisoon Ihm, Steven G. Louie, and Marvin L. Cohen. *Defects, Quasibound States, and Quantum Conductance in Metallic Carbon Nanotubes.* Physical Review Letters, **84**, 2917–2920 (2000).

[108] A. Lherbier. *Etude des proprietes electroniques et des proprietes de transport de nanofils semiconducteurs et de plans de graphene.* Universite Joseph Fourier, 2008. These de Doctorat.

[109] Gerald D Mahan. *Many-Particle Physics.* Springer, 2000.

[110] G. Lee, B. Lee, J. Kim, and K. Cho. *Ozone adsorption on graphene: Ab initio study and experimental validation.* Journal of Physical Chemistry C, **113**, 14225–14229 (2009).

[111] A. Cresti, G. Grosso, and G. Pastori Parravicini. *Theoretical imaging of current profiles in two-dimensional devices.* European Physics Journal B, **53**, 537 (2006).

[112] Md Zakir Hossain, James E Johns, Kirk H Bevan, Hunter J Karmel, Yu Teng Liang, Shinya Yoshimoto, Kozo Mukai, Tatanori Koitaya, Jun Yoshinobu, Maki Kawai, Amanda M Lear, Larry L Kesmodel, Steven L Tait, and Mark C Hersam. *Chemically homogeneous and thermally reversible oxidation of epitaxial graphene.* Nature Chemistry, **4**, 305–309 (2012).

[113] D. A. Bahamon, A. L. C. Pereira, and P. A. Schulz. *Inner and outer edge states in graphene rings: A numerical investigation.* Physical Review B, **79**, 125414 (2009).

[114] D. A. Bahamon, A. L. C. Pereira, and P. A. Schulz. *Tunable resonances due to vacancies in graphene nanoribbons.* Physical Review B, **82**, 165438 (2010).

[115] A. L. C. Pereira and P. A. Schulz. *Additional levels between Landau bands due to vacancies in graphene: Towards defect engineering.* Physical Review B, **78**, 125402 (2008).

[116] Youngwoo Nam, Jie Sun, Niclas Lindvall, Seung Jae Yang, Dmitry Kireev, Chong Rae Park, Yung Woo Park, and August Yurgens. *Quantum Hall effect in graphene decorated with disordered multilayer patches.* Applied Physics Letters, **103**, 233110 (2013).

[117] F.L. Hirshfeld. *Bonded-atom fragments for describing molecular charge densities.* Theoretica Chimica Acta, **44**, 129–138 (1977).

[118] C. Fonseca Guerra, J.-W. Handgraaf, E.J. Baerends, and F.M. Bickelhaupt. *Voronoi Deformation Density (VDD) Charges: Assessment of the Mulliken, Bader, Hirshfeld, Weinhold, and VDD Methods for Charge Analysis.* Journal of Computational Chemistry, **25**, 189–210 (2004).

[119] F.M. Bickelhaupt, N.J.R. Van Eikema Hommes, C.F. Guerra, and E.J. Baerends. *The carbon-lithium electron pair bond in (CH3Li)n (n = 1, 2, 4).* Organometallics, **15**, 2923–2931 (1996).

[120] M.A. Zwijnenburg, S.T. Bromley, C. Van Alsenoy, and T. Maschmeyer. *Factors affecting ionicity in all-silica materials: A density functional cluster study.* Journal of Physical Chemistry A, **106**, 12376–12385 (2002).

[121] R. Dronskowski and P.E. Blochl. *Crystal orbital hamilton populations (COHP). Energy-resolved visualization of chemical bonding in solids based on density-functional calculations.* Journal of Physical Chemistry, **97**, 8617–8624 (1993).

[122] T. Hughbanks and R. Hoffmann. *Chains of trans-edge-sharing molybdenum octahedra: Metal-metal bonding in extended systems.* Journal of the American Chemical Society, **105**, 3528–3537 (1983).

[123] A. Lherbier, S.M.-M. Dubois, X. Declerck, S. Roche, Y.-M. Niquet, and J.-C. Charlier. *Two-dimensional graphene with structural defects: Elastic mean free path, minimum conductivity, and anderson transition.* Physical Review Letters, **106**, 046803 (2011).

[124] T.O. Wehling, A.V. Balatsky, M.I. Katsnelson, A.I. Lichtenstein, K. Scharnberg, and R. Wiesendanger. *Local electronic signatures*

of impurity states in graphene. Physical Review B, **75**, 125425 (2007).

[125] V.M. Pereira, J.M.B. Lopes Dos Santos, and A.H. Castro Neto. *Modeling disorder in graphene.* Physical Review B, **77**, 115109 (2008).

[126] X. Wu, M. Sprinkle, X. Li, F. Ming, C. Berger, and W.A. De Heer. *Epitaxial-graphene/graphene-oxide junction: An essential step towards epitaxial graphene electronics.* Physical Review Letters, **101**, 026801 (2008).

[127] K.A. Mkhoyan, A.W. Contryman, J. Silcox, D.A. Stewart, G. Eda, C. Mattevi, S. Miller, and M. Chhowalla. *Atomic and electronic structure of graphene-oxide.* Nano Letters, **9**, 1058–1063 (2009).

[128] B. Biel, X. Blase, F. Triozon, and S. Roche. *Anomalous doping effects on charge transport in graphene nanoribbons.* Physical Review Letters, **102**, 096803 (2009).

[129] B. Biel, F. Triozon, X. Blase, and S. Roche. *Chemically induced mobility gaps in graphene nanoribbons: A route for upscaling device performances.* Nano Letters, **9**, 2725–2729 (2009).

[130] E.R. Mucciolo and C.H. Lewenkopf. *Disorder and electronic transport in graphene.* Journal of Physics Condensed Matter, **22**, 273201 (2010).

[131] J.W. Klos and I.V. Zozoulenko. *Effect of short- and long-range scattering on the conductivity of graphene: Boltzmann approach vs tight-binding calculations.* Physical Review B, **82**, 081414 (2010).

[132] P.M. Ostrovsky, I.V. Gornyi, and A.D. Mirlin. *Electron transport in disordered graphene.* Physical Review B, **74**, 235443 (2006).

[133] N.H. Shon and T. Ando. *Quantum Transport in Two-Dimensional Graphite System.* Journal of the Physical Society of Japan, **67**, 2421–2429 (1998).

[134] J.E. Santos, N.M.R. Peres, J.M.B. Lopes Dos Santos, and A.H. Castro Neto. *Electronic doping of graphene by deposited transition metal atoms.* Physical Review B, **84**, 085430 (2011).

[135] E. Pallecchi, A.C. Betz, J. Chaste, G. Feve, B. Huard, T. Kontos, J.-M. Berroir, and B. Placais. *Transport scattering time probed through rf admittance of a graphene capacitor.* Physical Review B, **83**, 125408 (2011).

[136] K. Nomura and A.H. MacDonald. *Quantum transport of massless dirac fermions.* Physical Review Letters, **98**, 076602 (2007).

[137] T. Stauber, N.M.R. Peres, and F. Guinea. *Electronic transport in graphene: A semiclassical approach including midgap states.* Physical Review B, **76**, 205423 (2007).

[138] K.I. Bolotin, K.J. Sikes, J. Hone, H.L. Stormer, and P. Kim. *Temperature-dependent transport in suspended graphene.* Physical Review Letters, **101**, 096802 (2008).

[139] T.V. Ramakrishnan and P.A. Lee. *Disordered Electronic Systems.* Review of Modern Physics, **57** (1985).

[140] D.J. Thouless. *Localization distance and mean free path in one-dimensional disordered systems.* Journal of Physics C: Solid State Physics, **6**, L49–L51 (1973).

[141] C.W.J. Beenakker. *Random-matrix theory of quantum transport.* Reviews of Modern Physics, **69**, 731–808 (1997).

[142] A.F. Ioffe and A.R. Regel. *Non-crystalline, amorphous and liquid electronic semiconductors.* Progress in Semiconductors, **4**, 237–291 (1960).

[143] Ferdinand Evers and Alexander Mirlin. *Anderson transitions.* Review of Modern Physics, **80**, 1355–1417 (2008).

[144] Guy Trambly de Laissardière and Didier Mayou. *Conductivity of Graphene with Resonant and Nonresonant Adsorbates.* Physical Review Letters, **111**, 146601 (2013).

[145] J. Fernandez-Rossier and J.J. Palacios. *Magnetism in graphene nanoislands.* Physical Review Letters, **99**, 177204 (2007).

[146] O.V. Yazyev and L. Helm. *Defect-induced magnetism in graphene.* Physical Review B, **75**, 125408 (2007).

[147] J.J. Palacios, J. Fernandez-Rossier, and L. Brey. *Vacancy-induced magnetism in graphene and graphene ribbons.* Physical Review B, **77**, 195428 (2008).

[148] E.H. Lieb. *Two theorems on the Hubbard model.* Physical Review Letters, **62**, 1201–1204 (1989).

[149] M.M. Ugeda, I. Brihuega, F. Guinea, and J.M. Gomez-Rodriguez. *Missing atom as a source of carbon magnetism.* Physical Review Letters, **104**, 096804 (2010).

[150] M. Sepioni, R.R. Nair, S. Rablen, J. Narayanan, F. Tuna, R. Winpenny, A.K. Geim, and I.V. Grigorieva. *Limits on intrinsic magnetism in graphene.* Physical Review Letters, **105**, 207205 (2010).

[151] H. Ohldag, P. Esquinazi, E. Arenholz, D. Spemann, M. Rothermel, A. Setzer, and T. Butz. *The role of hydrogen in room-temperature ferromagnetism at graphite surfaces.* New Journal of Physics, **12**, 123012 (2010).

[152] D. Soriano, F. Munoz-Rojas, J. Fernandez-Rossier, and J.J. Palacios. *Hydrogenated graphene nanoribbons for spintronics.* Physical Review B, **81**, 165409 (2010).

[153] L. Pisani, J.A. Chan, B. Montanari, and N.M. Harrison. *Electronic structure and magnetic properties of graphitic ribbons.* Physical Review B, **75**, 064418 (2007).

[154] J.M. Soler, E. Artacho, J.D. Gale, A. Garcia, J. Junquera, P. Ordejon, and D. Sanchez-Portal. *The SIESTA method for ab initio order-N materials simulation.* Journal of Physics Condensed Matter, **14**, 2745–2779 (2002).

[155] Z. Zanolli and J.-C. Charlier. *Spin transport in carbon nanotubes with magnetic vacancy-defects.* Physical Review B, **81**, 165406 (2010).

[156] J. Zhou, Q. Wang, Q. Sun, X.S. Chen, Y. Kawazoe, and P. Jena. *Ferromagnetism in semihydrogenated graphene sheet.* Nano Letters, **9**, 3867–3870 (2009).

[157] R. T. Lv, A. R. Li, Q an Botello-Mendez, T. Hayashi, B. Wang, A. Berkdemir, Q. Z. Hao, A. L. Elias, R. Cruz-Silva, H. R. Gutierrez, Y. A. Kim, H. Muramatsu, J. Zhu, M. Endo, H. Terrones, J. C. Charlier, M. H. Pan, and M. Terrones. *Nitrogen-doped graphene: beyond single substitution and enhanced molecular sensing.* Scientific Reports, **2**, 586 (2012).

[158] A. Lherbier, A. R. Botello-Mendez, and J. C. Charlier. *Electronic and transport properties of unbalanced sublattice N-doping in graphene.* Nano Letters, **13**, 1446 (2013).

[159] T.O. Wehling, S. Yuan, A.I. Lichtenstein, A.K. Geim, and M.I. Katsnelson. *Resonant scattering by realistic impurities in graphene.* Physical Review Letters, **105**, 056802 (2010).

[160] T. Ando, T. Nakanishi, and R. Saito. *Berry's Phase and Absence of Back Scattering in Carbon Nanotubes.* Journal of the Physical Society of Japan, **67**, 2857–2862 (1998).

[161] S. Das Sarma, S. Adam, E.H. Hwang, and E. Rossi. *Electronic transport in two-dimensional graphene.* Reviews of Modern Physics, **83**, 407–470 (2011).

[162] T. Palacios. *Graphene electronics: Thinking outside the silicon box.* Nature Nanotechnology, **6**, 464–465 (2011).

[163] A.F. Morpurgo and F. Guinea. *Intervalley scattering, long-range disorder, and effective time-reversal symmetry breaking in graphene.* Physical Review Letters, **97**, 196804 (2006).

[164] C.P. Ewels, G. Van Lier, J.-C. Charlier, M.I. Heggie, and P.R. Briddon. *Pattern formation on carbon nanotube surfaces.* Physical Review Letters, **96**, 216103 (2006).

[165] C.T. White and T.N. Todorov. *Carbon nanotubes as long ballistic conductors.* Nature, **393**, 240–241 (1998).

[166] S. Roche, G. Dresselhaus, M.S. Dresselhaus, and R. Saito. *Aharonov-bohm spectral features and coherence lengths in carbon nanotubes.* Physical Review B, **62**, 16092–16099 (2000).

[167] J.-C. Charlier, X. Blase, and S. Roche. *Electronic and transport properties of nanotubes.* Reviews of Modern Physics, **79**, 677–732 (2007).

[168] F.V. Tikhonenko, D.W. Horsell, R.V. Gorbachev, and A.K. Savchenko. *Weak localization in graphene flakes.* Physical Review Letters, **100**, 056802 (2008).

[169] F.V. Tikhonenko, A.A. Kozikov, A.K. Savchenko, and R.V. Gorbachev. *Transition between electron localization and antilocalization in graphene.* Physical Review Letters, **103**, 226801 (2009).

[170] E McCann, K Kechedzhi, Vladimir I Fal'ko, H Suzuura, T Ando, and B L Altshuler. *Weak-Localization Magnetoresistance and Valley Symmetry in Graphene.* Physical Review Letters, **97**, 146805 (2006).

[171] N. Leconte, J. Moser, P. Ordejon, H. Tao, A. Lherbier, A. Bachtold, F. Alsina, C.M. Sotomayor Torres, J.-C. Charlier, and S. Roche. *Damaging graphene with ozone treatment: A chemically tunable metal - Insulator transition.* ACS Nano, **4**, 4033–4038 (2010).

[172] A. Lherbier, X. Blase, Y.-M. Niquet, F. Triozon, and S. Roche. *Charge transport in chemically doped 2D graphene.* Physical Review Letters, **101**, 036808 (2008).

[173] K. Nomura and A.H. MacDonald. *Quantum transport of massless dirac fermions.* Physical Review Letters, **98**, 076602 (2007).

[174] Y.-Y. Zhang, J. Hu, B.A. Bernevig, X.R. Wang, X.C. Xie, and W.M. Liu. *Localization and the kosterlitz-thouless transition in disordered graphene.* Physical Review Letters, **102**, 106401 (2009).

[175] F. Ortmann, A. Cresti, G. Montambaux, and S. Roche. *Magnetoresistance in disordered graphene: The role of pseudospin and dimensionality effects unraveled.* European Physics Letters, **94** (2011).

[176] E. Mccann, K. Kechedzhi, V.I. Fala'Ko, H. Suzuura, T. Ando, and B.L. Altshuler. *Weak-localization magnetoresistance and valley symmetry in graphene.* Physical Review Letters, **97**, 146805 (2006).

[177] M. Monteverde, C. Ojeda-Aristizabal, R. Weil, K. Bennaceur, M. Ferrier, S. Guéron, C. Glattli, H. Bouchiat, J.N. Fuchs, and D.L. Maslov. *Transport and Elastic Scattering Times as Probes of the Nature of Impurity Scattering in Single-Layer and Bilayer Graphene.* Physical Review Letters, **104**, 126801 (2010).

[178] X. Hong, K. Zou, and J. Zhu. *Quantum scattering time and its implications on scattering sources in graphene.* Physical Review B, **80**, 241415 (2009).

[179] L. Ciric, A. Sienkiewicz, B. Nafradi, M. Mionic, A. Magrez, and L. Forro. *Towards Electron Spin Resonance of Mechanically Exfoliated Graphene.* Physica Status Solidi B, **246**, 2558 (2009).

[180] R. R. Nair, M. Sepioni, I. L. Tsai, O. Lehtinen, J. Keinon, A. V. Krasheninnikov, T. Thomson, A. K. Geim, and I. V. Grigorieva. *Spin-Half Paramagnetism in Graphene Induced by Point Defects.* Nature Physics, **8**, 199 (2012).

[181] Y. Wang, Yi. Hoang, Y. Song, X. Zhang, Y. Ma, J. Liang, and Y. Chen. *Room-temperature ferromagnetism of graphene.* Nano Letters, **9**, 220–224 (2009).

[182] H. S. S. Ramakrishna Matta, K. S. Subrahmanyam, and C. N. R. Rao. *Novel Magnetic Properties of Graphene: Presence of Both Ferromagnetic and Antiferromagnetic Features and Other Aspects.* Journal of Physical Chemistry, **113**, 9982 (2009).

[183] K. Tada, J. Haruyama, H. X. Yang, M. Chshiev, T. Matsui, and H. Fukuyama. *Graphene Magnet Realized by Hydrogenated Graphene Nanopore Arrays.* Applied Physics Letters, **99**, 183111 (2011).

[184] L. Xie, X. Wang, J. Lu, Z. Ni, Z. Luo, H. Mao, R. Wang, Y. Wang, H. Huang, D. Qi, R. Liu, T. Yu, Z. Shen, T. Wu, H. Peng, B. Ozyilmaz, K. Loh, A.T.S. Wee, Ariando, and W. Chen. *Room temperature ferromagnetism in partially hydrogenated epitaxial graphene.* Applied Physics Letters, **98**, 193113 (2011).

[185] A. J. M. Giesbers, K. Uhlířová, M. Konečný, E. C. Peters, M. Burghard, J. Aarts, and C. F. J. Flipse. *Interface-Induced Room-Temperature Ferromagnetism in Hydrogenated Epitaxial Graphene.* Physical Review Letters, **111**, 166101 (2013).

[186] M. Garnica, D. Stradi, S. Barja, F. Calleja, C. Diaz, M. Alcami, N. Martin, A. L. Vazquez de Parga, F. Martin, and R. Miranda. *Long-Range Magnetic Order in a Purely Organic 2D Layer Adsorbed on Epitaxial Graphene.* Nature Physics, **9**, 368 (2013).

[187] J. Hong, E. Bekyarova, P. Likang, W. A. de Heer, R. C. Haddon, and S. Khizroev. *Room-Temperature Magnetic Ordering in Functionalized Graphene.* Scientific Reports, **2**, 624 (2012).

[188] J. Hong, E. Bekyarova, W. A. de Heer, R. C. Haddon, and S. Khizroev. *Chemically Engineered Graphene-Based 2D Organic Molecular Magnet.* ACS Nano, **7**, 10011 (2013).

[189] K. Sasaki and R. Saito. *Pseudospin and Deformation-Induced Gauge Field in Graphene.* Progress of Theoretical Physics Supplement, **176**, 253 (2008).

[190] K. Sasaki, S. Murakami, and R. Saito. *Gauge Field for Edge State in Graphene.* Journal of the Physical Society Japan, **75**, 074713 (2006).

[191] A. Lherbier, B. Biel, Y.-M. Niquet, and S. Roche. *Transport length scales in disordered graphene-based materials: Strong localization regimes and dimensionality effects.* Physical Review Letters, **100**, 036803 (2008).

[192] J. M. Luttinger. *The effect of a magnetic field on electrons in a periodic potential.* Physical Review B, **54**, 814 (1951).

[193] R. Peierls. *Zur Theorie des Diamagnetismus von Leitungselektronen.* Zeitschrift für Physik, **80**, 763 (1933).